A STUDY ON COAL COMBUSTION: EXPERIMENTS AND MODELLING

A THESIS SUBMITTED TO
THE GRADUATE SCHOOL OF NATURAL AND APPLIED SCIENCES
OF
MIDDLE EAST TECHNICAL UNIVERSITY

BY

BURAK ÖZER

IN PARTIAL FULFILLMENT OF THE REQUIREMENTS
FOR
THE DEGREE OF MASTER OF SCIENCE
IN
MECHANICAL ENGINEERING

DECEMBER 2019

Approval of the thesis:

A STUDY ON COAL COMBUSTION: EXPERIMENTS AND MODELLING

submitted by **BURAK ÖZER** in partial fulfillment of the requirements for the degree of **Master of Science in Mechanical Engineering Department, Middle East Technical University** by,

Prof. Dr. Halil Kalıpçılar
Dean, Graduate School of **Natural and Applied Sciences** _____

Prof. Dr. Mehmet Ali Sahir Arıkan
Head of Department, **Mechanical Engineering** _____

Assist. Prof. Dr. Feyza Kazanç Özerinç
Supervisor, **Mechanical Engineering, METU** _____

Examining Committee Members:

Prof. Dr. Ahmet Yozgatlıgil
Mechanical Engineering Dept., METU _____

Assist. Prof. Dr. Feyza Kazanç Özerinç
Mechanical Engineering, METU _____

Assoc. Prof. Dr. Mehmet Metin Yavuz
Mechanical Engineering Dept., METU _____

Prof. Dr. Görkem Külah
Chemical Engineering Dept., METU _____

Prof. Dr. Murat Köksal
Mechanical Engineering Dept., Hacettepe University _____

Date: 18.12.2019

I hereby declare that all information in this document has been obtained and presented in accordance with academic rules and ethical conduct. I also declare that, as required by these rules and conduct, I have fully cited and referenced all material and results that are not original to this work.

Name, Surname: Burak Özer

Signature:

ABSTRACT

A STUDY ON COAL COMBUSTION: EXPERIMENTS AND MODELLING

Özer, Burak
Master of Science, Mechanical Engineering
Supervisor: Assist. Prof. Dr. Feyza Kazanç Özerinç

December 2019, 126 pages

Coal combustion involves multi-scale, multi-phase and multi-component aspects, in a process where both transport phenomena and reaction kinetics must be considered. The aim of the work is to investigate how the lignite characteristics and origin affect the combustion kinetics at different heating rates. Three Turkish lignites from different regions (Soma lignite, Tunçbilek lignite, Afşin-Elbistan lignite) and one German lignite (Rhenish lignite) were used. Combustion characteristics of these lignites are investigated experimentally and numerically. Experiments are conducted using a high temperature (1000ºC) and high heating rate (~10^4 ºC/s) drop tube furnace (DTF), along with a thermogravimetric analyzer (TGA) at non-isothermal conditions (5, 10, 15, 20 ºC/min). The numerical part of the study includes the computational fluid dynamic analysis of DTF and the predictive multi-step kinetic PoliMi model analysis of the fuel particle. TGA experiments show that the ratio of volatile matter over fixed carbon has an effect on the ignition times. Moreover, maximum reaction rates obtained by TGA experiments are inversely proportional to the ash contents of the fuels used. High heating rate DTF experiments shows similar combustion behaviors with TGA experiments. According to DTF experiments, RL has highest reactivity (RL: 7.8 s-1) among all fuels (AEL: 5.3, SL: 4.7, TL: 2.9 s-1). In comparison to experimental data, PoliMi model predictions on high temperature volatile yields are satisfactory with 5-

7 % errors whereas devolatilization rates are overpredicted. However, PoliMi model predictions on char oxidation rates are in agreement with the experimental data.

Keywords: Coal Combustion, Char reactivity, Drop tube furnace, Thermogravimetry analysis, Kinetic modeling

ÖZ

KÖMÜR YANMASI ÜZERİNE DENEYSEL VE NÜMERİK BİR ÇALIŞMA

Özer, Burak
Yüksek Lisans, Makina Mühendisliği
Tez Danışmanı: Dr. Öğr. Üyesi Feyza Kazanç Özerinç

Aralık 2019, 126 sayfa

Kömür yanması, hem ısı transferi ve akışkanlar mekaniği olaylarının hem de reaksiyon kinetiğinin göz önünde bulundurulması gereken çok ölçekli, çok fazlı ve çok bileşenli bir süreçtir. Çalışmanın amacı, linyit özelliklerinin ve kaynağının yanma kinetiği üzerindeki etkilerinin farklı ısıtma hızlarında incelenmesidir. Farklı bölgelerden üç Türk linyiti (Soma linyiti, Tunçbilek linyiti, Afşin-Elbistan linyiti) ve bir Alman linyiti (Rhenish linyiti) kullanılmıştır. Bu linyitlerin yanma özellikleri deneysel ve sayısal olarak incelenmiştir. Deneyler, izotermal olmayan koşullarda (5, 10, 15, 20 ºC/ dakika) kullanılan termogravimetrik analizör (TGA) ve yüksek sıcaklık (1000 ºC) ve yüksek ısıtma oranına (~ 10^4 ºC / s) sahip düşey borulu fırın (DBF) kullanılarak gerçekleştirilmiştir. Çalışmanın sayısal analiz kısmı, DBF'nin hesaplamalı akışkan dinamik analizini ve yakıt partikülünün kinetik PoliMi model analizini içerir. TGA deneyleri, yakıtların sahip olduğu uçucu maddenin sabit karbona oranının yakıtın tutuşma sürelerine etki ettiğini göstermektedir. Ayrıca, TGA deneyleriyle elde edilen maksimum reaksiyon hızları, kullanılan yakıtların sahip oldukları kül miktarlarıyla ters orantılıdır. Yüksek ısıtma hızı DBF deneyleri, TGA deneyleri ile benzer yanma davranışlarını göstermektedir. DBF deneylerine göre RL tüm yakıtlar arasında en yüksek reaktiviteye (RL: 7.8 saniye^{-1}) sahiptir (AEL: 5.3, SL: 4.7, TL: 2.9 saniye^{-1}). Deneysel verilerle karşılaştırıldığında, PoliMi modeli yüksek

sıcaklıkta elde edilen uçucu madde miktarları üzerine % 5-7 hata ile yakın tahminlerde bulunmuştur, oysa ucucuların salınım hızları olduğundan yüksek hesaplanmıştır. Ancak, PoliMi modelin char oksidasyon hızları üzerine yaptığı tahminleri deneysel verilerle uyumludur.

Anahtar Kelimeler: Yanma, Çar reaktivitesi, Düşey borulu fırın, Termogravimetri analizi, PoliMi model

To My Family

ACKNOWLEDGEMENTS

First of all, I would like to thank my advisor, Asst. Prof. Dr. Feyza Kazanç Özerinç for her continued support, guidance, attention and encouragement throughout my study days. None of this would be possible without her support and encouragement. Besides my supervisor, I would like to thank Duarte Magalhaes for the help with the experimental work of my study. He has been a great mentor and friend to me. Also, I wish to thank my colleagues of Clean Combustion Technologies Laboratory, Süleyman Şener Akın, Kaan Gürel, Mammadbaghir Baghirzade for their support and assistance during all stages of this work. Last three years, I feel privileged to be in this research group and studied with Asst. Prof. Dr. Feyza Kazanç Özerinç. I am very lucky to have such a fun, trustworthy and well-educated team during my graduate years.

I would like to thank Prof. Altan Kayran for the support on TGA experimental trials done in RUZGEM of the Middle East Technical University. Also, I would like to thank Central Laboratory of the Middle East Technical University for the support on the preliminary analysis. I wish to thank the workshop of the Mechanical Engineering Department for the construction of the equipment used in the experiments.

I would like to appreciate TUBITAK (Career Award No: 214M332, and 2210-National Scholarship Programme for MSc Students) for the financial support. These financial supports enabled me to work on my study without worry.

Finally, I wish to express my deepest gratitude to my parents for their love and support throughout my life. I am thankful for everything that they have done for me.

TABLE OF CONTENTS

LIST OF TABLES

TABLES

LIST OF FIGURES

FIGURES

LIST OF ABBREVIATIONS

ABBREVIATIONS

ASTM	American Society for Testing and Materials
BL	Boundary Layer
BET	Brunauer–Emmett–Teller
CBK	Carbon Burnout Kinetics
CELL	Cellulose
CFD	Computational Fluid Dynamics
CPD	Chemical Percolation Devolatilization
FC	Fixed Carbon
FTIR	Fouirer Transform Infrared Spectrometer
FG-DVC	Functional-Group, Depolymerization, Vaporization, and Cross- Linking
DTF	Drop Tube Furnace
DAE	Distributed Activation Energy
DTG	Derivative Thermogravimetry
DO	Discrete Ordinate
GUI	Graphical User Interface
HECELL	Hemicellulose
HHV	Higher Heating Value
HTVL	High Temperature Volatile Yield
LH	Langmuir- Hinshelwood
LHV	Lower Heating Value
LIG	Lignin
MS	Mass Spectrometer
C NMR	Carbon Nuclear Magnetic Resonance
RWE	Rheinisch-Westfälisches Elektrizitätswerk
SEM	Scanning Electron Microscopy

TANN	Tannin
TG	Thermogravimetry
TGA	Thermogravimetric Analysis
TGL	Trilinolein
TPES	Total Primary Energy Supply
VM	Volatile Matter
WMA	Wire Mesh Apparatus

CHAPTER 1

INTRODUCTION

1.1. World Energy Scenario

Worldwide energy demand has grown steadily over the past century and is expected to grow by 50 % from 2018 to 2050 [1]. Historically, pulverized coal firing has provided a significant portion of the total generated electricity in the world (see Figure 1.1). This has been largely due to the abundance and relatively low cost of coal as primary energy source, when compared with other fossil fuels or renewables. Due to these reasons, coal is expected to continue to provide a significant share of the total electricity supply for the next decades, corresponding to 19.4% of the total primary energy [1]. Because of concerns over the high amount of greenhouse gases in the atmosphere there has been, over the past few decades, a remarkable number of studies and efforts for the efficient firing of coal and minimization of emissions.

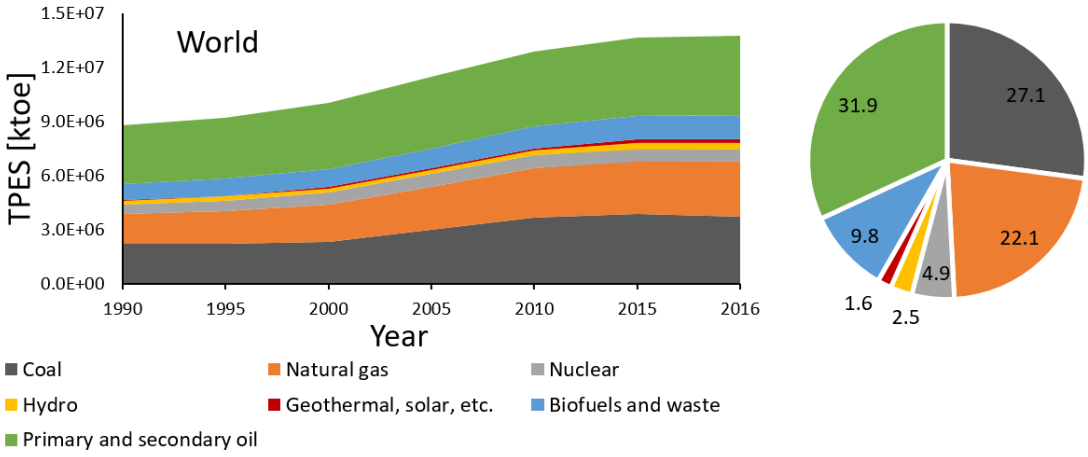

Figure 1.1. Total Primary Energy Supply (TPES) by source –World (Source: IEA World Energy Balances)

Energy security is a pressing issue, especially for the developing countries. In Turkey, 87.1 % of the total primary energy is supplied by fossil fuels (see Figure 1.2), and 83 % of these are imported fuels (source: 2016 Türkiye Ulusal Enerji Denge Tablosu). The utilization of low rank indigenous lignite is required in order to decrease dependency on imported coal, and increase energy security. Lignite is the most abundant coal type in Turkey, with proven reserves of 17.4 billion tones [2]. In 2015, Turkey's Energy and Natural Resources Ministry [3] stated that an increase of 50 % in electricity generation of domestic coal fired power plants was aimed in order to increase the share of the domestic sources.

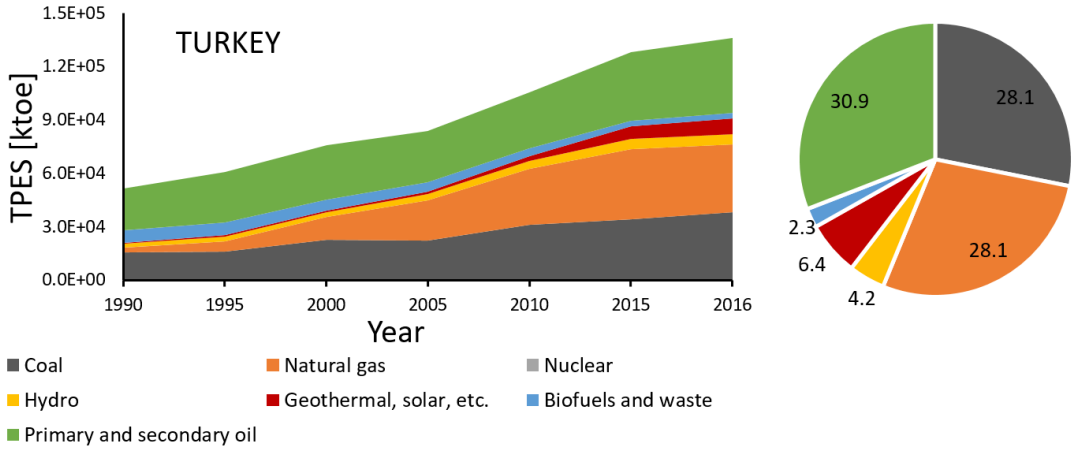

Figure 1.2. Total Primary Energy Supply (TPES) by source –Turkey (Source: IEA World Energy Balances)

1.2. Motivation

Coal combustion is multi-phase, multi-scale and multi-component phenomenon (see Table 1.1). It highly depends on the combustion environment, such as heating rate, temperature and gas phase contents. Since coal combustion serves only energy industry, the focus of the literature on this topic is understanding coal

combustion extensively and increasing the efficiency of pulverized coal combustion boilers. Boiler, closed vessel in which combustion takes place, is fitted with heat exchanger tubes inside of which the working fluid (water) circulates and is heated to generate superheated vapor. In order to have high thermal efficiency in the cycle, the working fluid must heat up as much as possible. The temperature restriction is usually on the turbine's material, and the working fluid temperature is thus limited to 1400-1600 K. These lead to the high heating rate and high-temperature coal combustion in the industrial boilers. When the pulverized coal is injected into the boiler, the coal is exposed to high-temperature which leads rapid combustion. Among many combustion experimental setups, drop tube furnace (DTF) provides some of these conditions, namely the strong radiative heat transfer (also characteristic of the zone of a boiler where combustion mainly takes place), and the high heating rates. Moreover, it permits to conduct experiments in a control and expedite manner.

Table 1.1. Coal combustion problem in different viewpoints

Multi-Phase	Multi-Scale	Multi-Component
Solid phase: Heterogeneous surface reactions, heat transfer by conduction	Particle scale: Intraparticle diffusion of reactant and product gases	Components of coal: Moisture, volatiles, fixed carbon, ash
Gas phase: Secondary gas phase reactions, heat transfer by convection	Boiler scale: Temperature, velocity, pressure profiles	Components of gas phase: Oxygen, nitrogen, carbon dioxide, water vapor

There are many experimental studies on Turkish lignite combustion but none of them provides high heating rate and high temperature to the lignite samples [4–8]. Simulating same combustion conditions in industrial boiler experimentally is expensive and dangerous.

Single particle combustion in drop tube furnace is, though simplified as compared to large scale combustion, still a very complex process. Moreover, this

experimental setup designed for this purpose may not suitable for the sensitivity analysis of coal combustion parameters all the time. CFD analysis supported by experimental validation helps understanding combustion behavior of the coal. It decreases the number of necessary experiments dramatically.

This study aims at investigating the combustion characteristics of the lignites from different origins, experimentally. In order to understand the selected lignites' combustion behavior better, the experimental study under both high and low heating rate conditions is executed. Then, suitable modelling procedure is proposed and validated with the experimental results.

1.3. Objectives

This study investigates the coal combustion in numerical and experimental ways. Main objectives are as follows:

- To experimentally examine the combustion behaviours of lignites mined from three different regions: Western and Southeast Turkey and Western in Germany.
    - To obtain intrinsic kinetic rates of combustion using Thermogravimetric analyzer (TGA)
    - To emulate the combustion conditions in the industrial boilers using drop tube furnace (DTF), and obtain combustion rates in kinetic-diffusion regime
- To model single particle combustion in DTF for the experimentally investigated fuels
    - To model non-reactive flow in DTF combustion experiments and pulverize the fuel particle into the DTF to obtain the temperature and velocity profiles of the fuel particles in DTF.
    - To model the single particle combustion using the multi-step reaction mechanism with a semi-empirical approach

This thesis is structured as follows: in chapter 2 the background information about coal and its conversion methods is given. Experimental and numerical ways used for coal combustion are also provided in the latter sections of chapter 2. In chapter 3 the experimental methods and procedures followed in the scope of this study are explained. The necessary information about the sample fuels used is also provided. In chapter 4 the modelling procedure followed to simulate single coal combustion is explained. Chapter 4 has two main sections: reactive fluid flow modelling and single particle coal combustion modelling. Also, chapter 4 explains the fundamental theory to understand the chemical reaction modelling. The main results of this study are discussed in chapter 5. Chapter 6 finalizes the thesis with major conclusions and suggested future works.

CHAPTER 2

LITERATURE REVIEW

2.1. Coal and its Chemical Structure

Coal is a black rock originated from dead plants. From the effect of pressure over millions of years underground, dead plants were converted to peat, lignite, bituminous coal, anthracite, respectively from youngest to oldest [9].

The chemical structure of the coal mainly depends on its original dead plant(s) and on the conditions during the carbonization process. Figure 2.1 (a) gives an example of the chemical structure of coal. Chemical structure is highly complex, and its heterogeneous nature does not allow to divide it into equal parts. There are various types of functional groups and clusters linked to each other on peripheral positions. Solid state nuclear magnetic resonance (NMR) is one of the experimental methods capable of a direct characterization of the relative number of carbon atoms in the chemical structure of coal [10]. The structural types of carbons can be obtained using the extrapolation techniques [11] on NMR raw data. If the hydrogen and oxygen contents are known, NMR data can furthermore be helpful to comment on the structural features of hydrogen and oxygen in the coal. Figure 2.1 (b) is an example of the chemical structure formed using C NMR analysis.

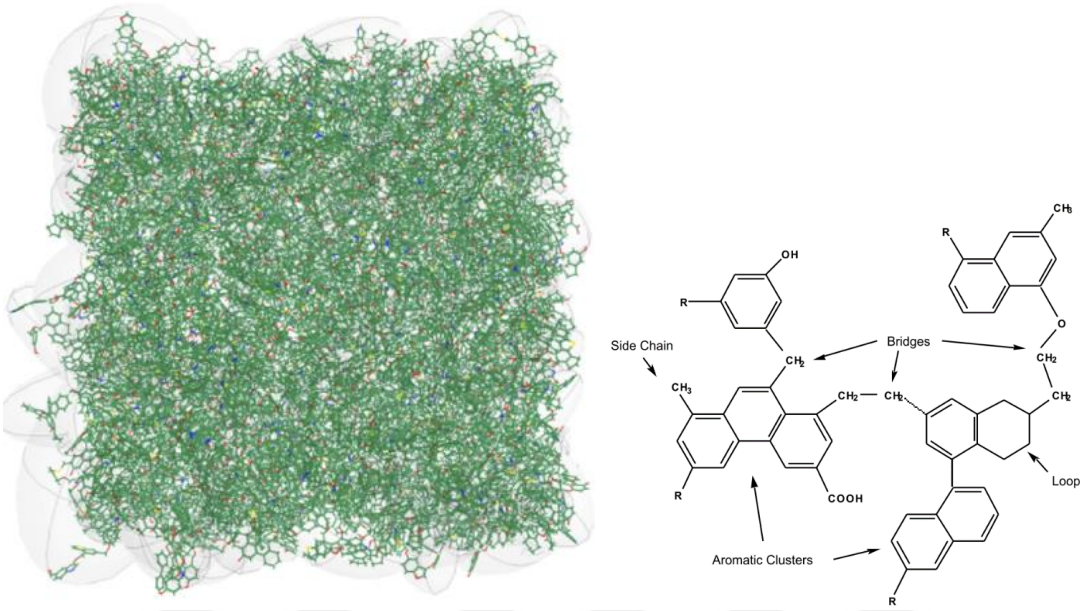

Figure 2.1. Left: Original atomic model of Illinois no. 6 bituminous coal [12]: Carbon (green), Oxygen (red), Hydrogen (blue), Sulphur (yellow). Right: Representative chemical structure identified in C NMR analysis [10]

This multi-component structure of coal has two main parts: inorganic ash and organic maceral. Ash is physically bonded to the maceral. While inorganic ash consists of only minerals (e.g. Si, Ca, Mg, Fe etc.), maceral designates organic substances (C, H, O, S, N) originated from plant tissues [13]. There are three main maceral types: vitrinite, liptinite, and inertinite [14]. Each maceral type has its own elemental composition and crystalline structure. Maceral identification is done using petrographic analysis.

Even though C NMR and petrographic analysis can provide detailed data on the chemical composition and structure of coal, these methods are unusual and expensive. There are, however, other simpler methods to understand the compositional characteristics of the coal. Since coals are used mainly to obtain thermal energy, their characterization is also done by high-temperature conversion experiments.

Accordingly, the basic compositional data for coal is provided using the following tests:

- Proximate analysis (ASTM D5142): It includes the contents of moisture, volatile matter, fixed carbon, ash in parent coal. Moisture is the water present in the coal since the first stage of carbonization process. High moisture content is a sign for young coals. Volatile matter is made of the small clusters and functional groups which can be separated from the main carbon clusters at high temperatures. Volatile matter contains the most of hydrogen and oxygen atoms in the parent coal, in the form of molecules such as CH_4, H_2, CO, C_3H_8. At high temperatures (above 400ºC), volatile compounds are released from the coal in combustible gas form. Ash is the inert solid part of the coal. The remaining part of the coal is named as fixed carbon and is obtained by difference during proximate analysis. During proximate analysis, the coal sample is gradually heated in inert gas environment. After getting constant mass, oxygen agent is fed to the coal sample and heating of the sample proceeds. Figure 2.2 is an example for mass profile of the coal sample during the process. As seen in the figure, each composition is calculated using the constant mass lines: constant mass line at 105 ºC gives the moisture content; the next constant mass line (still under inert atmosphere) gives the volatile content; following injection of oxidizer agent the final constant mass line gives the ash content. Fixed carbon is obtained by difference. The heating rate and temperature points used in the test are experimental parameters and can be changed [15]. Thermogravimetric analyzer (TGA) is the most popular experimental apparatus for proximate analysis.

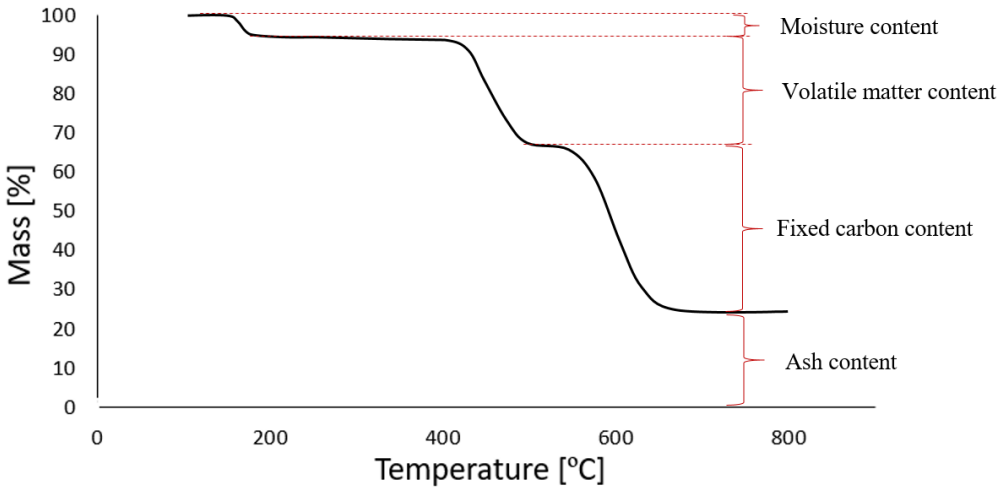

Figure 2.2. Typical proximate analysis results

- Ultimate analysis (ASTM D3176): It is also known as elemental analysis. It gives the elemental composition of the combustible part of the coal sample. Elements included are carbon, hydrogen, nitrogen and, sometimes, sulfur. Also, oxygen is obtained by difference. The analysis excludes the mineral matters in the ash.

- Calorific value determination (ASTM D5865): Calorific value indicates the amount of heat released upon combustion of the fuel. Its unit is kJ/kg. Calorific value is expressed in two ways: net and gross calorific values (or lower and higher heating values). Net or lower heating value corresponds to the case in which water is in vapor form in the combustion products (the case for most combustion processes). For the case of gross or higher heating value, water is condensed and obtained in liquid form in the products. The difference between higher (gross) and lower (net) heating values is the latent heat of vaporization.

- Major and minor element analysis (ASTM D3682): It covers the contents of the inorganics in the ash. These inorganics give an information about the origin of the coal. Some of the inorganics behave as catalysts of the combustion process. Other less desirable outcomes also related with the inorganics in ash are, e.g., ash deposition (ash and fouling) and particulate matter formation.

2.2. Coal Classification

Over centuries, coal classification methods changed with new coal samples and development of new experimental methods. Main types of coals are anthracite, bituminous, sub-bituminous and lignite. Anthracite is the oldest coal with highest calorific value. It has low content of moisture and volatile matter. There are three subgroups of anthracite: semi-anthracite, anthracite and meta-anthracite. Its low amount of volatile matter makes its ignition difficult. For this reason, anthracite coals are not suitable for power generation applications. Bituminous and sub-bituminous coals are the most common coals used in power plants. Bituminous coal has calorific values similar to anthracite and enough volatile matter for its fast ignition and combustion. Lignite coals are the youngest coals and include some remaining woody

structures from its plant origins. Its low calorific value and high moisture content makes it the least desired among the other coals.

There are many coal classification systems in the history. One of the oldest one is Fraser's classification system established in 1877. This system orders coal types based on the ratio of fixed carbon to volatile matter (Table 2.1). In Great Britain, Seyler published a classification system (Appendix C) seen as a masterpiece of scientific coal classification in 1900. His system is based on elementary composition of the coals. The coals with carbon content equal or below 75% are not included, meaning that lignite has no place in this classification.

Table 2.1. Fraser's coal classification [16]

Type	Fuel ratio
Anthracite	100-12
Semi-Anthracite	12-8
Semi-Bitumious	8-5
Bitumious	5-0

In recent years, Van Krevelen diagram and ASTM standards are the most popular coal classification systems. Van Krevelen diagram (Figure 2.3) shows the atomic C, O, H ratios of each organic based solid fuels. It also provides a clear image for the aging process of coal. Carbonization process of the biomass over centuries follows the path from biomass (RHS of the diagram) to anthracite (LHS of the diagram). ASTM coal classification uses both the calorific value and the proximate analysis of the coal, and is available in Table 2.2.

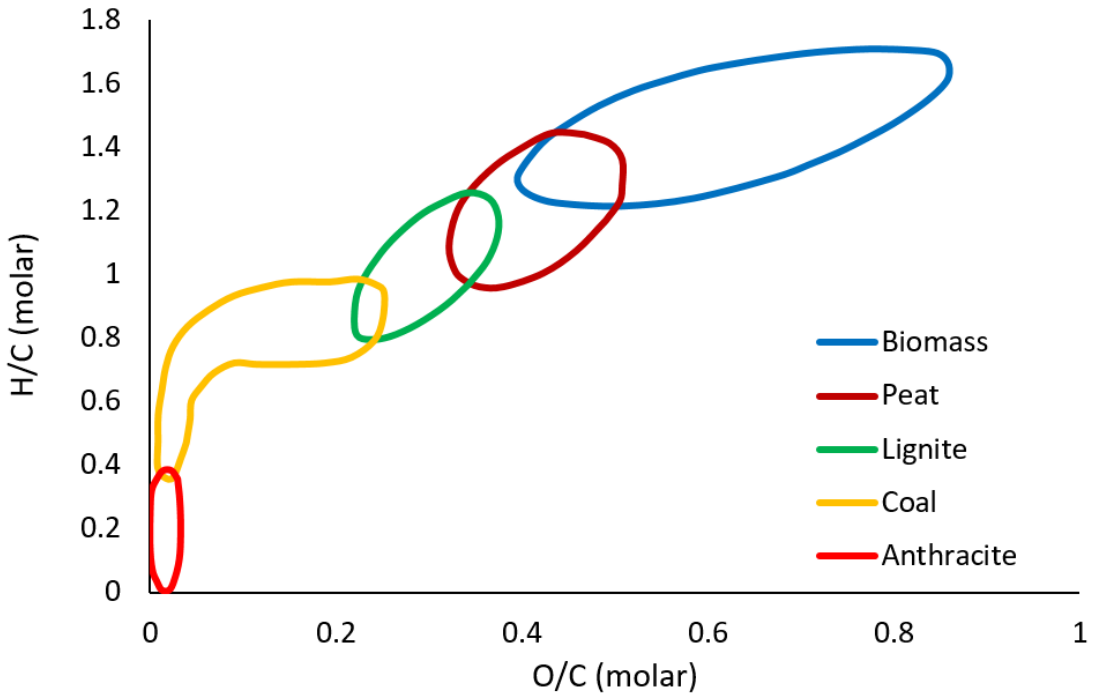

Figure 2.3. Van Krevelen diagram for various solid fuels

Table 2.2. Coal classification in ASTM standards [17]

Class	Group	Fixed Carbon		Volatile Matter		Energy	
		Dry%	Moist%	Dry%	Moist%	Dry(BTUs/lb)	Moist(MJ/kg)
Anthracite	Met anthracite	>98	>92	<2	<2	13,500	31,4
	Anthracite	92-98	89-95	2-8	2-8	15,300	35.5
	Semi anthracite	86-92	81-89	8-14	8-15	14,900	34.6
Bituminous	Low-volatile	78-86	73-81	14-22	13-21	15,400	35.8
	Medium-volatile	69-78	65-73	22-31	21-29	14,900	34.6
	High-volatile A	<69	58-65	>31	>30	>14,000	>32.5
	High-volatile B	57	53	57	40	13,000-14,000	30.2-32.5
	High-volatile C	54	45	54	40	10,500-13,000	24.4-30.2
Sub-bituminous	A	55	45	55	38	10,500-11,500	24.4-26.7
	B	56	43	56	35	9,500-10,500	22.1-24.4
	C	53	37	53	36	8,300-9,500	19.3-22.1
Lignite	A	52	32	35	38	6,300-8,300	14.7-19.3
(brown coal)	B	52	26	32	50	<6,300	<14.7

2.3. Coal Conversion

Coal conversion is categorized into two subsections: combustion and pyrolysis depending on the content of the gas phase to which coal is exposed.

2.3.1. Combustion

Combustion is a self-sustained exothermic chemical reaction of a fuel with an oxidizer. The oxidizer is oxygen for the combustion of hydrocarbon fuels. Like all other reactions, it has activation energy barrier. Provided that the fuel-oxidizer mixture is within the flammability limits, sufficient external heat that surpasses the activation energy barrier will trigger the reaction. Thus, the types of the products of combustion depends on the fuel and on the active sites (i.e. the available carbon sites that oxygen can react with). The following reactions are examples of combustion reactions for different fuels.

$$Hydrocarbon: 4\,C_XH_Y(g) + (4X + Y)\,O_2(g) \rightarrow (2Y)\,H_2O(g) + (4X)\,CO_2(g) \quad (1)$$

$$Hydrogen \quad : \quad H_2(g) + \quad 0.5\,O_2(g) \rightarrow \quad H_2O(g) \quad (2)$$

$$Carbon \quad : \quad C(s) + \quad O_2(g) \rightarrow \quad CO_2(g) \quad (3)$$

With insufficient time or oxygen, combustion reactions are incomplete. For carbon or hydrocarbons, incomplete combustion causes the output of CO along with CO_2 and H_2O.

Combustion reactions can be categorized as homogeneous or heterogeneous depending on the current physical state of the fuel and oxidizer. Homogeneous reactions occur in a single phase. The most common example is the combustion of mixture of natural gas and air. Heterogeneous reactions take place at an interface of reactants which are in two or more phases (e.g. carbon oxidation, surface reactions on catalysis).

Coal combustion process is a complex process in which diffusional mass transfer and surface reaction kinetics are coupled. Combustion of solid fuels can be categorized in four stages: drying, devolatilization, volatile combustion (homogeneous), and char combustion (heterogeneous). The process is summarized visually in Figure 2.4. However, there is no exact separation between the steps in the Figure 2.4. Specifically, devolatilization and char combustion tend to occur at the same time for some coals [18–20]. After the completion of the four stages, the left residual of is ash (inorganic).

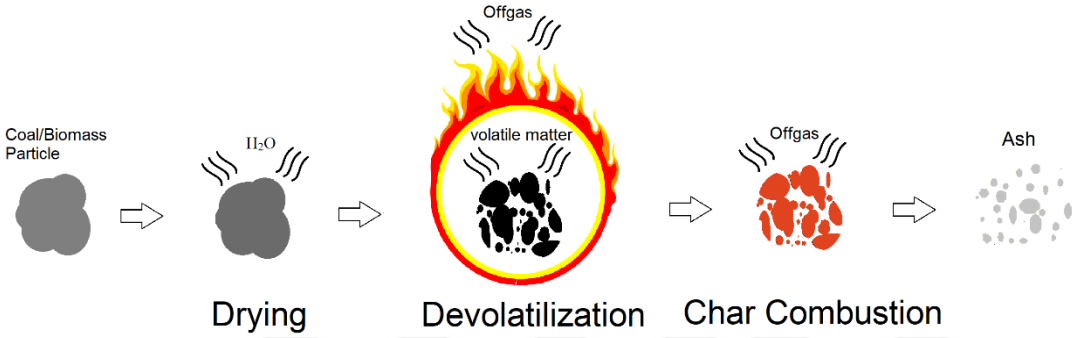

Figure 2.4. Steps of solid fuel combustion: drying, devolatilization, char oxidation

The solid particle first undergoes the drying stage during which the desorption of gases stored in pores of the coal structure during its formation, takes place at temperatures about 100 ºC. Water steam, methane, nitrogen, carbon dioxide are some of them [9]. Above 400 ºC, devolatilization takes place. The temperature at which devolatilization starts depends on the solid fuel composition. Devolatilization has three distinct physical and chemical processes: pyrolysis (decomposition of solid fuel), volatile matter transport through the pores, and secondary reactions that may occur provided sufficient residence time of the volatiles and cause the decomposition of volatile matter to other gas products [21]. The pyrolysis behavior of coal depends on the combustion conditions and on the physical and chemical properties of coal [22–24]. The generated volatiles oftentimes cause swelling due to high internal pressure, which may result in fragmentation due to high porosity. Moreover, the amount of

volatiles released depends on the environmental conditions. It is confirmed that high heating rate causes more volatile release [25]. The volatile matter is released and oxidized simultaneously (volatile combustion) if there are oxygen molecules in the environment, and the mixture is within flammability limits. After the devolatilization stage, only char is left in the solid particle.

Depending on the heating rate and temperature, char combustion may be controlled by chemical kinetics or diffusion rate. Figure 2.5 shows the three zones for char combustion. Char combustion is controlled by chemical kinetics at low temperatures, oxygen pore diffusion at moderated temperatures and oxygen bulk diffusion at high temperatures. Comparison of diffusion and chemical kinetics' time scales is another way to divide these into regions.

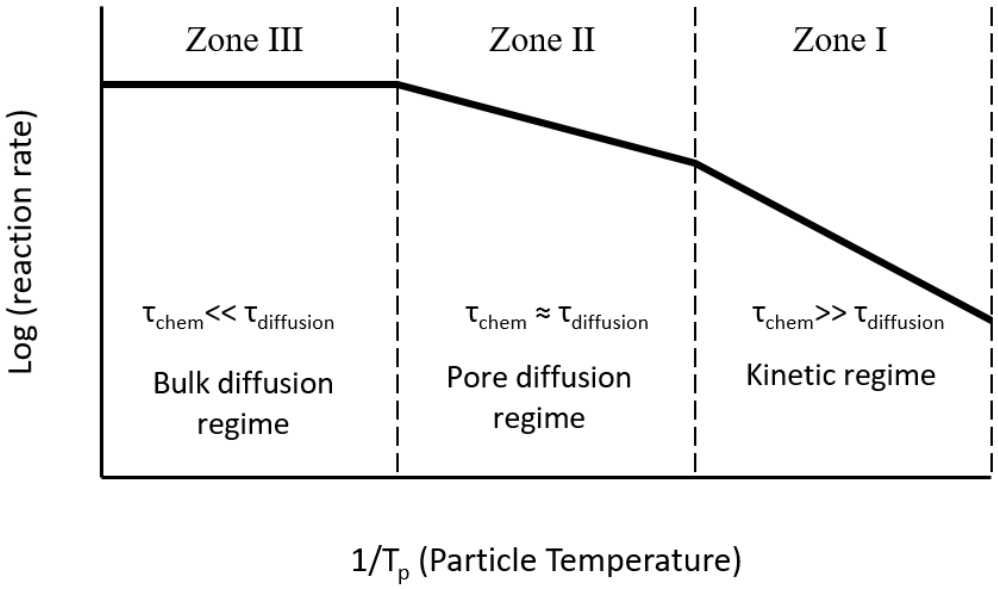

Figure 2.5. Rate-controlling regimes for heterogeneous char oxidation [26]: τchem: Time scale of chemical kinetic, τdiffusion: Time scale of diffusion rate

Another way of analyzing the different combustion regimes is by attending at Figure 2.6 that shows the oxygen concentrations in the boundary layer and the particle.

Zone I is referred to the kinetic limited case. Oxygen molecules diffuse into the particle center and encounter carbon molecules at a higher rate than the combustion reaction rate. Since oxygen molecules are not consumed fast enough, oxygen concentration is constant in the boundary layer and the particle. On the contrary, zone III has higher reaction kinetic rate than diffusion rate. Combustion reactions are so fast that high flow rate of offgas does not allow oxygen molecules to reach the particle. In the case of zone II, kinetic and diffusion rates are so close to each other that the reactant gas is consumed in the particle but does not reach its center.

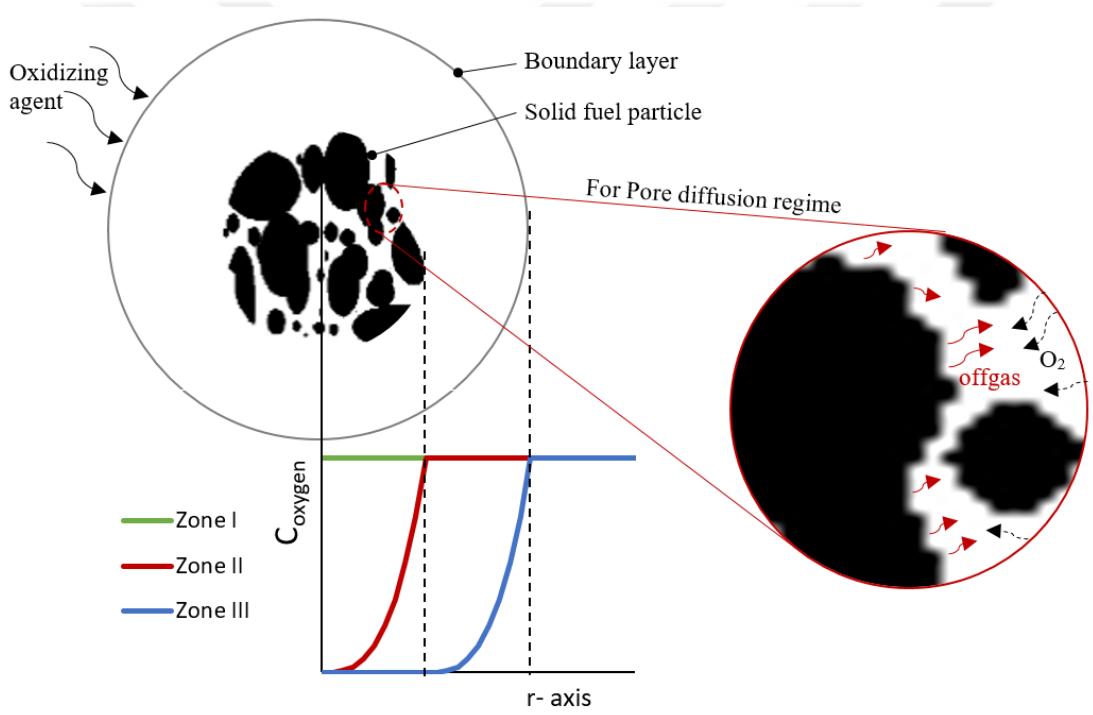

Figure 2.6. Oxygen concentration profile inside the boundary layer shown on the sketch

The following reaction steps are used to represent whole coal combustion process [21]:

$$Decomposition \quad : \quad Coal\,(raw) \rightarrow Char + Volatile + H_2O \qquad (4)$$

$$Homo.\ combustion : Volatiles + O_2 \rightarrow CO + H_2O + SO_2 + NO \quad (5)$$

$$Hetero.\ combustion : Char + \frac{1}{\Phi}O_2 \rightarrow (2-\frac{2}{\Phi})CO + (\frac{2}{\Phi}-1)CO_2 \quad (6)$$

$$Gasification.1 : Char + CO_2 \rightarrow CO + CO \quad (7)$$

$$Gasification.2 : Char + H_2O \rightarrow H_2 + CO \quad (8)$$

Adsorption and desorption reactions are also quite important for heterogeneous reactions. Adsorption is the adhesion of fluid molecules to another fluid or solid phase. Desorption is the reverse of adsorption. Heterogeneous reactions do not occur without adsorption and desorption. The following reaction steps represent the adsorption and desorption that occurs at the solid surface [27]:

$$Adsorption.1 : 2\,C_f + O_2 \rightarrow 2\,C(O) \quad (9)$$

$$Adsorption.2 : C_f + CO_2 \leftrightarrow C(O) + CO \quad (10)$$

$$Desorption.1 : C(O) \rightarrow CO + (free\ site) \quad (11)$$

$$Desorption.2 : 2\,C(O) \rightarrow CO_2 + C_f \quad (12)$$

Where C_f and C(O) are free site and chemisorbed oxygen atoms on carbon surface, respectively.

To sum up, oxygen molecules first diffuse through the boundary and get into the particle's pores. Oxygen starts to fill the free sites after it reaches the carbon surface. Next, combustion reaction can begin (and end). Product gasses of combustion (offgas) leaves by means of desorption, and diffusion through pores and boundary layer (BL), in order. Figure 2.7 gives the char combustion steps by means of diffusion and reactions stages.

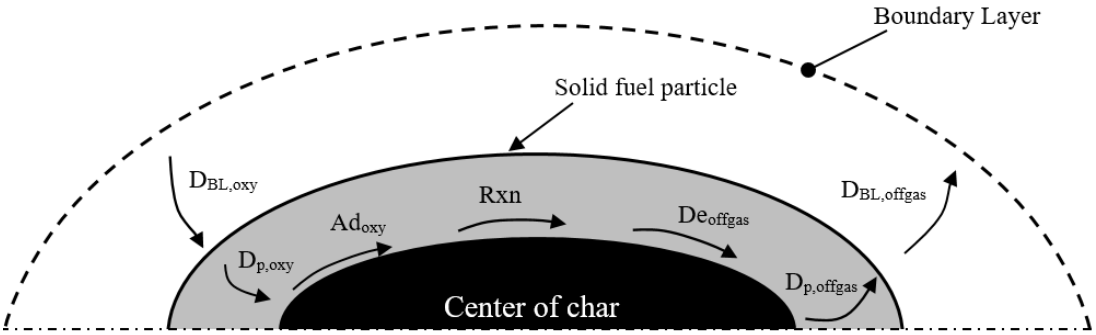

Figure 2.7. Char combustion with diffusion and reaction stages: DBL,oxy (oxygen diffusion through BL), Dp,oxy (oxygen diffusion through pores), Adoxy (oxygen adsorption), Rxn (heterogeneous reaction), Deoxy (oxygen desorption), Dp,offgas (offgas diffusion through pores), DBL,oxy (offgas diffusion through BL)

2.3.2. Pyrolysis

Pyrolysis is the thermal decomposition of a solid fuel in an absence of an oxidizing agent. Pyrolysis starts with converting raw coal to metaplast which is an intermediate plastic phase. Products of pyrolysis are char (solid) and volatile matter (liquid and gas). There are two types of volatiles: condensable (tar) and non-condensable (light gases). Tar consists of larger chemical structures than light gases (see Figure 2.1). Since larger clusters have more chemical bonds with the main coal structure, their bonding energy is high. Therefore, light gases are released before tars during pyrolysis. If tars are exposed to sufficiently high temperatures, and provided sufficient residence time, tar cracking (decomposition of tar to light gases and soot) happens. Figure 2.8 shows the main steps of pyrolysis.

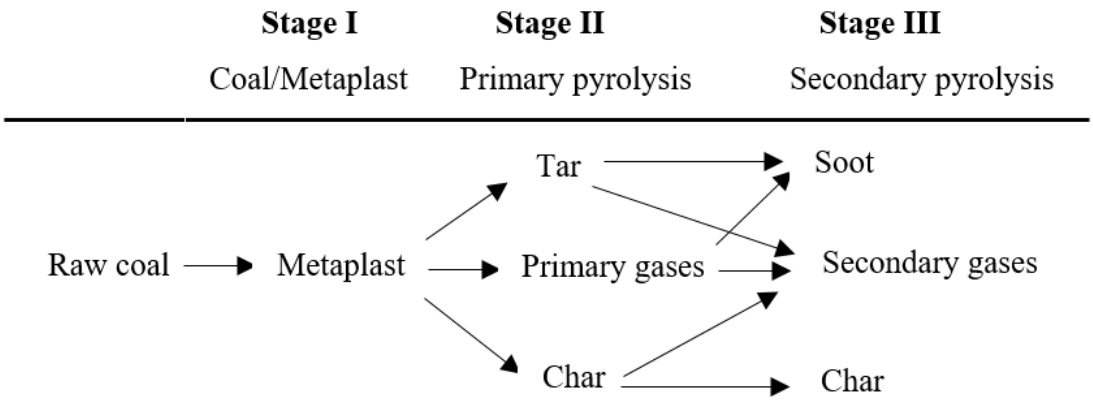

Figure 2.8. Steps of solid fuel pyrolysis [28]

The main types of pyrolysis are torrefaction (also termed mild pyrolysis), slow pyrolysis, fast pyrolysis and flash pyrolysis. Torrefaction is a partially done pyrolysis which performed at low temperatures for long residence times, and typically for biomass fuels. This process improves the fuel's properties, such as heating value and grindability. Slow pyrolysis (long residence times) is used for the production of charcoal without any tar release. The purpose of fast pyrolysis (>10-200 ºC/s) is to produce bio-oil. High heating rate cause higher volatile yield. Flash pyrolysis (10^3 – 10^4 ºC/s) can achieve even higher bio-oil yields as compared with fast pyrolysis.

2.4. Experimental Studies

There are different types of experimental setups to investigate solid fuel combustion. Combustion environment provided to the solid fuel depends on the experiment design and procedure. The ultimate goal is to simulate combustion conditions in large scale combustion systems such as boilers in power plants. Therefore, experimental rigs with capabilities to work at high heating rate and high temperature are preferred by researchers [19,20,29–31]. Three different experimental

setups are presented in this section: drop tube furnace, wire mesh apparatus, and thermogravimetric analyzer.

2.4.1. Drop Tube Furnace (DTF)

DTF is a laboratory-scale furnace which can provide high heating rate (10^4-10^5 ºC/s) and high-temperature (up to 1500 ºC) reaction conditions for solid fuel combustion. It is used to investigate solid fuel ignition characteristics [19,32,33], combustion kinetics [19,34–40], pyrolysis[41–43] and gaseous emissions [29,30,37,44–46]. In the recent studies, the effects of the fuel type/rank [18,19,47,48] and ambient composition [29,34,40] on the combustion phenomena are widely discussed. DTF is designed to provide similar combustion conditions with industrial boilers. The main heat transfer mechanisms are radiation and convection, at the image of industrial boilers. DTF experimental setup consists of a feeding system for solid fuel and gas phase, a vertically placed tube covered with heating elements, and a collection system. As an example, Figure 2.9 shows a DTF setup used for solid fuel conversion experiments. Thermocouples are positioned on the DTF wall to monitor the temperature and ensure constant temperature along the reaction zone. During the experiment, solid fuel is fed into the reactor with the help of transport air, whereas the secondary air is set to provide sufficient oxygen for the combustion. Water cooled injector is used to keep particle temperature below ignition temperature until reaching the reaction zone. Post-combustion solid fuel residues are collected using filter(s) at the end of DTF.

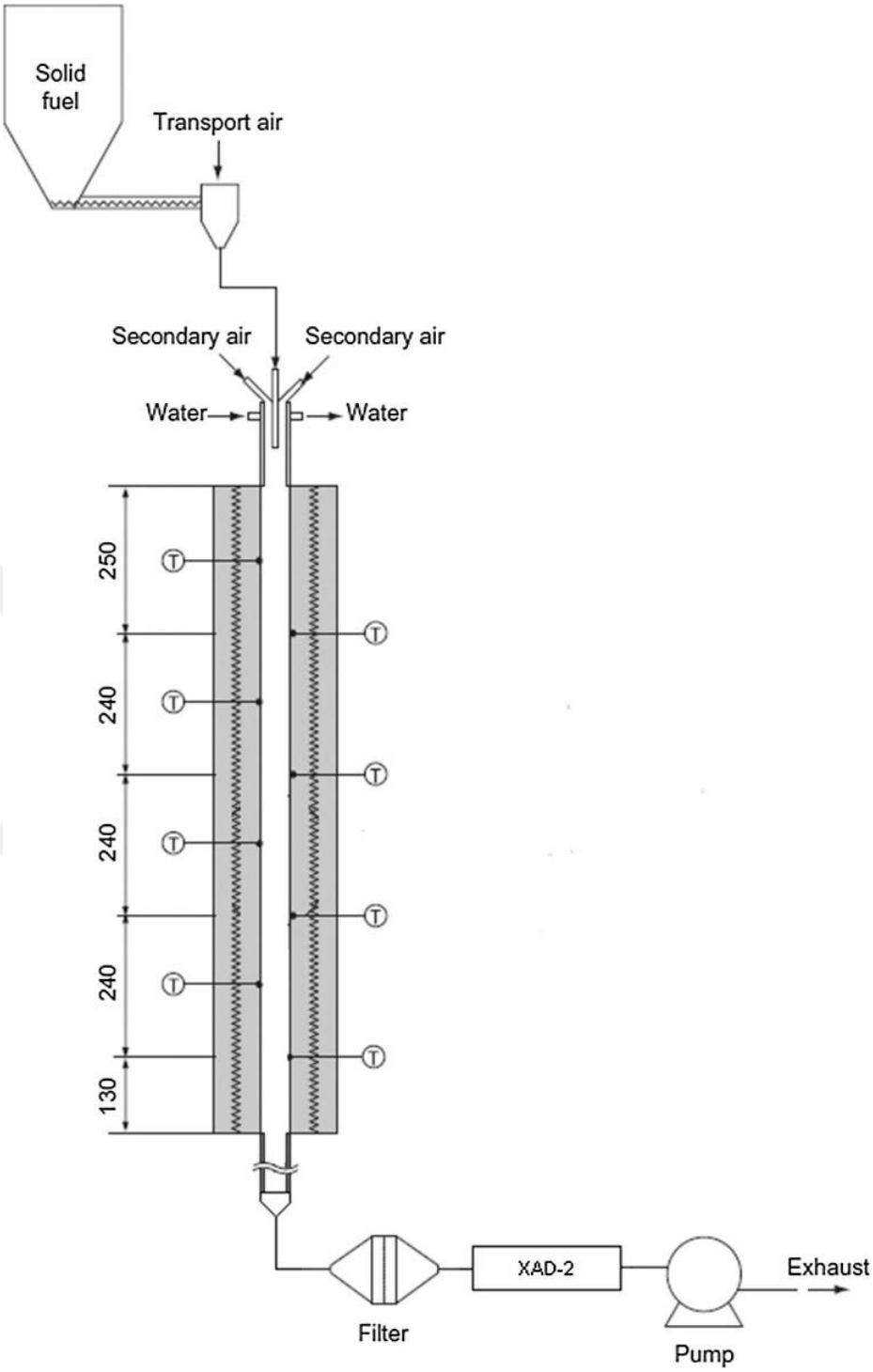

Figure 2.9. Schematic view of drop tube furnace [49]

Under the light of experimental data obtained using DTF, effects of the parameters in experimental conditions are investigated. It is concluded that the smaller particle size [29] and higher wall temperature [50–52] lead faster combustion process, particularly at the early combustion stages.

Dhaneswar and Pisupati [53] investigated the effects of coal rank on air combustion in DTF using 4 different coals. Combustion tests done at 1600ºC show that low rank coals had higher reactivities than the high rank coals. Similarly, Li et al. [51] obtained combustion rates of two different coals (anthracite and bituminous) with DTF operated at 1000 ºC. It was observed that anthracite coal has much lower conversion rate than bituminous coal. At residence time of 1.15 s, fuel conversions were 32% and 87% for anthracite and bituminous, respectively.

Riaza et al. [47] investigated the combustion and ignition behavior of single particle of four coals with different ranks using electrically heated laminar flow drop tube furnace. Results showed that combustion behavior varies depends on the coal ranks. Char and volatile burnout times are increasing linearly with carbon and volatile contents in the coal, respectively. Additionally, Khatami and Levendis [54] reported cinematography images of various coal types obtained with DTF experiments at wall temperature of 1400 K and quiescent flow conditions. According to the cinematography [54], burnout times and the tendency of the coal to have distinguishable combustion phases grows as coal rank increases.

In a recent work, Magalhaes et al.[19] reported the fragmentation and combustion behaviours of Tunçbilek and Soma lignites under high heating rate and high temperature conditions. Cinematography, coupled to drop tube furnace, showed that Soma lignite particles fragmented extensively in devolatilization stage. Then, simultaneous devolatilization and char oxidation occurred for resultant fragments. Sudden increase in surface area of Soma lignite due to the fragmentation resulted in shorter burnout time. On the other hand, Tunçbilek lignite, which have similar

elemental composition with Soma lignite, exhibited devolatilization and char oxidation in order.

2.4.2. Wire Mesh Reactor (WMR)

WMR is a lab scale experimental setup used for solid fuel conversion experiments that consists of a wire mesh, electrodes and thermocouple. The wire mesh is heated with a DC power supplier and the temperature controlled with a PC controller. Electrical current supplied by DC power supplier is transferred to the wire mesh by means of electrodes. The PC controller sets necessary current according to instant temperature measured by the thermocouple. Gas inlet/outlet valve(s) and vacuum pump are used to control the pressure and gas phase content in the reactor. WMR is capable of providing high heating rates (1-10^3 ºC/s), high temperatures (up to 1600 ºC), and a wire array of gaseous compositions.

Obtaining high heating rate and controllable gas compositions in WMR allows the studies on single particle conversion [55–63]. WMR is also widely preferred for pyrolysis studies of different biomass feedstocks [55–59], and coal [60–63]. WMR prevents secondary pyrolysis (see Figure 2.8) and provides accurate yield of pyrolysis product due to the short residence time of the volatile gases under high temperature.

2.4.3. Thermogravimetric Analysis (TGA)

TGA is a device which monitors the mass of a sample as a function of temperature or time. Temperature, pressure and gas composition are controllable parameters. There are two types of TGA: top-loading and bottom-loading (hang down) [64]. The design affects balance precision and capacity. A TGA has small furnace volume covered by heating elements to control the temperature in it. There is a sample pan supported by a precision balance in the furnace volume. Gas content of sample

environment is controlled via inlet purge gas. The mass of the sample placed in the pan is monitored during the operation.

In constants to WMR and DTF, TGA is used in different research area which makes it the easy to access. Its availability and repeatability makes it one of the most used apparatus in the literature [4,5,71–80,6,81–83,37,65–70] TGA is used to research solid fuel ignition behavior [65–68], conversion kinetics, namely pyrolysis [69–76], gasification [69,75,77–79], combustion [4–6,37,69,80–83], and the gaseous products released during these processes [6,70,74]. The studies on the combustion kinetics investigated the thermal reactivity of the chars prepared in N_2 and CO_2 environments [80,81,83,84], biomass/coal blends [82], and the parent fuels [4,5,37] under different atmospheres (e.g. air or oxy-fuel environments). Combustion characteristics of parent fuels were evaluated to assess the influence of the fuel type and heating rate on the combustion behavior. Non-isothermal TGA experiments helped to understand the effect of the fuel compositional properties on its combustion behavior. Barzegar et al. [4] used non-isothermal TGA experiments to compare the combustion and oxy-fuel combustion characteristics of two Turkish lignites, namely Orhaneli lignite and Soma lignite. Three different oxygen concentration ratios were selected. Results showed that the oxy-fuel combustion had higher activation energy than the combustion under air. As oxygen concentration increased, combustion process had higher activation energy and took less time. Also, Orhaneli lignite with the lower ash content (10.51%) compared to that of Soma lignite (42.64%) showed more rapid weight loss during combustion.

Botelho et al. [37] studied the effect of torrefaction on combustion behaviors of grape pomace. Non-isothermal TGA experiments with a heating rate of 10 ºC/min gave the activation energy at devolatilization stage as 84.9 and 85.2 kJ/mol, and at char oxidation stage as 137.5 kJ/mol and 109.2 kJ/mol for raw and torrefied fuel, respectively. Magalhaes et al. [5] investigated the combustion behaviors of olive residue(OR) and two Turkish lignites; Soma lignite(SL) and Tunçbilek lignite(TL). Combustibility index, characteristic temperatures and conversion stages were

identified, and obtained using non-isothermal TGA experiments. An increase in heating rate caused higher reactivity, combustibility and burnout temperatures for all fuel samples. The similarities among the activation energies for the combustion stages of the sample fuels were attributed to the volatile matter/fixed carbon ratios (OR: ~4, SL: ~1.2 TL: ~0.8).

Riaza et al. [85] investigated the oxy-fuel combustion reactivity of coal and coal/biomass blends chars. In this study, different feedstocks were pyrolyzed in the entrained flow reactor under 1000ºC and N_2/CO_2 atmosphere. Obtained chars were burned in non-isothermal TGA experiments to see which numerical model represents char reactivity better. Al-Qayim et al. [73] performed two step TGA experiments to observe how the parent fuel composition effect the char reactivity. First step was the non-isothermal pyrolysis at same heating rate for all experiments. Then, Second step was the isothermal char oxidation at different temperatures. Changes in gas phase content can be done immediately due to TGA's small reactor volume. Fourier transform infrared spectrometer (FTIR) and mass spectrometer (MS) are the experimental rigs commonly used along with TGA [69,70]. These methods monitor the release of gaseous species during the experiment.

TGA provides two graphs; TG (mass loss, %) and DTG (derivative mass loss, %/min) vs temperature or time. Method of characteristic temperatures is a graphical method based on TG and DTG curves that describes the combustion characteristics of solid fuel in a quantitative manner with no kinetic modelling required [5,6,65,72,82,86–88]. Characteristic temperatures are: decomposition temperature (T_D), ignition temperature (T_{ig}), peak temperature (T_P) and burnout temperature (T_B). In Figure 2.10, the characteristic temperatures are displayed graphically. Characteristic temperatures are determined using ash free basis TG and DTG graphs. Decomposition and burnout temperatures indicate the onset and end of the conversion, respectively. They are meant to be the temperatures at mass loss rate of 1%/min. Peak temperature is the temperature with highest mass loss rate in overall process. Ignition temperature is located at the intersection of two tangent lines on TG line; tangent to

the point at highest mass loss rate and tangent to the point where all moisture is released. TG graph can be divided into stages using characteristic temperatures. Decomposition stage (S_D) is defined from decomposition(T_D) and ignition temperatures (T_{ig}). Second stage named as combustion stage (S_C) starts by ignition temperature (T_{ig}), and continue to the burnout temperature(T_B).

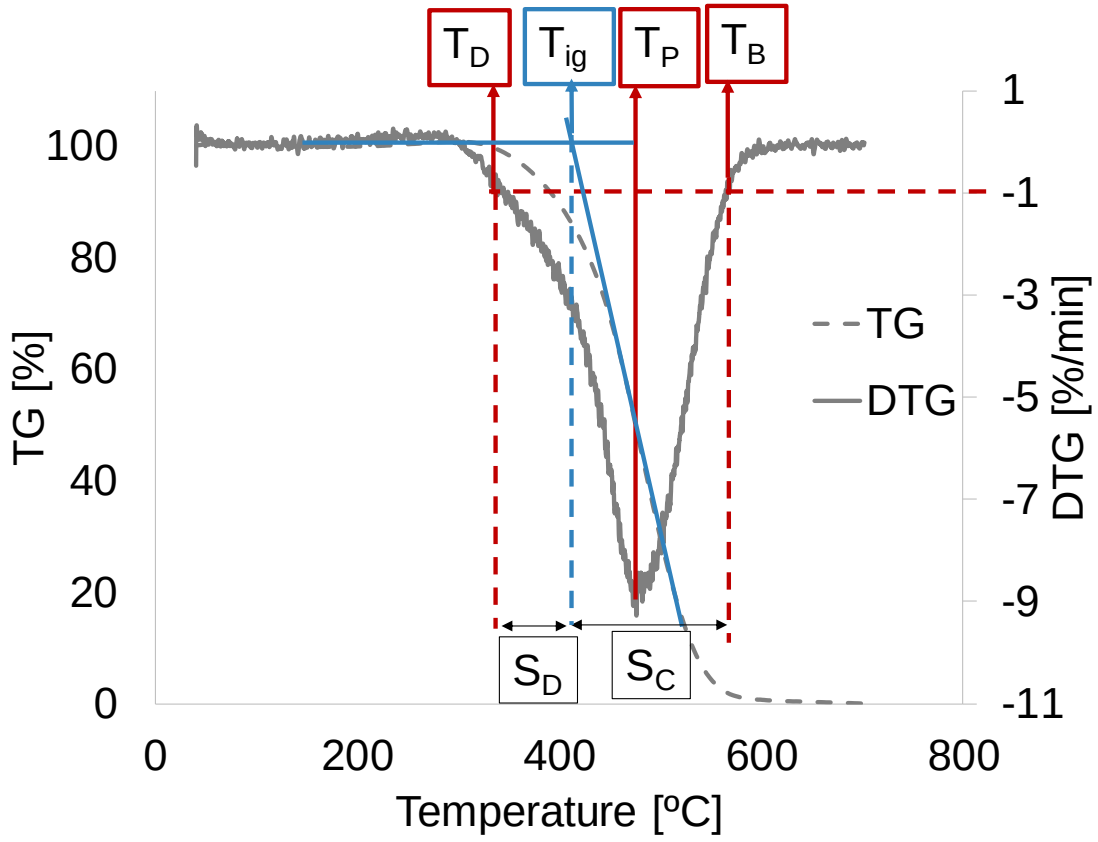

Figure 2.10. Graphical illustration of characteristic temperatures obtained using TG and DTG curves

2.5. Numerical Studies

The progress in the scientific knowledge enables boiler designs with higher efficiency and lower greenhouse gas emissions. Nowadays, research needs comprise, but are not limited to, the understanding surface reactions (heterogeneous chemistry)

and transport phenomena. The improvements in the available computational power enables researchers to use computational fluid mechanics (CFD) more effectively in their studies. CFD is a fast and inexpensive tool to analyze various complex cases, such as turbulence, multi-phase flows, and solid fuel combustion.

In the literature, coal combustion is modelled in three stages: drying, devolatilization and char oxidation [89–94]. For each stage, there are different numerical models. In order to model coal combustion in its entirety in a single simulation, devolatilization and char models need to be used consecutively. In this manner, the two main combustion stages (devolatilization and char oxidation) are not allowed to occur at the same time, which is a limitation of these models. In the following subsections, information is given about the most popular devolatilization and char models developed until now.

2.5.1. Devolatilization Models

In this section, devolatilization models are summarized following the classification suggested by Sankar et al. [95] (see Figure 2.11).

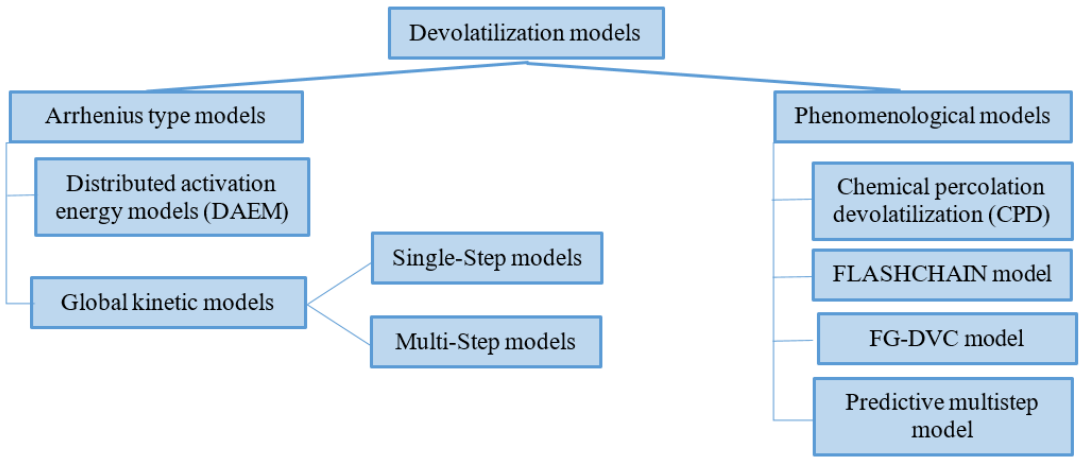

Figure 2.11. Classification of devolatilization models [95]

Phenomenological and Arrhenius type models are two separated groups due to their distinct usage procedures. Arrhenius type models need experimental results to be fitted. The activation energy and pre-exponential factors obtained using Arrhenius models are restricted to the conversion (i.e. pyrolysis) conditions and the respective fuel, so it is difficult to be generalized. Phenomelogical models aim to predict the experimental result using compositional data of coal before performing the respective experiment. In contrast with Arrhenius models, Phenomelogical models try to simulate phenomenological processes occur during devolatilization, such as depolymerization and cross linking. Phenomelogical models have mathematical frameworks based on the coal network structure developed using the compositional data of the coal. For this reason, they are also called as network models.

2.5.1.1. Arrhenius Type Models

Arrhenius type models use the global reaction rate definition with reaction rate constant in Arrhenius form. Global reaction rate for isothermal conditions is in the following form:

$$\frac{dV}{dt} = k\,(V_\infty - V)^n \tag{14}$$

$$k = A\,e^{-\frac{E}{RT}} \tag{15}$$

where V is the normalized mass of volatiles on a dry ash-free basis, V_∞ is the value of V at particular time, n is reaction order, t is time, k is rate constant defined in Arrhenius form (equation 15). A and E are the pre-exponential factor (min^{-1}) and activation energy (J mol^{-1}), respectively. These two also are called as Arrhenius kinetic coefficients. R is the universal gas constant (J K^{-1} mol^{-1}) and T is absolute temperature (K).

Under non-isothermal conditions with constant heating rate [96], temperature defined as,

$$T = T_0 + \beta t \tag{16}$$

Where β is heating rate (K/min), T_0 and T are the initial temperature and the temperature at particular time. The conversion of isothermal reaction rate (dV/dt) into nonisothermal reaction rate (dV/dT) can be done according the following expression:

$$\frac{dV}{dT} = \frac{dV}{dt}\,\frac{dt}{dT} \tag{17}$$

where dT/dt is the heating rate (β). Substituting (14) and (15) into (16) gives,

$$\frac{dV}{dT} = \frac{A}{\beta}\, e^{-\frac{E}{RT}}\,(V_\infty - V)^n \tag{18}$$

Another method to take into account a linear change of temperature with time is to apply fourth-order Runge Kutta Method to the combination of equations (14-16) described as [97],

$$\frac{dV}{dt} = A\, e^{-\frac{E}{R(T_0+\beta t)}}\,(V_\infty - V)^n \tag{19}$$

Single-step model is the simplest way to simulate the devolatilization. Volatile matter is released in one step reaction and gives the final products, as in the mechanism proposed by Gürüz et al. [97],

$$Coal \rightarrow Gas + Tar + Char \tag{20}$$

Single-step method is one of the oldest model used in many solid fuel conversion studies [98–100]. However, it is seen that devolatilization rate and products changes along different temperature ranges. Kobayashi et al. [101] presents results on coal devolatilization at high temperature with high heating rate. At high temperatures the volatile yields are significantly greater than those determined with the ASTM standards. In order to add the effect of temperature on volatile yields, a model that consists of two competing reactions is implemented. The two step model,

also named as Kobayashi model (Figure 2.12), is the most popular multistep model in the literature. Two parallel reactions with distinct activation energies can predict the amount of volatile yields available according to the operation temperature. In a more recent study, Gürüz et al.[97] tested a three multistep reaction mechanism to model isothermal pyrolysis of two lignites. These are also presented in Figure 2.12.

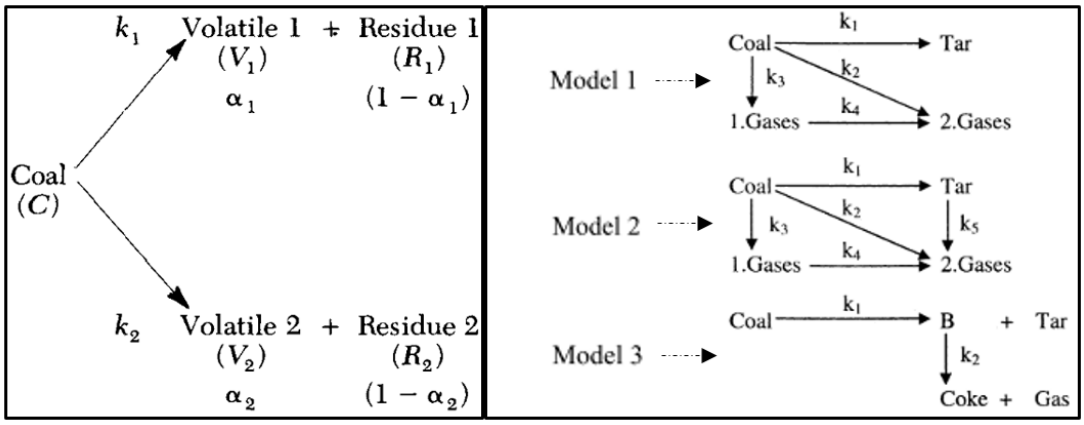

Figure 2.12. (Left) Kobayashi model for coal devolatilization where k: reaction rate constant, α: Mass stoichiometric coefficients [101]. (Right) Selected models for decomposition of coal in the study [97]

The distributed activation energy model (DAEM) assumes that the devolatilization is composed of independent and parallel reactions with different activation energies. It was first proposed by Pitt [102]. Anthony et al. [99,103] generalized the global reaction rate equation using activation energies that follows a Gaussian distribution. In time, distribution of activation energy used in DAEM is diversified using Weibull distribution [104] and Double-Gaussian distribution [105].

2.5.1.2. Phenomenological Models

Phenomenological models are capable of describing the devolatilization of the coal with the mathematical framework representing the organic matrix composed of aromatic structures connected by stable and labile bridges [106]. In these models,

decomposition of functional groups connected to organic matrix is attached to the release of light and heavy volatile species. Characteristic information of the parent coal structure, such as elemental analysis or C NMR, is required as an input. According to their approaches to devolatilization, there are four kinds of phenomenological models: Chemical percolation devolatilization (CPD) [10], FLASHCHAIN model [107], Functional-Group, Depolymerization, Vaporization, Cross-Linking (FG-DVC) model [108], Predictive multistep model [109]. These models can predict the volatile yield, tar yield, reaction rate and content of the devolatilization products.

CPD model is the only open source code among all the network models. CPD model uses the chemical structure of the coal to describe the rapid devolatilization process [10]. In the CPD framework, chemical structure of the coal with aromatic rings of various sizes and variety of chemical bridges is modelled using Bethe lattice (see Figure 2.13). Some of the bridges are ready to break at the beginning of the devolatilization while some remain until the end. C NMR analysis is used to obtain chemical structural information of the coal which includes the average molecular weight per side chain, the average molecular weight per aromatic cluster, the ratio of bridges to total attachments, and the total attachments per cluster. Since NMR data is not available for all coal samples, Genetti [110] developed a non-linear correlation to get NMR parameters using ultimate and proximate analysis.

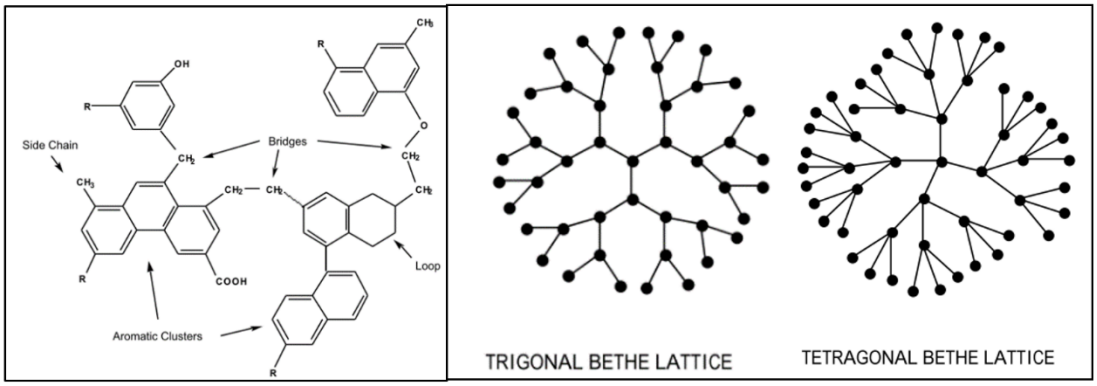

Figure 2.13. Representative chemical structure of the coal (Left) , and representative Bethe lattices (Right) [10]

FG-DVC model was first developed by Solomon [108]. This model combines a functional group model (FG) for gas evolution and tar formation model (DVC) which covers the depolymerization, cross-linking, external and internal transports. According to FG-DVC, formation of tar and gas species occurs simultaneously with the release or cross-linking of bridges in the tar. This synchronous operation includes 20 reactions. Like CPD model, FG-DVC uses the bethe lattice approximated by lattice statistics.

FLASHCHAIN model developed by Niksa and Kerstein [107] is composed of four reaction mechanisms, flash distillation and chain statistics. It is integrated into the commercial software PC Coal Lab distributed by Niksa Energy Associates LLC. Unlike the others, FLASHCHAIN model uses chain statistics instead of lattice statistics.

PoliMi is a multi-step kinetic mechanism model which provides conversion behaviors of various coals with no need to tune rate coefficients or the stoichiometry of the reactions. Detailed explanation of the approach PoliMi uses is available in the study done by Sommariva [109]. PoliMi differs from other empirical multistep models because of its predictive approach. There are three different reference coals defined in the PoliMi model. This set of coals (COAL1, COAL2, COAL3) and pure carbon (CHARC) form three triangles with overlapping edges, presented in Figure 2.14.

These reference species are selected to cover as many coals whose elemental C/H/O compositions are available in the literature as possible. Sample coal under study needs to be described as a combination of three of the closest reference coals. This is accomplished using linear interpolation.

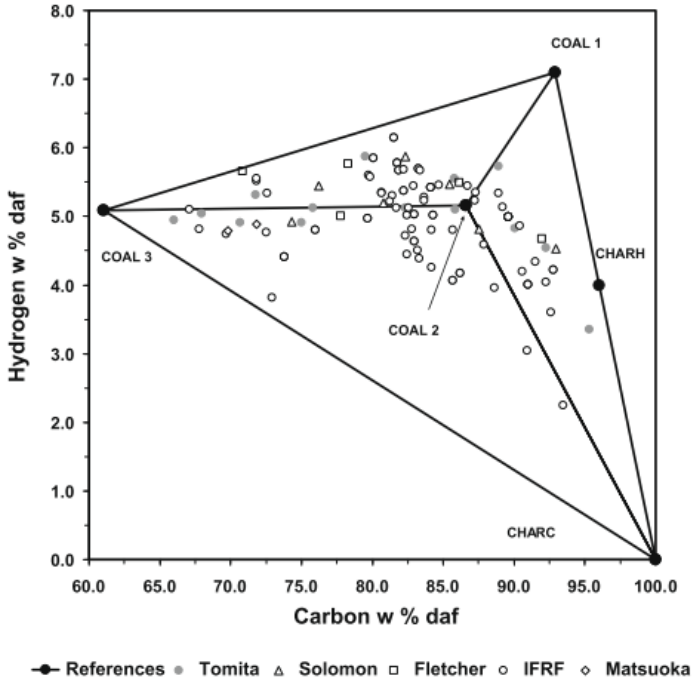

	C	H	O	C%	H%	O%
COAL1	12	11	0	0.929	0.071	0.000
COAL2	14	10	1	0.866	0.052	0.082
COAL3	12	12	5	0.610	0.051	0.339
CHARH	2	1	0	0.960	0.040	0.000
CHARC	1	0	0	1.000	0.000	0.000

Figure 2.14. Carbon and hydrogen contents of the reference coals used in the PoliMi model (solid symbols) and investigated coals in the literature (open symbols) [109]

Reaction mechanism of PoliMi has three main parts: pyrolysis of coal particle; secondary gas-phase reactions of the volatile matter; and heterogeneous char conversion. Pyrolysis process defined in PoliMi is shown in Figure 2.15. Other than the decomposition of functional groups in the metaplast phase, PoliMi contains cross-linking and annealing reactions to predict accurate chemical structure of the char.

Cross linking is the reconnection of released tar fragments to the coal lattice. Annealing is the deactivation of char due to the reorganization in the char structure. High temperature processes like combustion leads the reorganization of carbon atoms and loss of reactive sites [106]. After light volatile matter and tar released to the atmosphere, tar cracking and homogenous oxidation occur.

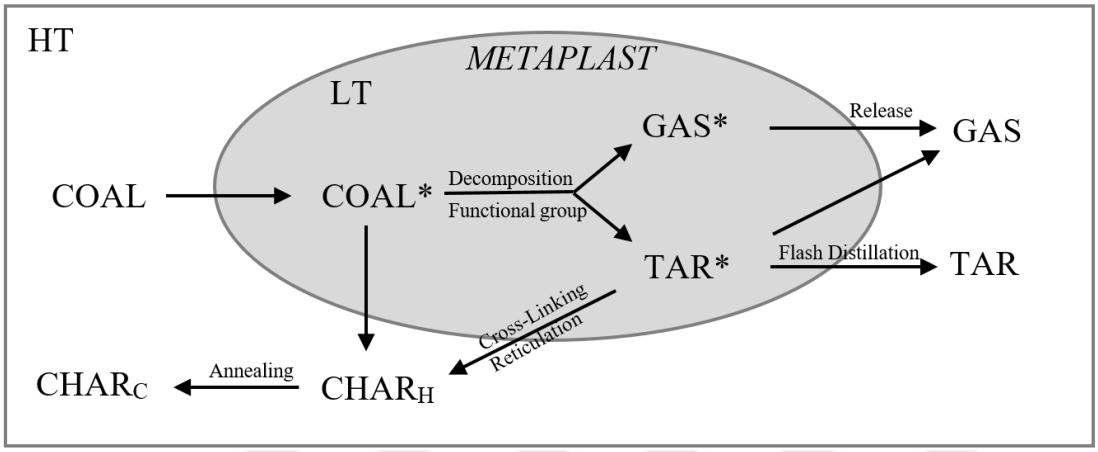

Figure 2.15. According to PoliMi model, coal decomposition mechanism [111]. LT: Low Temperature, HT: High Temperature

PoliMi model is a multi-step kinetic mechanism model which provides conversion behaviors of various coals with no need to tune rate coefficients or the stoichiometry of the reactions. Sommariva et al. [109] proposed PoliMi model for the first time, and validated the reliability of the model with a large set of experimental coal pyrolysis data obtained in different experimental rigs. Then, Maffei et al. [112] improved the multi-step coal pyrolysis kinetic mechanism adding sulfur and nitrogen compound release model. Maffei et al. [34] investigated the effect of operating conditions in the coal combustion using drop tube furnace. For the numerical part of the study, mass and heat transport equations were coupled with PoliMi kinetic model at particle scale. For both bituminous and lignite coals, model predictions showed a

good match with experimentally obtained particle life times for different O_2 mole fractions in O_2/N_2 mixture. In the recent study done by Debiagi et al. [113], PoliMi model predictions were compared with high temperature (1300ºC) air combustion and pyrolysis experimental data obtained using drop tube furnace. The model overpredicted the mass loss rate of the fuel sample, Colombian coal under air atmosphere whereas the model guess for volatile yield was higher than the experimental data.

2.5.2. Char Conversion Models

Char is the product of pyrolysis and contains only carbon and inorganics. Char conversion includes heterogeneous combustion and gasification reactions that take place on the char surface. As mentioned in section 2.3.1, the heterogeneous combustion reaction occurs in 3 stages: diffusion of oxygen molecules into the particle's pores, adsorption of oxygen molecules, and chemical reaction of carbon with oxygen. Thus, the diffusion rates of the reactant and product gases are as important as the intrinsic kinetic rates of the heterogeneous reactions. There are phenomena, which occurs concurrently to the char conversion, and affect these rates. Prior to the brief description of the most widely used models for char conversion, these phenomena need to be mentioned . The most important conversion phenomena are,

- Morphological changes: morphological properties of char, which includes char diameter, porosity, mean pore diameter and tortuosity, change during conversion, and influence the conversion rate. As an example, higher tortuosity leads lower pore diffusion rate of reactant and product gases during conversion since tortuosity is defined as the ratio of actual flow path length to the straight distance between the ends of the flow path in the particle [114]. Moreover, the total surface area of the particle depends on the morphology, and higher surface area leads to a higher number of available carbon sites for conversion.

- Thermal annealing: thermal annealing is the deactivation process of organic-based solid fuel at high temperatures that reorganizes the carbon structure into

a more graphite-like structure [115]. This process causes a loss of active carbon sites [115–118].

- Ash inhibition: the ash content of the char that increases with the increase in conversion results in lower area of available carbon surface [119]. Moreover, inert ash layer causes a resistance to diffusion of oxygen into the core of the char at high conversion levels [119].

The carbon burnout kinetics (CBK) model family is one of the most widely used char conversion models for oxy- fuel [120], air combustion [121] and gasification [122] since it considers several phenomena which happen during char conversion. It was originally proposed by Hurt et al. [119] in 1998. Recently, the CBK/E model was introduced. In this model, Langmuir- Hinshelwood (LH) mechanism is coupled with thermal annealing and pore evaluation models to predict reaction kinetics. A single film model is used to describe the transport processes of gas species in the boundary layer of the particle, and ash inhibition effects are considered. There are two methods to describe pore diffusion on kinetics [106]: numerical solution of species transport equations along with the fuel particle [34], or Thiele modulus approach [80]. The CBK/E uses the Thiele modulus approach along with a parallel path pore model.

The PoliMi model is a semi-empirical kinetic reaction model which is quite easy to use compared to other well-known combustion models, and was developed by [111]. Moreover, in contrast with devolatilization and char conversion, i.e. stage-specific models, the PoliMi model simulates both volatile and char combustion stages at the same time. Heterogeneous reactions of the residual char include thermal annealing, gasification, and combustion, as listed in [34]. Moreover, there are three types of char species with different chemical structure and composition as a result of the devolatilization conditions. The reaction mechanism and rate coefficients for heterogeneous char combustion are validated using a large number of experimental results [111]. Maffei et al. [34] used the PoliMi model to simulate coal combustion in a drop tube furnace under O2/N2 and O2/CO2 atmospheres. In order to include diffusion limitations into the simulations, energy and mass transport equations are solved at the particle scale. The model predictions showed an overall good agreement

with experiment data. According to the recent study done by Debiagi et al. [113], PoliMi model predictions are compared with high temperature (1300ºC) air combustion and pyrolysis experimental data obtained using drop tube furnace. The model overpredicted the mass loss rate of the fuel sample, Colombian coal, under air atmosphere and the guess for volatile yield was higher than the experimental data.

CHAPTER 3

EXPERIMENTAL METHODOLOGY

3.1. Fuel Preparation and Characterization

In the scope of this thesis, the combustion kinetic experiments are proceeded for four different coal samples; Soma lignite (SL), Tunçbilek lignite (TL), Afşin Elbistan lignite (AEL) and Rhenish lignite (RL). Fuels are selected to be representative for different regions. Tunçbilek, Soma and Afşin Elbistan lignites are from the Turkey's own mines. While Turkey Coal Enterprises (Türkiye Kömür İşletmeleri) provides Soma lignite (Manisa) and Tunçbilek lignite (Kütahya), AEL is from Afşin-Elbistan power plant. Rhenish lignite is supplied by Rheinisch-Westfälisches Elektrizitätswerk (RWE), the operator of Rhenish lignite mine.

Received fuels were ground using different types of grinders located in mineral processing laboratory in Mining Engineering, METU. There are 2 types of crushers suitable for coal samples: one-roller crusher and ball-mill crusher (Figure 3.1). Each has its own advantages. While one-roller crusher is similar to industrial coal crushers and more suitable for mass grinding, ball-mill crusher can grind stiff coals like Afşin-Elbistan lignite. One should choose proper crusher depending on the stiffness of the coal. The ground coal was sieved using Retsch brand sieve sets and the Retsch sieve shaker located in Mining Engineering, METU (Figure 3.2). The fuel samples were stored in glass vials in a particle size range of 106-125 μm. In order to validate the reliability of sieving procedure, particle size analysis was done using Marvern Mastersizer 2000 in the Central Laboratory (Merlab) of METU.

Figure 3.1. One roller crusher (Right) and ball-mill crusher (Left)

Figure 3.2. Retsch brand sieve set and sieve shaker which used for preparation of coal samples

Before experiments, the sample fuel was left to dry (105 ºC in ash furnace) overnight. Drying process is necessary to remove excess moisture in the fuel. It is important to avoid the effect of moisture on the experimental results. After drying, fuels still retrieve specific amount of moisture from the air/ environment (0-5%). For each coal, this residual moisture content varies.

The proximate analysis of the fuels was done using Perkin Elmer 4000 thermogravimetry analyzer and following the procedure described in [15]. The ultimate analysis was obtained using a Leco CHNS-932 elemental analyzer in the

Central Laboratory of METU. The muffle furnace in Clean combustion technologies laboratory was used to get ash contents of the fuels (standard TS EN 15309). Proximate analysis, ultimate analysis and ash contents of the fuels are shown in Table 3.1. AEL and RL have highest and lowest ash contents, respectively. TL and SL share very similar ash contents. Ratio of VM/FC separates the fuels into two groups: below 1 (TL and SL) and above 1 (AEL and RL).

Table 3.1. Proximate analysis, ultimate analysis, heating values and mean particle diameters of the fuels: Tunçbilek lignite, Soma lignite, Afşin- Elbistan lignite, Rhenish lignite

	Parameter	Tunçbilek lignite(TL)	Soma lignite(SL)	Afşin- Elbistan lignite (AEL)	Rhenish lignite(RL)
Proximate analysis [as received %]	Moisture	2.8	2.0	4.6	5.4
	Volatile matter	31.1	38.4	34.9	47.9
	Fixed carbon	52.1	44.1	18.1	43.8
	Ash	14.0	15.5	42.4	2.9
Proximate analysis [ash free %]	Moisture	3.3	2.4	8.0	5.6
	Volatile matter (VM)	36.2	45.4	60.6	49.3
	Fixed carbon (FC)	60.6	52.2	31.4	45.1
	VM/FC	0.6	0.9	1.9	1.1
Ultimate analysis [dry, ash free %]	C	71.8	70.4	52.3	67.8
	H	6.5	5.4	5.4	5.2
	N	3.1	1.2	1.4	0.7
	S	1.7	1.5	7.1	0.3
	O[a]	16.9	21.5	33.8	26.0
Heating Values[b] [MJ kg^{-1}]	Low	24.3	22.5	10.5	23.6
	High	25.6	23.5	11.2	24.7
Particle size Analysis [μm]	d_{50}	110	110	110	110

[a] Obtained by subtraction

[b] LHV and HHV are calculated using the method developed by Srivastava [123] and tested for Turkish coals by Bilgen et al. [124]

The location of each fuel on the Van Krevelen diagram (see Figure 3.3) shows that AEL is in the peat-biomass common zone and TL is out of all zones. This is because Van Krevelen diagram was drawn with the known solid fuel feedstock and AEL and TL were not included. RL and SL have close positions to each other on the figure, like their ratio of VM/FC. Since RL has higher oxygen content, its VM/FC ratio is higher than SL.

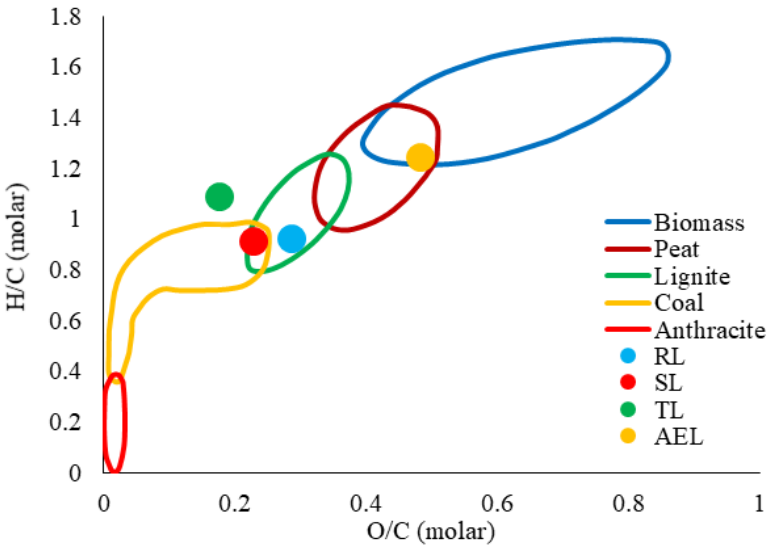

Figure 3.3. Sample fuels on the Van Krevelen diagram

3.2. Experimental Apparatus

3.2.1. Drop Tube Furnace (DTF)

A sketch of the drop tube furnace setup is given in Figure 3.4. The drop tube furnace setup consists of the drop tube furnace itself, a feeding unit, and a collection unit. The alumina tube of the drop tube furnace has length of 1750 mm and inner diameter of 75 mm. Middle part of the tube (1000 mm) is surrounded by SiC and $MoSi_2$ heating elements and can be heated up to 1500 ºC. A thermocouple is placed at mid length of the hot zone to control the wall temperature. By using a thermocouple

probe, tube wall temperature was measured at different points and it was seen that the temperature was constant along the hot zone.

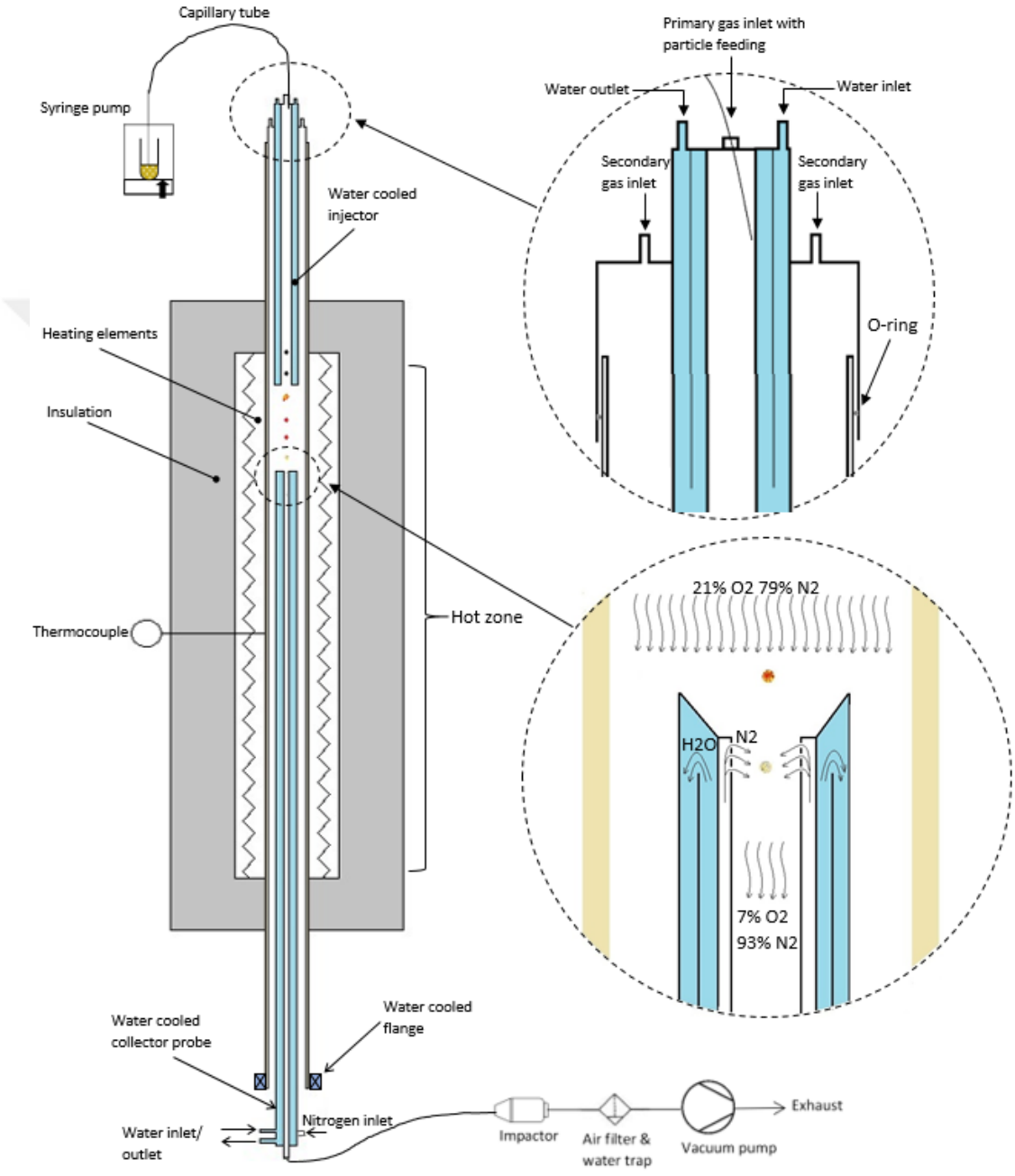

Figure 3.4. *S*ketch of drop tube furnace and its accessories

Figure 3.5 shows the injector located at the top of alumina tube of DTF, part of the feeding unit. It has water inlet and outlet to circulate cold water in it and keep its temperature low. Thus, sample fuel flows through injector with constant temperature (20 ºC) and is exposed to high heating rate (10^4-10^5 C/min) when it left the injector. High heating rate is important for the realistic solid fuel combustion experiments because industrial furnaces also treats the solid fuels with high heating rates. For this study, wall temperature of DTF is set to 1000ºC which is expected to provide char combustion in zone II (see Figure 2.5) according to [125] . The primary inlet air flow (4 L/min) is necessary to feed the sample fuel. The secondary inlet air flow (16 L/min) provides the sufficient oxygen content for the combustion. Also, the secondary flow keeps particle on its path to the end. Without the secondary flow, particles would be under the buoyancy effects near the wall.

Biot number for heat transfer (Bi_h), an non-dimensional number to compare the conduction in a fuel particle and the convection at its surface, is calculated based on experimental conditions (see Appendix A), found as 0.09, 0.11, 0.14, 0.11 for TL, SL, AEL and RL, respectively. In the calculation of Bi_h, it is assumed that the velocity of the fuel particle and the gas flow are same, as found in the study done by Wang et al. [48]. Since Bi_h is much smaller than 1, the internal temperature distribution in fuel particle is uniform.

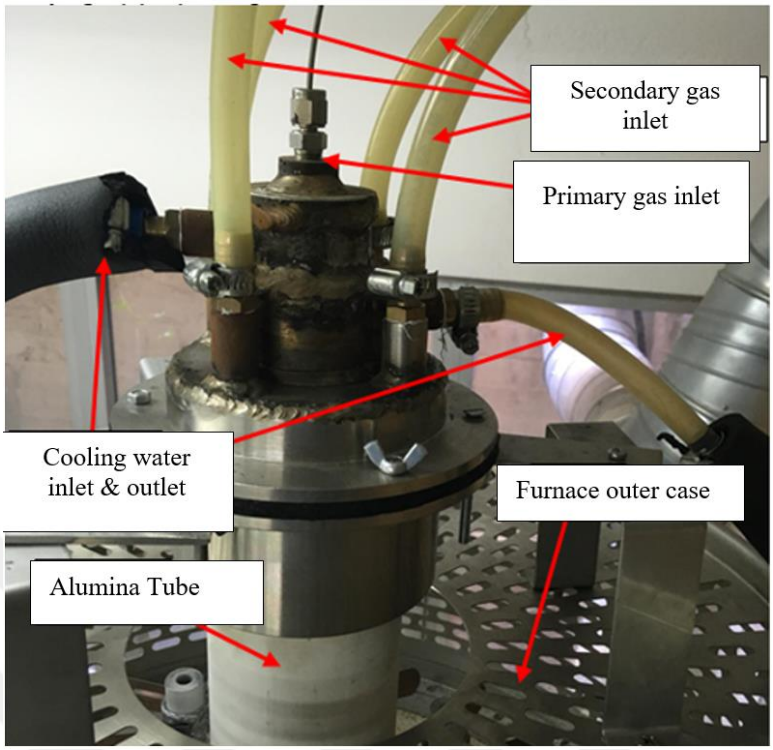

Figure 3.5. *W*ater cooled injector assembled to the alumina tube

In the scope of this study, inlet gas was always air. In order to feed air independent to the ambient conditions, gas cylinders are used in the experiments. Inlet gas flow rates are controlled by using computer aided flow controllers. While secondary inlet gas flow goes directly to the furnace, primary inlet flow passes the fuel feeding system and carry fuel particles to the furnace. Fuel feeding system (see Figure 3.6) consists of capillary tube, vibration motor, mixing chamber, syringe pump and test tube. Incoming secondary gas flow passes through mixing chamber and goes below to the sample tube. Then, gas flow goes out of mixing chamber via capillary tube which is the only way out. Vibration motor vibrates the test tube and cause coal particles to fly around in the mixing chamber. Since coal particle sizes are very small in the experiment, incoming gas can carry the particles to the exit.

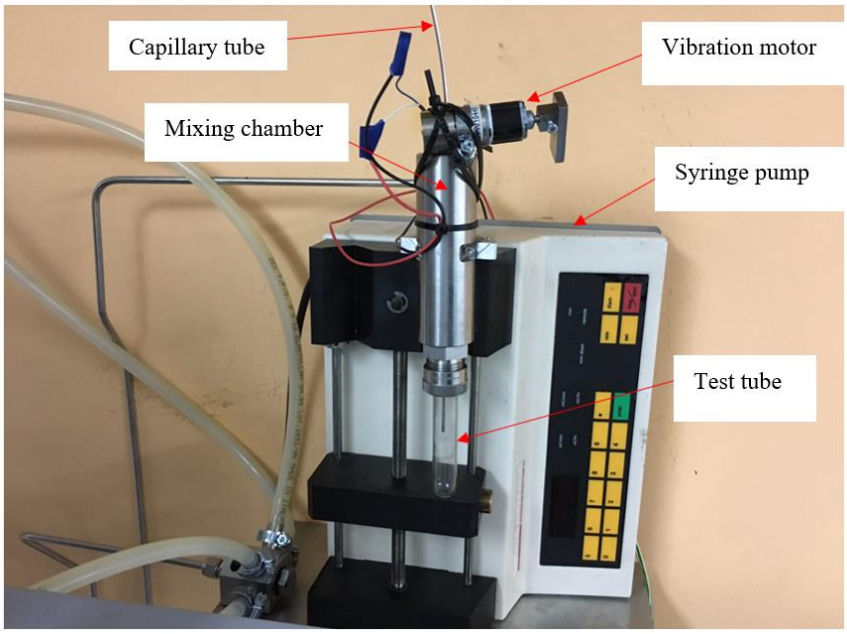

Figure 3.6. Fuel feeding system with its components

ISISO brand water chiller is used as cooling unit. The cold water comes from cooling unit separates into three different directions; collector probe, injector, flange. Then it returns to the cooler unit to complete the closed circuit.

Analyzing fuel particles which last in DTF for different residence times is the way to understand combustion characterization of the fuel. In the literature [48], water cooled collector probe placed in the DTF and vacuum pump to suck the fuel particles through water collector probe are used for combustion characteristic experiments. Particle collection system includes water cooled collector probe, impactor and vacuum pump. A water-cooled and nitrogen-quenched stainless steel collection probe was used to collect particles along the centre axis of DTF (see Figure 3.4). Nitrogen quenching decreases the oxygen content of environment from 21 vol% to 7 vol% at the tip of collector probe (see Appendix B). Due to dimensional restrictions, the collection probe can reach up to 22 cm from the tip of the injector. The probe has small holes at its tip to quench the solid fuel conversion through nitrogen injection. The gas content in the collection probe is calculated as 7% O_2 and 93% N_2 with an assumption

of negligible offgas amount from solid fuel conversion (see Figure 3.4). The solid sample was extracted along the collector probe via a Tecora vacuum pump and collected on quartz microfiber filters placed in a Tecora single stage impactor (filter holder). During the experiments, the impactor was wrapped with the heating wire in order to avoid the moisture condensation on the filters. After weighting the filter with the solid sample on it, ashing was done following ASTM D3174 standard. Burnout data was calculated as follows;

$$\text{Burnout}\ [-] = \alpha = \frac{1 - w_i * \frac{w_b}{w_a}}{1 - w_i} \tag{21}$$

Where w_i is the ash weight fraction of the input coal. w_b and w_a are respectively the sample weights on the filter before and after ashing of collected sample.

Pyrolysis experiments done in the scope of this study is categorized as a flash pyrolysis due to particle temperature (1000ºC) and heating rate (~10^4 ºC/s) DTF provides [126]. Char samples are collected using stainless steel laboratory funnel at the outlet of the furnace. The funnel with same diameter as the ceramic drop tube avoids any oxygen flow coming from outside of DTF. Same primary and secondary inlet flow rates are used for combustion experiments. Collected chars are burned to ash to calculated high temperature volatile yield (HTVL) as follows:

$$\text{HTVL}\ [\%] = \left(1 - w_i \frac{w_b}{w_a}\right).100 \tag{22}$$

For consistency, all combustion and pyrolysis experiments are repeated in this study.

3.2.2. Thermogravimetric Analyzer (TGA)

The low heating rate combustion experiments are carried out by using a TGA (Perkin Elmer, model Pyris STA 4000). Detailed sketch of a Perkin Elmer TGA 4000 (top-loading) is shown in Figure 3.7. For the sake of precision, approximately 4.3 (+/-

1) mg of sample fuel under 100 mL/min air flow is used in each experiment. The weight loss of the sample fuel was recorded from 30 ºC to 800 ºC with heating rates of 5 ºC/min, 10 ºC/min, 15 ºC/min, 20 ºC/min. Preliminary tests are done in order to be sure that the results had good reproducibility under these experimental conditions. Since heating rate limitations emerged for heating rates higher than 20 ºC/min, this study focused on the combustion kinetics of the coal under heating rates below 20 ºC/min.

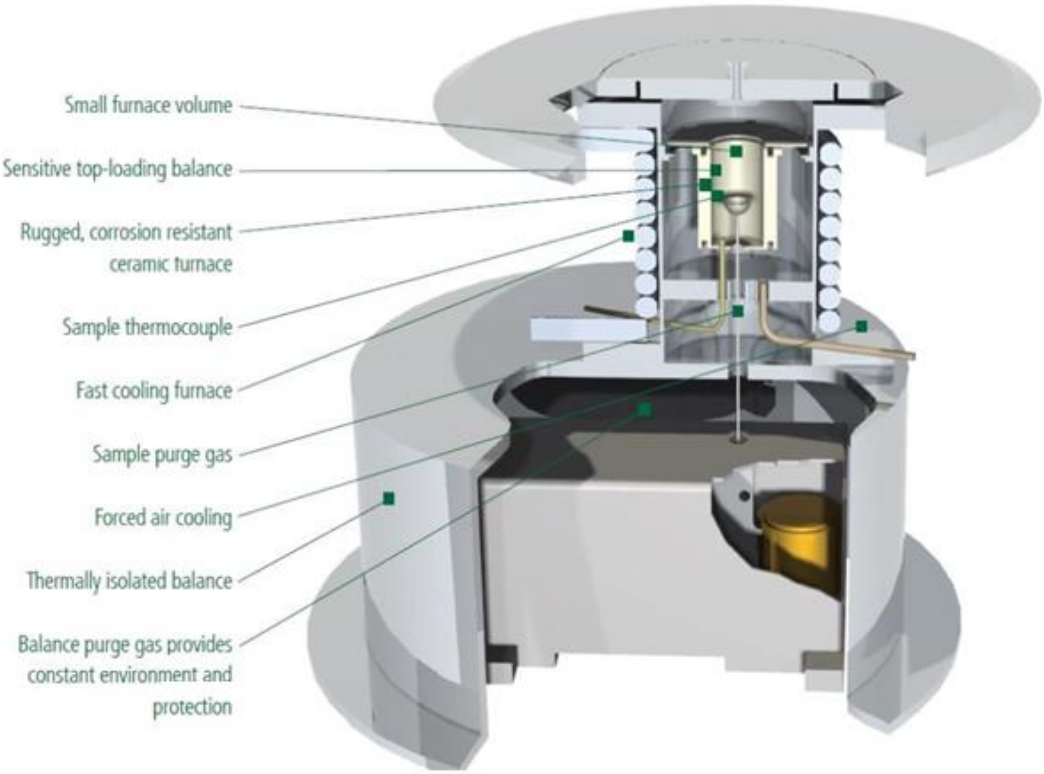

Figure 3.7. Thermogravimetric analyzer (TGA): Perkin Elmer TGA 4000 [127]

Mass loss up to 200 ºC is accounted for the evaporation of the moisture. The mass increase observed in the temperature range of 200-300 ºC is the result of oxygen adsorption [128]. The magnitude of the change in mass is also an indicator of self-oxidation potential [129]. Depending on the compositional and structural features of the fuel, devolatilization and char oxidation can occur as simultaneous or separate

processes. The DTG peak at 600-860 ºC can be attributed to the decomposition of calcium-carbonate ($CaCO_3$) [130].

CHAPTER 4

NUMERICAL METHODOLOGY

4.1. Reacting Fluid Flow modelling

This section explains the procedure followed to model non-reacting flow in DTF. The modelling part of this study is carried out using ANSYS FLUENT. The aim of this analysis is to obtain temperature and velocity profiles of the particle fed into the DTF, that were later used as input for the PoliMi model (see section 4.2). In order to have accurate results, geometry and boundary conditions are defined as similar to the real experimental setup as possible, as described in the following subsections.

Figure 4.1 illustrates the procedure followed to obtain the conversion profiles by means of weight [%] and derivative weight [%/min]. This procedure includes usage of the DTF experimental results, CFD analysis and Polimi model together. After building CFD model with proper geometry, mesh structure and sub-models for coal combustion in fluid flow, the Arrhenius constants in the intrinsic char oxidation model are set same as the values available in PoliMi kinetic mechanism (see Appendix E). Under these conditions, Fluent is run. Burnout lifetime of the fuel is obtained and compared with the burnout lifetime experimentally obtained from DTF experiments. By changing the pre-exponential factor, simulation rerun until the difference between two burnout lifetimes are relatively small. Then, the particle temperature profiles as a function of residence time ,which Fluent provides, is used as an input for the PoliMi model in order to obtain main modelling output graphs: Time vs Weight [%] and Time vs Derivative Weight [%/min].

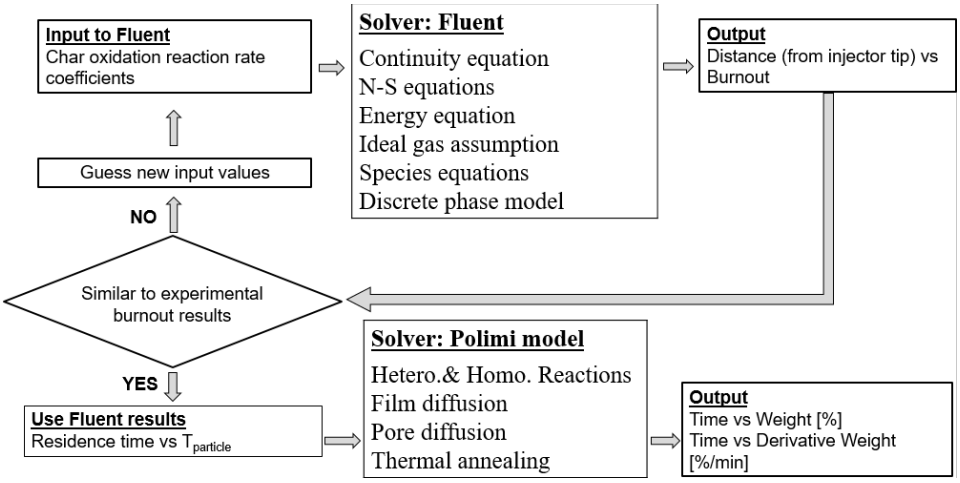

Figure 4.1. Modelling procedure including reactive fluid flow modelling and single particle combustion modelling

4.1.1. Domain and Boundary Conditions

The 3D geometry of the DTF (Figure 4.2) is defined using geometry tools in ANSYS. There are no simplifications done on the geometry of DTF. In order to have accurate velocity and temperature values for primary and secondary flows at the inlet of hot zone, geometry of the injector and alumina tube are added in the DTF geometry. Therefore, there are four different zones in the geometry: water domain in the injector, air domain in the alumina tube, steel injector, alumina tube. It is intended to add the effect of the heat transfer by axial conduction on alumina tube, so that preheated secondary flow can be obtained. Table 4.1 lists the boundary conditions used for CFD analysis.

There are two simplifications done on the boundary conditions that should be mentioned: the inlet zone and the outlet zone. Firstly, the inlet zone of the DTF is defined as an adiabatic wall, even though it is cooled down due to free convection on its outer wall. This assumption leads to hotter secondary air inlet flow than expected in the hot zone. Secondly, at the outlet zone, the collector probe is not added into the geometry. Since the collection probe is water cooled and nitrogen quenched, it is assumed that the coal particle cools down instantly. Nitrogen quenching decreases the

oxygen content of environment from 21 vol% to 7 vol% at the tip of collector probe. Thus, combustion reactions slow down instantly.

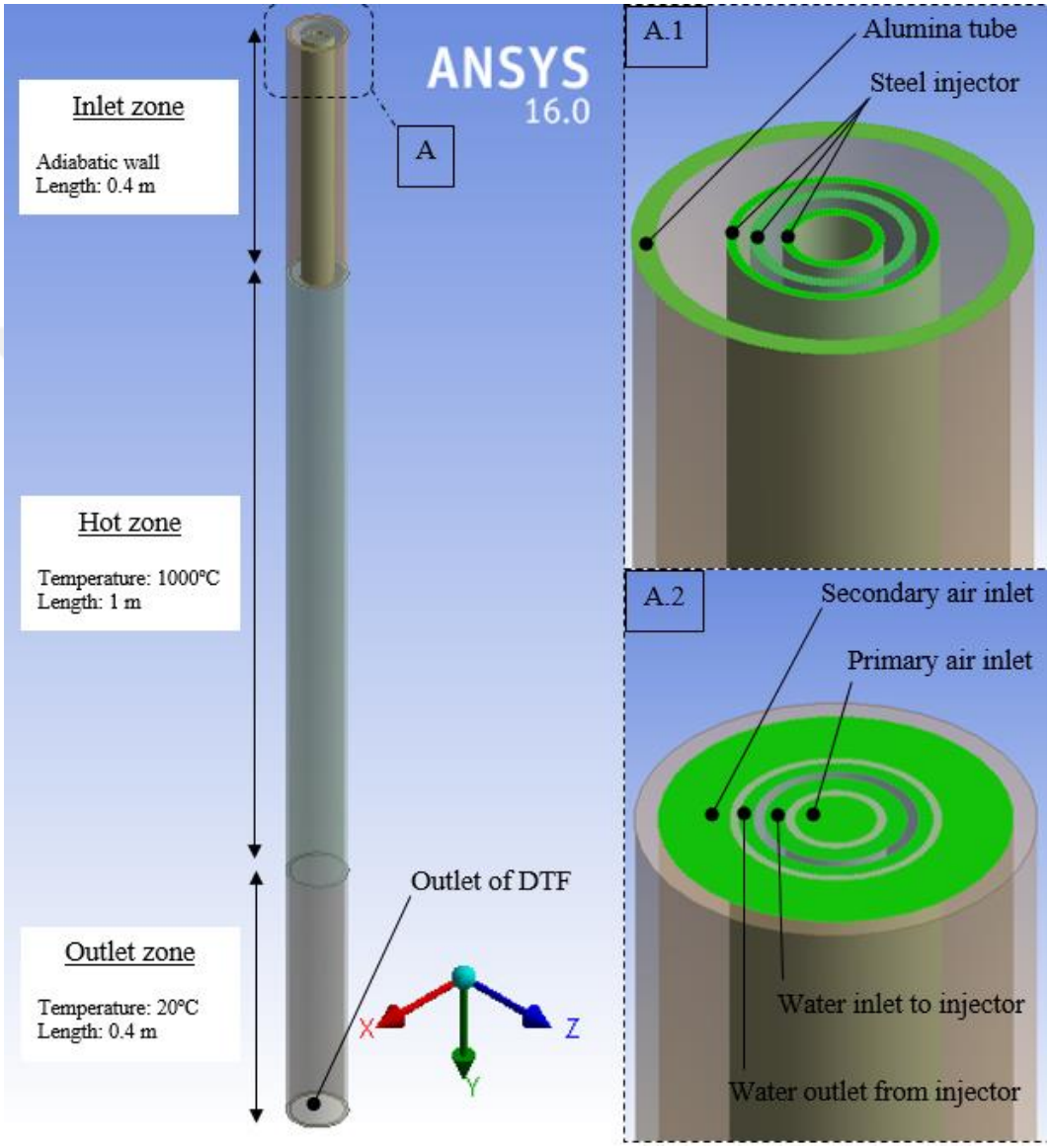

Figure 4.2. Drop tube furnace geometry and boundary conditions

Table 4.1. Boundary conditions of the CFD analysis for the domain mentioned in Figure 4.2

Boundary name	Boundary condition	Value
Primary air inlet	Mass- flow-inlet	$8x10^{-5}$ kg/s
Secondary air inlet	Mass- flow-inlet	$32x10^{-5}$ kg/s
Air outlet	Pressure-outlet with target mass flow	$4x10^{-4}$ kg/s
Water inlet	Mass- flow-inlet	0.1 kg/s
Water outlet	Pressure-outlet with target mass flow	0.1 kg/s
Inlet zone	Wall with constant heat flux	0 W/m^2
Hot zone	Wall with constant temperature	1000ºC
Outlet zone	Wall with constant temperature	300ºC

4.1.2. Computational Mesh

The computational mesh is created using ANSYS meshing tool. Since there are many interphase surfaces in the geometry, mesh type is not specified to only one mesh element type. Alumina tube and the injector are meshed with hexahedron elements while wedge and tetrahedron mesh elements are used for the rest. In order to capture near wall boundary layer gradients, inflation layer meshing is used for the air domain near the inner surface of alumina tube.

4.1.3. Solver Settings

Related non-dimensional numbers are calculated to understand what types of flow and heat transfer exists in DTF. These calculations are available in Appendix A. Selected non-dimensional numbers (Reynolds number (Re), Grashof number

(Gr), Rayleigh number (Ra) and Prandtl number (Pr)) are calculated and given by Table 4.2. Gr_L/ Re_L^2 is the parameter used to compare the importance of natural convection with forced convection. If Gr_L/ Re_L^2 is higher than 1, natural convection is dominant. Based on Table 4.2, natural convection is dominant on the heat transfer in the hot zone of DTF. Rayleigh number is used to know whether the natural convection boundary layer is laminar or turbulent. Since calculated Ra value is around critical Ra value (10^9), it is concluded that the boundary layer due to natural convection is in transition region.

Table 4.2. Calculated non-dimensional numbers for the flow in DTF: Reynolds number, Grashof number, Rayleigh number, Prandtl number

Reynolds number (Re_L)	Grashof number (Gr_L)	Gr_L/ Re_L^2	Rayleigh number (Ra_L)	Prandtl number (Pr)
2050	1.95×10^9	466	1.34×10^9	0.69

CFD analysis of DTF is performed under steady- state conditions. According to calculated non-dimensional numbers (Table 4.2), natural convection is dominant on the heat transfer in the hot zone of DTF, and the natural convection boundary layer is in the transition region, so the flow in the DTF is modelled as turbulent flow using K-ε realizable model. Pressure- velocity coupling is achieved using Coupled algorithm. Coupled algorithm provides an implicit method to solve the momentum and pressure-based continuity equations together [131]. Primary and secondary flow rates are defined same as experimental conditions (see Section 3.2.1). The boundary conditions for the energy equation are as seen in table 4.1. Since radiation heat transfer has an important effect on the coal combustion in drop tube furnace, radiation heat transfer is implemented into the simulation with the discrete ordinate (DO) model. DO model solves the radiative transport equation for a set of discrete directions, each associated with a solid angle. The number of divisions for both polar and azimuthal angles are selected as 4, as suggested for more reliable results in the user guide [131]. For this 3D model, radiative transport equation solved for 128 directions. The control volume face defined for each direction are divided into pixels. For the geometries involving

symmetry, recommended values (3x3) are used [131]. Alumina tube and the injector are defined as gray, opaque and diffuse boundary condition with zero absorption coefficients. Emissivity and scattering factor of the fuel particles are defined as 0.95 and 0.9 according to the study [132]. The governing equations Fluent solves to simulate the DTF experiments are available in Appendix C.

Injected pulverized coal particles are tracked in the Lagrangian frame with random walk model. The heat and mass transfer of the coal particles are not coupled with continuous phase. In this case, the coal particles can change by heat and mass transfer, but these changes do not affect the air flow [131]. CFD analysis was performed with a diluted particle flow of 12 g/h feeding rate.

Species transport model with defined volumetric and particle surface reactions is used to solve species equations for the selected species: volatile, O_2, CO_2, H_2O, N_2, H_2, CO. Coal calculator tool is used to set the relevant input parameters for Species and Discrete Phase models. Proximate and ultimate analysis of the fuels are given as inputs in this tool. The one step intrinsic combustion model is used to simulate the whole conversion process. For each fuel, Arrhenius constants in CFD analysis are tuned to obtain the same burnout time as the experimentally measured burnout time (as explained in section 4.1).

In order to achieve convergence in the CFD analysis, the simulations are started by solving K-ε realizable model equations, energy equation with DO model with first order discretization method and Species transport model equations. After the solution is converged, discretization method is switched to the second order, and discrete phase is defined. This process is followed using residual monitors, as seen in figure 4.3. Absolute convergence criteria are set to 10^{-3} for all residuals in figure 4.3. Average time per iteration is calculated as 30 sec.

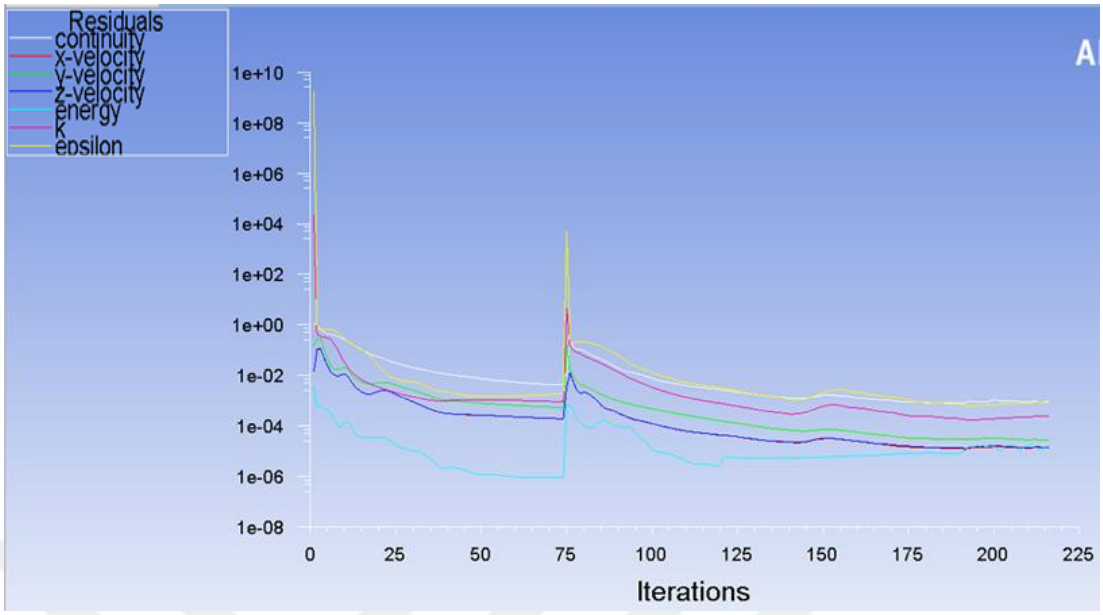

Figure 4.3. Drop tube furnace geometry and boundary conditions

4.1.4. Mesh Independency

Mesh independency of the results is done by comparison of the velocity and temperature profiles for three different meshes: coarse, medium and fine mesh. There are some parameters that are representative of the mesh quality, such as aspect ratio and skewness. Aspect ratio is defined as the ratio among the side lengths of the element. Skewness is defined as the difference between the shape of the mesh element and the equilateral mesh element with same volume. Properties of these meshes are given in Table 4.3.

For mesh independency study, discrete phase model and species transport model are deactivated. Non-reactive hot flow in the DTF is modelled.

Table 4.3. Properties of the chosen meshes

	Coarse mesh	**Medium mesh**	**Fine mesh**
Number of elements	292,066	1,790,511	8,622,017
Average Skewness	0.22	0.18	0.18
Average Aspect ratio	2.96	3.04	2.33

Figure 4.4 displays the axial velocity and temperature profiles obtained using the coarse, medium and fine mesh constructions. Compared to coarse mesh, analysis done with medium and fine meshes show lower fluctuations in the axial velocity profile. It is expected that the fine mesh enables to calculate more accurate velocity magnitudes than coarse and medium meshes. After the injector (0.0-0.4m), axial velocity value calculated with the fine mesh has sudden increase and gets constant. On the other hand, it takes around 0.2 m to reach a constant axial velocity value for the medium mesh. Due to excessive fluctuations, coarse mesh does not reach constant axial velocity value. The lower axial velocity values right after the injector leads higher heating rate in the temperature profile for both coarse and medium meshes.

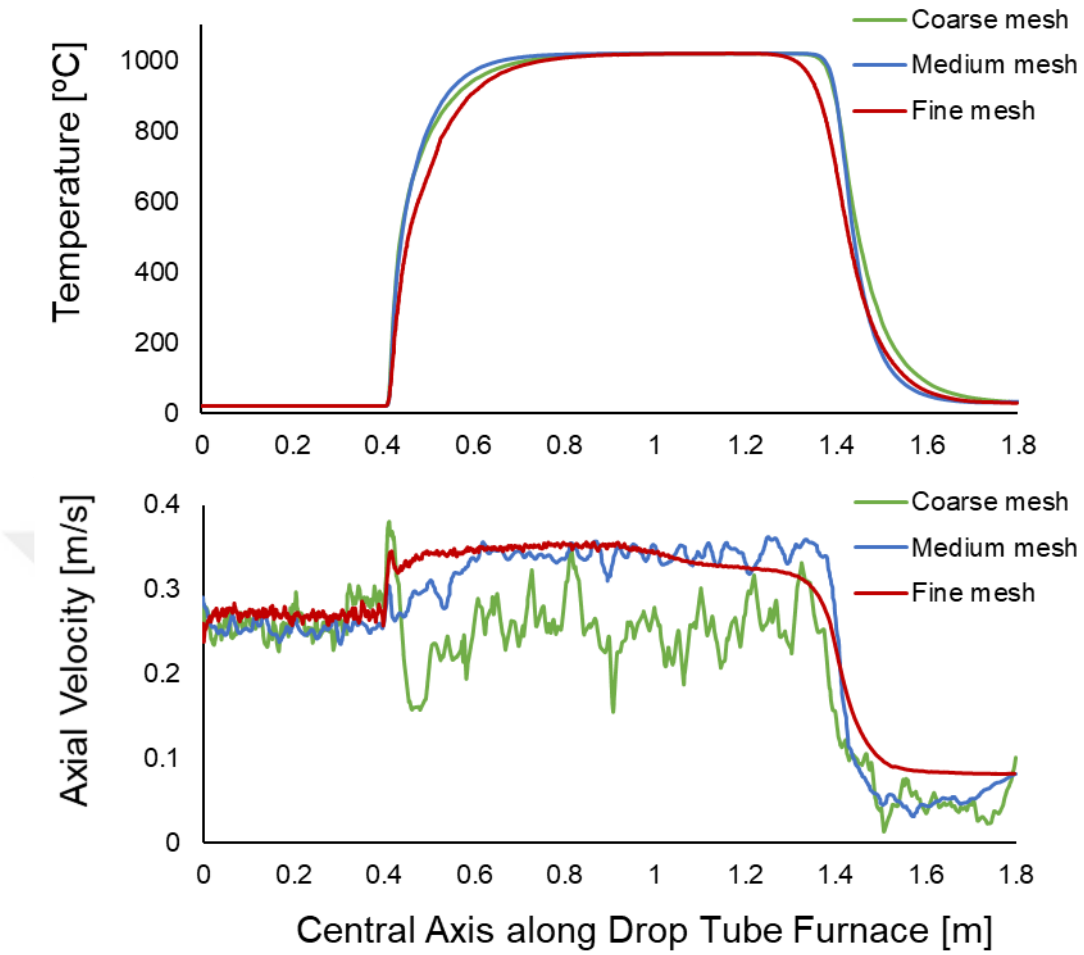

Figure 4.4. Temperature and axial velocity distributions along central axis of drop tube furnace obtained with two different mesh structures: Coarse, Medium and Fine meshes

Figure 4.5 displays the mass flow rates calculated at different cross sections in DTF. Compared to the medium and fine meshes, coarse mesh gives lowest mass flow rate values which attributed to that coarse mesh cannot satisfy the continuity in the air domain of DTF. Although fine mesh construction gives more accurate results on velocity and temperature distribution, computational cost considerations lead the study to use the medium mesh which gives acceptable axial velocity profile. The necessary times per iteration are 3, 8 and 45 seconds for coarse, medium and fine mesh, respectively. Figure 4.6 shows the cross section of the medium mesh construction at the end of mesh independency study.

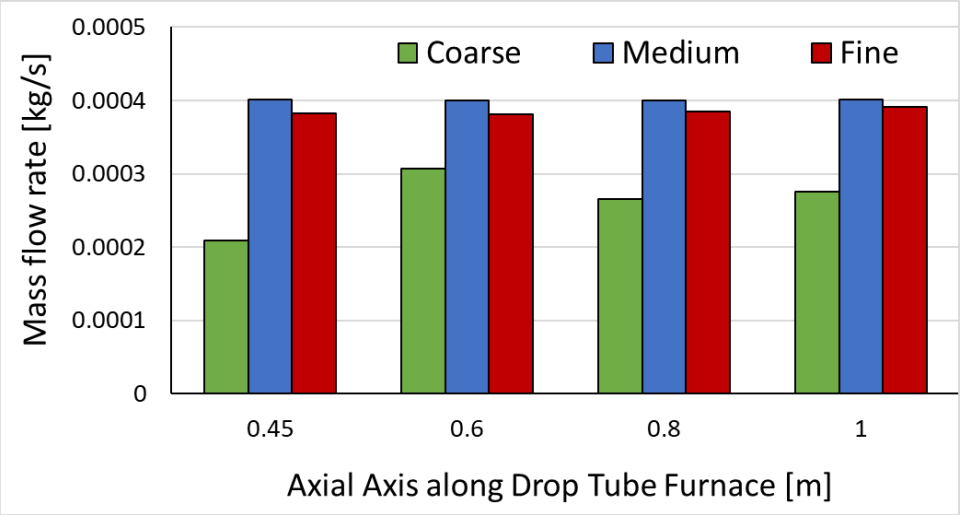

Figure 4.5. Mass flow rates at different cross sections in DTF

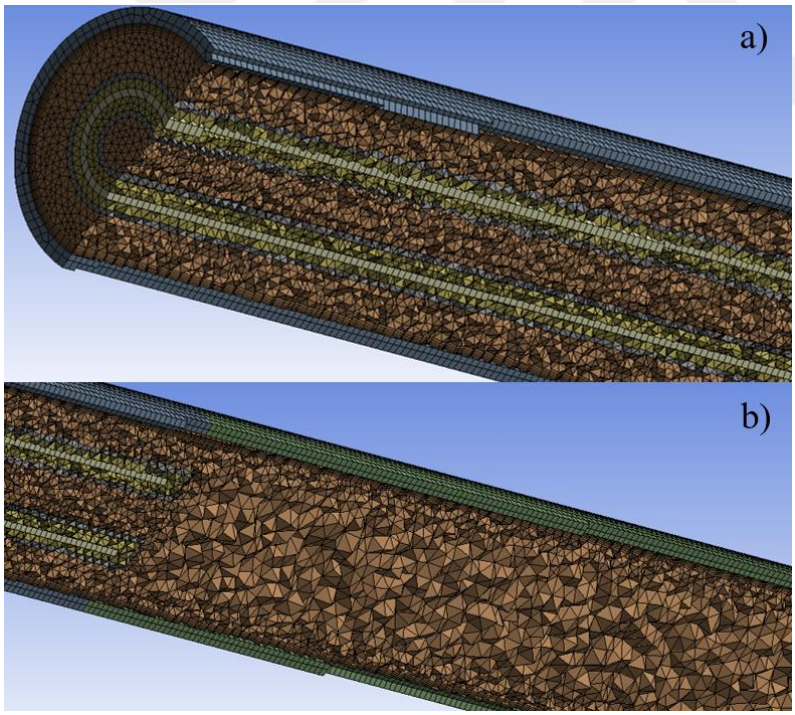

Figure 4.6. Cross section of the mesh structure used for CFD analysis: a) inlet zone b) hot zone

4.1.5. Sensitivity Analysis

Sensitivity analysis of CFD analysis is done only for simulations of Rhenish lignite to find out how the variations in the inputs of intrinsic char combustion model can affect the outputs. The temperature profile as a function of time is chosen as an output of CFD analysis in the sensitivity analysis.

Table 4.4 shows the pre-exponential factor [1/s] and activation energy [J/mol] combinations used for sensitivity analysis. In order to see the effect of these parameters, different combinations are created based on the reference combination, named as 'Used'. Sensitivity of CFD analysis on one parameter is done by changing it gradually and keeping the other one constant.

Table 4.4. Magnitudes of pre-exponential factors and activation energies used for the sensitivity analysis on the CFD simulation of Rhenish lignite (RL)

		Pre-exponential factor, A [1/s]	**Activation Energy, E [J/mol]**
Used		4500000	34000
Pre.1	-10%A	4050000	34000
Pre.2	-20%A	3600000	34000
Pre.3	+10%A	4950000	34000
Pre.4	+20%A	5400000	34000
Act.1	-10%E	4500000	30600
Act.2	-20%E	4500000	27200
Act.3	+10%E	4500000	37400
Act.4	+20%E	4500000	40800

Figure 4.7 shows the particle temperature profiles as a results of usage of each pre-exponential factor and activation energy combinations in Table 4.4. 20% change in pre-exponential factor causes around 100ºC increase at peak temperature and around 20% decrease at burnout time. On the other hand, 20% change in activation energy causes around 270ºC increase at peak temperature and around 50% decrease at burnout time. Thus, CFD analysis is more sensitive for activation energy than pre-

activation factor. Moreover, the particle temperature is constant in the hot zone for the activation energy with above 10% increase. This is the sign of incomplete combustion.

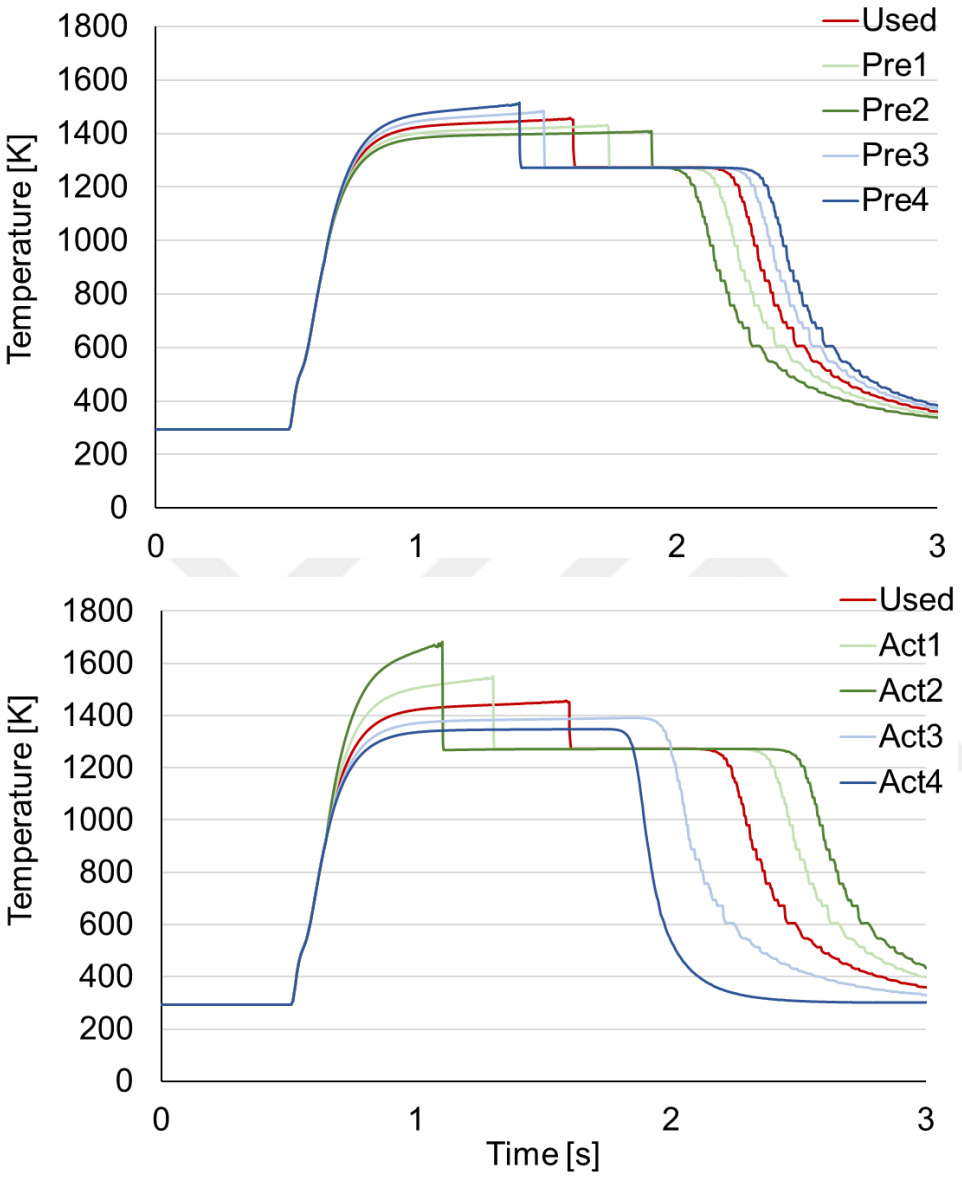

Figure 4.7. Particle temperature profiles obtained with different intrinsic combustion inputs of CFD analysis for Rhenish lignite: (Above) Constant activation energy, (Below) Constant pre-exponential factor

4.2. Single Particle Combustion Modelling

The numerical part of the study is done using the PoliMi model, which offers an end-to-end approach, in which simply from the elemental composition of the fuel and imposition of the operating conditions, the final oxidation products are predicted [34]. The PoliMi model offers a semi-empirical approach, that has been validated for a wide range of coals and operating conditions, with the advantage of no interface for model change, as all the sub-mechanisms are compatible and interconnected [111].

4.2.1. Kinetic Mechanism

In this study, Solid fuel combustion kinetic mechanism which PoliMi model uses is taken from the study done by Tufano et al. [133] (also available in Appendix E). In the light of the TGA experiments, the kinetic parameters are obtained to account for the faster combustion of these coals in the DTF in which the heating rates and temperatures are higher than those in TGA. Compared to pyrolysis, char conversion is not governed only by the chemistry, but also by the intra-particle diffusion of oxygen. Therefore, the oxidation reactions must be escalated to account for the effectiveness factor in these simulations, which is a ratio between the actual rate and the intrinsic rate, and a function of the surrounding temperature. Once accounted for, the rate of decomposition can be reproduced for each set of operating conditions. It becomes clear that TGA experiments are very useful to determine the intrinsic kinetic constants of the decomposition of coals, both in pyrolysis and oxidation conditions. However, one must be aware of the transport phenomena when applying the same tuned model to severe conversion conditions encountered in drop tube furnaces. For high temperature combustion modelling, mass transfer limitations are taking into account using Thiele modulus and effectiveness factor (η) [50,120]. Effectiveness factor is the ratio of actual reaction rate to the intrinsic reaction rate, and a function of Thiele modulus which describes the relation between diffusion and reaction rates of the porous particles. The reaction rates for char oxidation in the PoliMi model are

corrected by multiplication of pre-exponential factors with effectiveness factors calculation of which [80,134,135] is available in Appendix A.

Table 4.5 gives the mass transfer Biot number, Thiele modulus and effectiveness factor calculated for the fuels used in this study. For large mass transfer Biot numbers (Bi_m>30), surface diffusion rate is lower than the external mass transfer rate, so the surface diffusion controls the adsorption rate [136]. Additionally, an effectiveness factor above 0.2 is attributed to pore diffusion limited heterogeneous reaction regime (zone II in Figure 2.5) [137–139]. Thus, according to Table 4.5, DTF experiments at 1000ºC provides mixed char combustion conditions in which diffusion and surface reaction rates are of same order.

The calculated effectiveness factors for a particle size of 110μm and combustion temperature of 1000 ºC (see Table 4.5) are in agreement with the effectiveness factor calculated in the several studies on coal combustion in DTF [50,53,120]

Table 4.5. Characteristic non-dimensional numbers related to the external and internal mass transfer process in DTF experiments for the fuels under study: Rhenish lignite (RL), Soma lignite (SL), Afşin-Elbistan lignite(AEL), Tunçbilek lignite (TL)

	Biot number (Bi_m)	Thiele modulus (φ)	Effectiveness factor (η)
RL	600.04	10.27	0.26
SL	600.04	9.76	0.27
AEL	600.04	9.25	0.29
TL	600.04	9.76	0.27

4.2.2. Fuel Characterization

Characterization of the samples follows the procedure described in Sommariva et al. [109]. The samples SL and RL are directly within the characterization boundaries for coal combustion in PoliMi model (see Figure 4.8). However, AEL and TL cannot

be characterized by a feasible mixture of the reference coal components because of their high hydrogen and oxygen contents. In order to characterize AEL and TL, biomass components, described in reference [140], are used as a reference species along with reference coal species [109]; COAL1, COAL2, COAL3 and CHARC. COAL3 and COAL1 describes a lignite with high oxygen content and a bituminous coal with high hydrogen content, respectively whereas CHARC designates pure carbon. COAL2 which has similar composition with bituminous coal is selected in the middle of the triangle of COAL1, COAL3 and CHARC. As seen in Figure 4.8, the characterization of AEL and TL is possible using linear interpolation of coal and biomass reference species together. According to the Van Krevelen diagram (see Figure 3.3), the elemental composition of AEL fits the definition of peat and biomass, and cellulose (CELL) is selected as a biomass-based reference species in order to fit AEL into the model. For characterization of TL, there are two suitable biomass components: Trilinolein (TGL) and lignin with major element of hydrogen (LIGH). Since TGL represents the group of extractives, and suggested to be used for characterization of algae [141], LIGH is preferred for characterization of TL. Table 4.4 presents the distribution of reference species of 4 lignites.

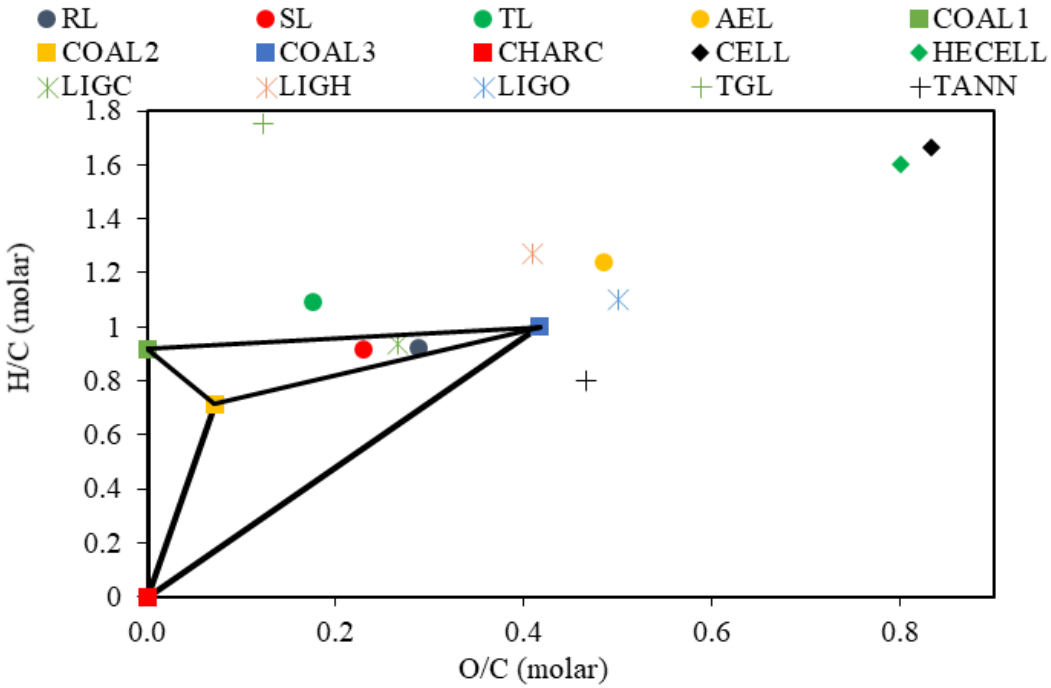

Figure 4.8. Composition of reference species and the lignites studied; RL: Rhenish lignite, SL: Soma lignite, TL: Turkish lignite, AEL: Afşin-Elbistan lignite, COAL1/2/3: Reference coal species, CHARC: Pure carbon, CELL: Cellulose, HECELL: Hemicellulose, LIGC/H/O: Reference lignin species, TGL: Trilinolein, TANN: Tannin

Table 4.6. Reference species distribution of sample coals: Rhenish lignite (RL), Soma lignite (SL), Tunçbilek lignite (TL), Afşin-Elbistan lignite (AEL)

Reference species, %	RL	SL	TL	AEL
MOIST	5.4	2.0	2.0	4.6
COAL1	9.3	16.5	47.9	11.7
COAL2	15.3	16.2	0.0	0.0
COAL3	67.2	49.9	0.0	21.2
CELL	0.0	0.0	0.0	20.1
LIGH	0.0	0.0	36.1	0.0
ASH	2.9	15.5	14.0	42.4

4.2.3. Sensitivity Analysis

Sensitivity analysis of the Polimi model is done comparing percent mass loss profiles obtained with different particle temperature profiles. Two parameters are chosen to make variety in the profiles: heating rate and peak temperature. In order to

see the effect of these parameters, different particle temperature profiles are created based on the profile obtained from CFD analysis. This reference profile is named as 'Used' in the following figures.

Figure 4.9 shows the profiles used to see the heating rate effects. These profiles are created using double and half of the heating rate of the reference profile with same peak temperature as the reference profile. PoliMi model predictions obtained using the profiles in Figure 4.9 are plotted in Figure 4.10. The results show that as heating rate increases, the conversion starts earlier. Moreover, the conversion rate decreases with the heating rate.

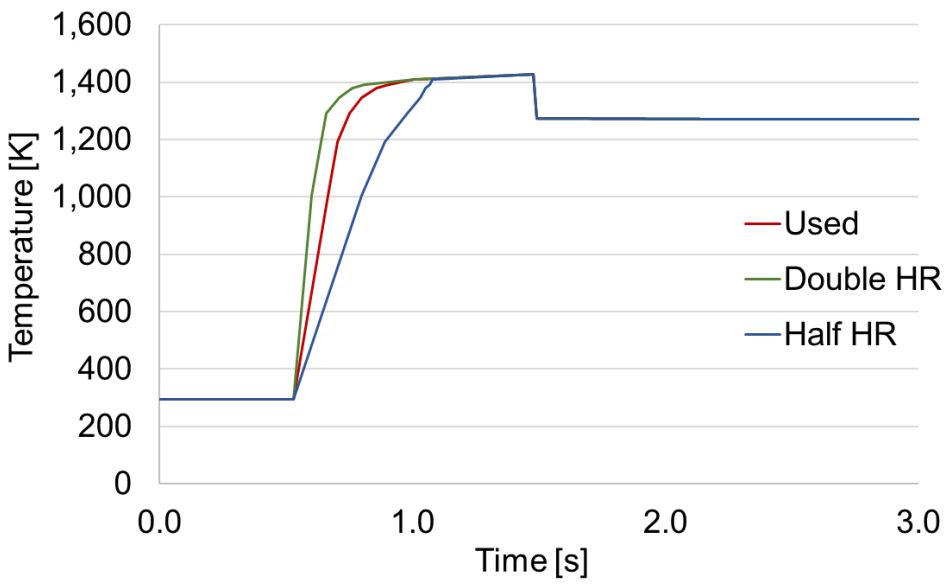

Figure 4.9. Particle temperature profiles used for sensitivity analysis: Used (for the results), Double heating rate (HR) and Half heating rate (HR)

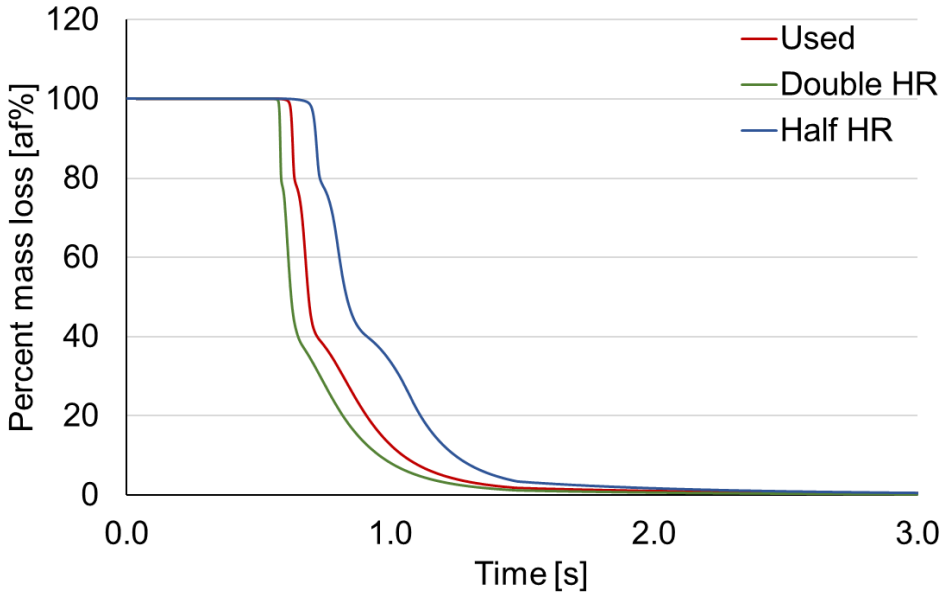

Figure 4.10. Polimi model predictions based on the particle temperature profiles used for sensitivity analysis: Used (for the results), Double heating rate (HR) and Half heating rate (HR)

Peak temperature effect on the model predictions is investigated using the particle temperature profiles in figure 4.11. The heating rate is kept constant to isolate peak temperature as only parameter. The peak temperatures in figure 4.11 are 1300, 1400, 1500, 1600, 1700 and 1800K. Model predictions are shown in Figure 4.12. Since pyrolysis ends before the particle temperature reaches 1300K, there is no peak temperature effect observed on the pyrolysis step. In the char oxidation, conversion rate increases with temperature, as expected. Also, the conversion profiles are not changing much for the peak temperatures above 1600K.

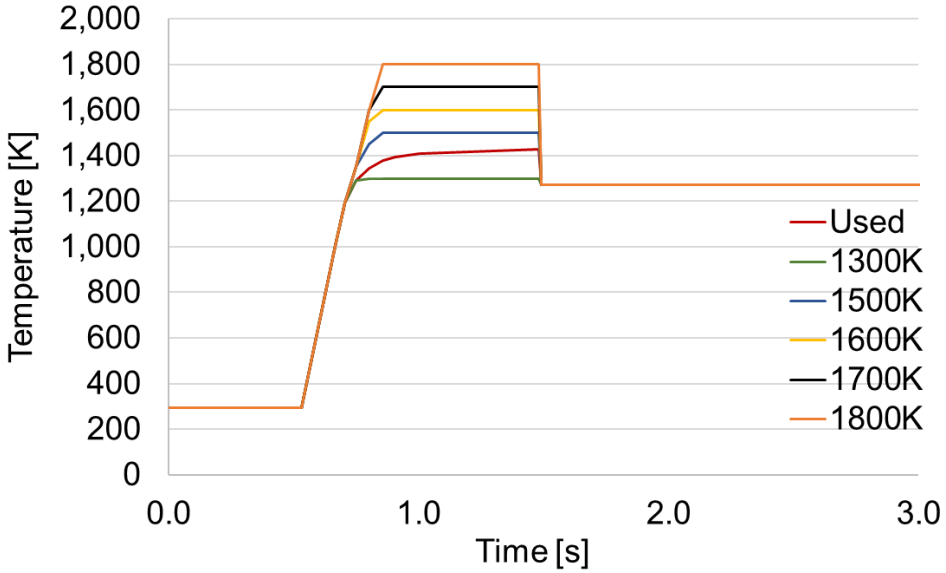

Figure 4.11. Particle temperature profiles used for sensitivity analysis: Used (for the results), peak temperature of 1300K, 1500K, 1600K, 1700K and 1800K

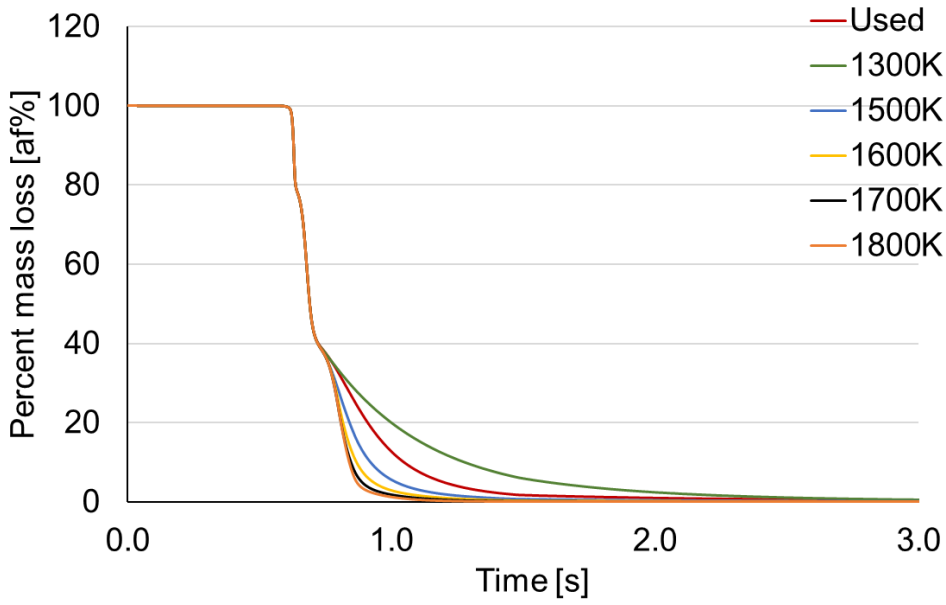

Figure 4.12. Polimi model predictions based on the particle temperature profiles used for sensitivity analysis: Used (for the results), peak temperatures of 1300K, 1500K, 1600K, 1700K and 1800K

CHAPTER 5

RESULTS AND DISCUSSION

5.1. Experimental Results on Combustion Behavior

Experimental part of this study includes combustion experiments in TGA and DTF. The ash free mass loss profiles of studied fuels in TGA are compared as done by Özer et al. [142] before. Additionally, raw TGA experimental data are used to calculate the characteristic temperatures for further discussion. High temperature combustion rates of each studied fuel are obtained using global one-step reaction model on DTF experimental data.

5.1.1. TGA Experiments

The low-temperature combustion behavior of the samples is studied using analysis of the thermogravimetry (TG) and differentiated thermogravimetry (DTG). Figure 5.1 displays the ash-free mass loss and differentiated (rate of) ash-free mass loss with respect to time for four sample fuels and four heating rates. Up to 200ºC, the mass loss due to evaporation of moisture is observed for all fuel samples. The magnitude of the mass loss is found similar to the moisture content presented in the proximate analysis of each fuel (see Table 3.1). Oxygen adsorption after the evaporation is observed only for TL, as seen in the study on a different batch of TL [5,88]. Devolatilization and char oxidation phases take place between 300-700 ºC with different reaction rates based on sample fuel's compositions. Decomposition of calcium carbonate ($CaCO_3$) occurs only for AEL as expected because of its high calcium content.

According to Figure 5.1, Soma lignite (SL) and Tunçbilek lignite (TL) have one phase combustion process, i.e. simultaneous devolatilization and char oxidation. On the other hand, Rhenish lignite (RL) and Afşin-Elbistan lignite (AEL) burn with

more than one distinguishable phase. While RL has two DTG peaks that occur at around 380 ºC and 525ºC, AEL has three at around 405 ºC, 650 and 720 ºC. According to the ash-free proximate analysis (see Table 3.1), RL and AEL have fixed carbon of 45.1 and 31.4%, respectively. Since after their first DTG peaks, RL and AEL remainder weight is only 7.9 and 16.8% of their ash-free portions, respectively, some of the fixed carbon in these fuels also burn in the devolatilization phase.

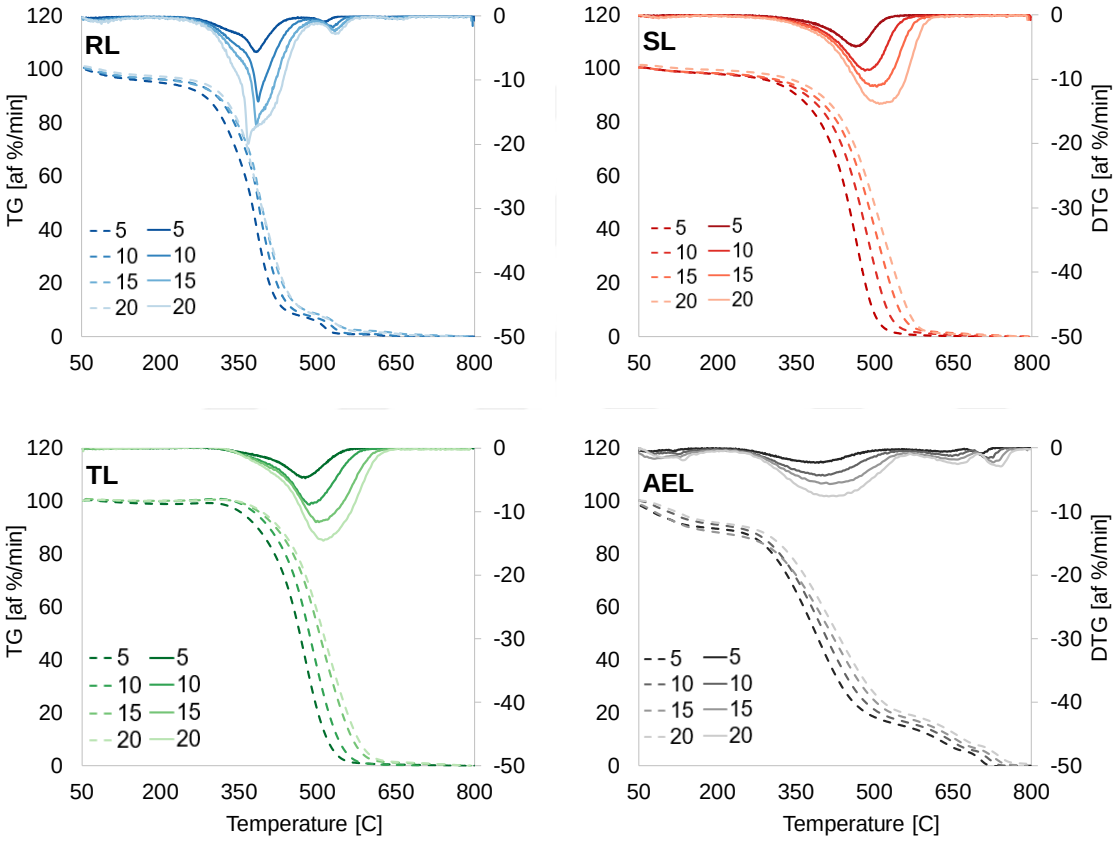

Figure 5.1. TG (dashed lines) and DTG (solid lines) as a function of temperature for the individual chars: Soma lignite (SL), Rhenish lignite (RL), Tunçbilek lignite (TL), Afşin-Elbistan lignite (AEL) for four different heating rates: 5, 10, 15, 20 C/min

Figure 5.1 also shows that the combustion profiles of the fuels change with the heating rate during TGA experiments. DTG graphs are shifted to higher temperatures as the heating rate increases, except for RL. Moreover, the DTG peaks of Turkish

lignites (SL, TL, AEL) remain at the same temperature with an increase in the heating rate. On the contrary, the positions of devolatilization peaks of German lignite (RL) remain the same at 5, 10 and 15 ºC/min, and shift to lower temperatures at 20 ºC/min. Also, the devolatilization peak of RL changes its profile as the heating rate increases. The curvature of the DTG peaks vary depending on compositions. Sharp DTG peaks are attributed to high volatile content available mostly in biomass [5,6,83,143]. German lignite (RL) differs from Turkish lignites (SL, TL, AEL) as having the highest volatile content (47.9%). Accordingly, combustion of German lignite shows a sharp DTG peak even in the experiments with the lowest heating rate (5 ºC/min) but smooth peaks are observed for all Turkish lignites.

The characteristic temperatures and the stages of all TGA experiments (Figure 5.1) are measured and illustrated in Figure 5.2. Appendix D contains the numerical values of characteristic temperature and stages. For RL and AEL, which have more than one peak in their DTG graphs, only the first peak temperatures (T_P) are plotted.

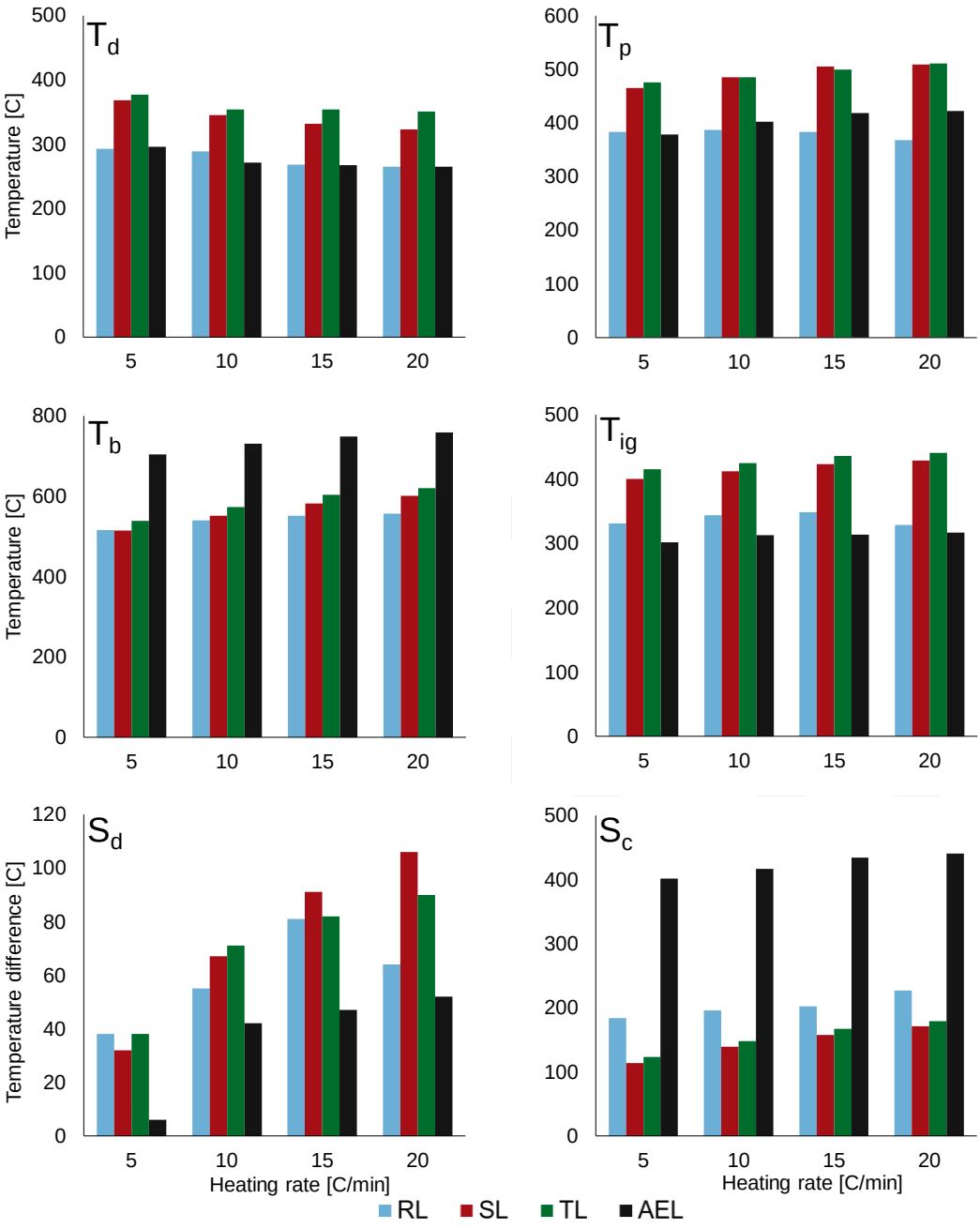

Figure 5.2. Combustion characteristic temperatures and stages of each fuel for different heating rates in TGA experiments: Decomposition temperature (Td), ignition temperature (Tig), peak temperature (Tp), burnout temperature (TB), Decomposition Stage (Tig- Td), Combustion Stage (Tb -Tig)

The fuels used in this study can be divided into two groups in terms of the ratio of volatile matter over fixed carbon (VM/FC) which has an effect on the

decomposition onset. Table 3.1 shows the ratio of VM/FC for the lignites used in this study. The lignites with the ratios higher than 1 (RL & AEL) tend to decompose earlier than the others (TL & SL), as seen in other studies [6,65,82,144]. Even SL has a higher ratio of VM/FC than TL, their DTG profiles are almost identical to each other for all heating rates. It can be attributed to the proximity of their origins.

Decomposition stage covers the decomposition of the chemical structure of the solid fuel before the onset of ignition. Both German (RL) and Turkish lignites (TL, SL, AEL) have higher temperature ranges for decompostion stage as temperature increase from 5 to 15 C/min. However, increasing the heating rate from 15 to 20 ^{o}C/min causes a shift to narrower temperature ranges for German lignite (RL) whereas the temperature ranges of Turkish lignites keep increasing. Among the fuels studied, AEL has smallest decomposition stage temperature ranges for all heating rates.

Xu et al. [145] report non-isothermal TGA experiments under air atmosphere for 32 Chinese coals with various volatile contents (dry-ash free basis, 7- 49%). Results show that the three combustion characteristic temperatures (T_{ig}, T_b, T_p) decreases with an increase of volatile content. In the present work, this relation between characteristic temperatures and volatile content is valid for TL, SL and RL. On the other hand, the high dry-ash free volatile content of AEL causes early ignition (lower T_{ig} and T_p) but its T_b is higher than the others due to late-stage $CaCO_3$ decomposition which leads longer combustion stage [5]. It is expected that the temperature range of combustion stages increases with the heating rate for all fuels [4,5].

To assess the influence of the heating rate, the combustion behavior of the sample fuels is compared using DTG graphs in Figure 5.3 which uses the dataset expressed in Figure 5.1. The magnitude of mass-loss rates at T_P are inversely proportional to the ash percentage of fuel. [4,5,82]. AEL (Ash:42.4%) burns with the lowest mass loss rates while the highest rate is observed for RL (Ash: 2.9%). SL and

TL have similar ash contents (TL:14%, SL:15.5%), so the maximum reaction rates are similar to each other for all heating rates.

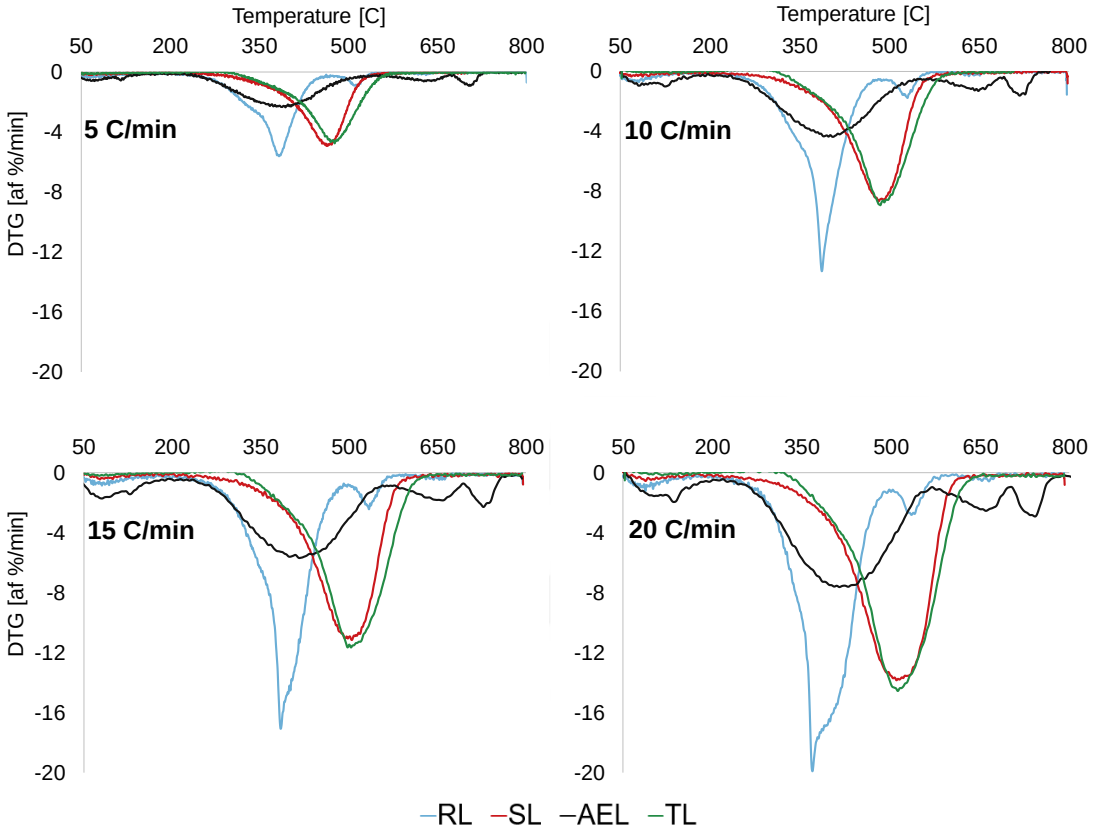

Figure 5.3. DTG [%/min] as a function of temperature for the individual Heating rates: 5, 10, 15, 20 C/min for four coal samples: Soma lignite (SL), Rhenish lignite (RL), Tunçbilek lignite (TL), Afşin-Elbistan lignite (AEL)

Decomposition of $CaCO_3$ is observed for only AEL among the fuel samples studied. In a recent study by Barzegar et al. [4], decomposition of $CaCO_3$ is observed in the combustion of two Turkish lignites with similar CaO contents; Orhaneli lignite (CaO: 22.8%) and Soma lignite (CaO: 19.4%). Higher magnitude of the mass loss due to decomposition of $CaCO_3$ is observed for Soma lignite since Soma lignite has higher ash content than Orhaneli lignite (42.6%, 10.5%, respectively). Magalhaes et al. [5] performs X-ray Diffraction (XRD) analysis on ash samples of Soma lignite which are

prepared at final temperatures of 650ºC and 800 ºC. The results show a lower peak of $CaCO_3$ for a final temperature of 650ºC which indicates the presence of $CaCO_3$ decomposition after 650 ºC. In the present study, X-Ray Fluorescence (XRF) analysis of AEL is done, and shows that calcium has the highest percentage (38.8%) among the other organic components in the ash. Since AEL has very high ash content (42.4%), elemental content of the calcium equals to 16.4% of as-received particle. Third DTG peak of AEL causes 3.7% mass loss of as-received particle which is much lower the total amount of calcium in the particle.

5.1.2. Drop Tube Furnace Experiments

The high temperature (1000ºC) combustion behavior of the sample fuels is investigated using DTF with feeding and collection system. Conversion profiles were obtained changing the position of the collection probe along the center axis of the DTF. The residence times of the fuel particles for each collection probe position are calculated using the particle velocity profiles in DTF provided by CFD analysis. The reaction rate constants for each fuel are obtained using the burnout values of samples collected at different axial levels of the DTF. A global one-step reaction model was used for isothermal char oxidation, as defined in equation (24):

$$\frac{\partial \alpha}{\partial t} = k\,(1-\alpha) \qquad (24)$$

where k is the reaction rate constant, t is time, and α is the burnout given by Eq. (24). Integration of the above equation with the application of the initial condition $\alpha = 0$ at t=0 gives:

$$-\ln\,(1-\alpha) = kt \qquad (25)$$

The first-order rate constants, k, in this study were obtained by linear fitting to the experimental data in plots of $-\ln(1-\alpha)$ vs t (see Figure 5.4). The slopes of the chart represent the combustion rate of each fuel.

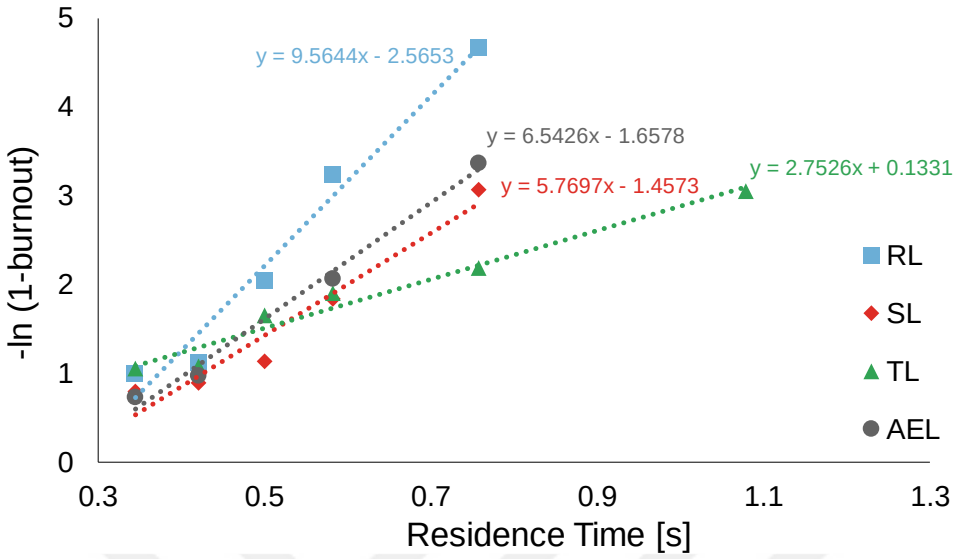

Figure 5.4. DTG [%/min] as a function of residence time: 5, 10, 15, 20 C/min for four coal samples: Soma lignite (SL), Rhenish lignite (RL), Tunçbilek lignite (TL), Afşin-Elbistan lignite (AEL)

The measured residence times for a 90% burnout in DTF are 0.55, 0.6, 0.65, 0.7 sec for RL, AEL, SL and TL, respectively. RL has the highest reactivity (9.6 s-1) among other fuels (AEL: 6.5, SL: 5.8, TL: 2.8 s-1). Unlike low heating rate experiments, TL and SL have distinct combustion rates in the high heating rate DTF experiments. SL burns faster than TL due to excessive fragmentation also observed in the high speed cinematography provided by Magalhaes et al. [19]. There are no available cinematography results for the combustion of RL and AEL. Combustion rates of RL and AEL are also higher than SL which may be an indicator for fragmentation behaviors of RL and AEL. This will be investigated in future studies.

5.2. Numerical Results on Combustion Behavior

5.2.1. CFD Analysis

Figure 5.5 displays the contours of the axial velocity, temperature in DTF without coal injection and 10 particle traces colored by particle temperature for Rhenish lignite simulations. At the tip of the injector, the particles spread away from the central axis along DTF. The diameter of the particle traces are around the inner diameter of the DTF at the particle temperatures above 1300K.

CFD analysis gives the particle temperatures in the hot zone of the DTF as 1402K, 1324K, 1390K for RL, AEL, SL&TL, respectively (see Figure 5.6). Particle temperature results are comparable with the result of the study done by Gilot et al. [50]. Giot et al. [50] measured the particle temperature of the coal char with mean particle size of 130 μm during combustion tests in DTF. According to results [50], particle temperatures were 1244, 1330 and 1417 ºC under wall temperatures of 1100, 1200 and 1300 ºC, respectively.

Magalhaes et al. [19] reported the particle temperatures of TL and SL as 1800 and 1900 K during free-falling combustion experiments in DTF at 1400 K. Due to differences in the experimental conditions, the temperature difference between the ambient air and the particle is high for [19] (400-500 K) compared to the present study (50-150K). Moreover, burnout times of the fuels are measured below 200 ms. Burnout times in the present study (650-700ms) are much higher than the values in the study done by Magalhaes et al. [19]. The differences in both burnout times and particle temperatures are attributed to the differences in the experimental conditions: Higher furnace temperature and lower convective heat transfer of quiescent gas flow conditions in [19].

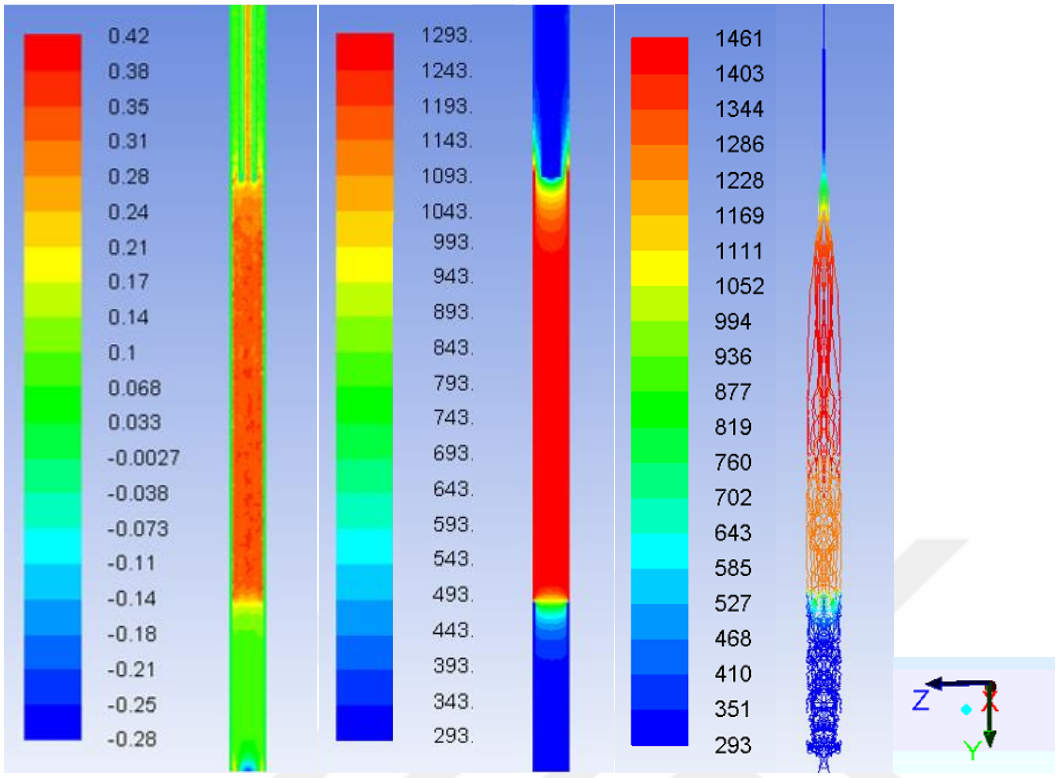

Figure 5.5. CFD simulation results: (Left) contour of axial velocity [m/s], (Middle) temperature [K], (Right) particle traces colored by particle temperature [K]

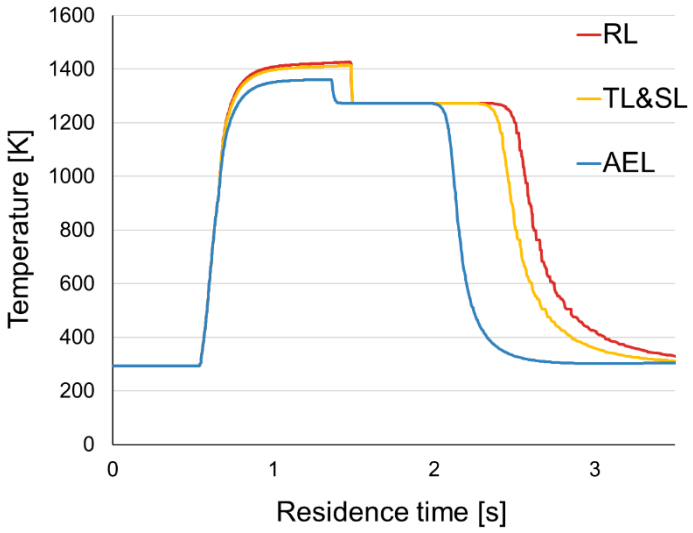

Figure 5.6. Results of the CFD simulation: Particle temperature profiles for each fuel

5.2.2. **PoliMi Model Analysis**

A multi-step PoliMi model is developed and tuned using intrinsic kinetic parameters obtained from non-isothermal air combustion TGA experiments. Accurate estimation of the volatile yield in devolatilization modelling is necessary to obtain reliable numerical results from the combustion of the resultant char. Low and high heating rate pyrolysis simulations are done to understand how accurate the PoliMi model can predict the volatile yields of each fuel. Figure 5.7 compares the experimental and numerical dry-ash free volatile yields for each fuel. It illustrates the low-temperature volatile yields based on proximate analysis and the PoliMi model estimations for the low and high-temperature volatile yields. For low-temperature volatile yield, numerical and experimental results have a good match for SL, AEL and RL with errors of 1.2, 3.1, 4.5%, respectively. The highest error is obtained for TL (29.0%) which can be attributed to the high content of biomass component (LIGH) in TL (see Table 5.7).

The ratio of high over low-temperature volatile contents is calculated using PoliMi model results. The fuels can be divided into two groups based on their ratios: 1.16 for TL and AEL, and 1.31 for SL and RL. This difference may be the outcomes of the non-traditional characterization method used for both TL and AEL (explained in section 4.2).

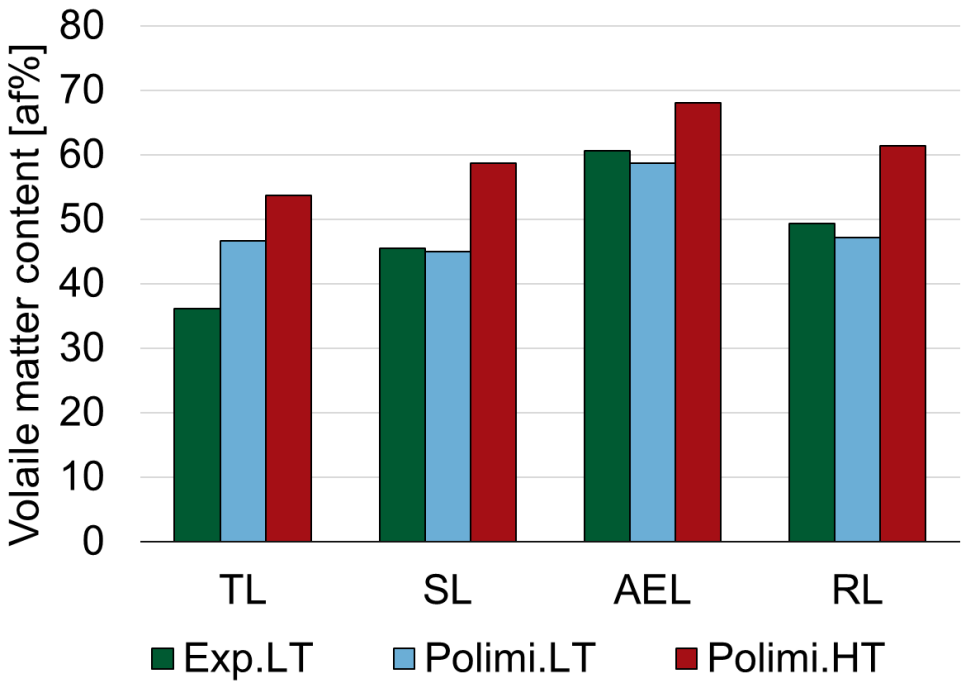

Figure 5.7. Volatile contents measured experimentally (TGA) and calculated numerically (PoliMi model) for all studied fuels; LT: Low Temperature, HT: High Temperature

High temperature (1000ºC) pyrolysis experiments under N_2 ambient are done using DTF to validate the high-temperature volatile contents estimation of PoliMi model. Only RL and SL are used in pyrolysis experiments due to their suitability for validated PoliMi model characterization [109]. According to CFD analysis, DTF provides residence times of 2 seconds in the hot zone to the particle fed into it. Alhought It is assumed that all volatile contents the fuels have released at the end of the hot zone of the DTF. Numerical and experimental results are shown in Table 5.1. It is expected that the high temperature volatile yield (HTVL) is higher than the low-temperature volatile content (proximate analysis). The modelling error is higher in high-temperature pyrolysis for both fuels. PoliMi model overpredicts HTVL of SL with 5.1% error, and under predicts HTVL of RL with 6.4% error.

Table 5.1. Volatile contents [af%] measured experimentally (TGA for low temperature and DTF for high temperature) and calculated numerically (PoliMI model)

	Low Temperature			High Temperature		
	Experimental	PoliMi	Error [%]	Experimental	PoliMi	Error [%]
Soma Lignite (SL)	45.4	44.9	1.2	55.8	58.6	5.1
Rhenish Lignite (RL)	49.3	47.1	4.5	65.7	61.4	6.4

In order to model solid fuel combustion in DTF, particle temperature profiles given in Figure 5.6 are used as an input to PoliMi model. Figure 5.8 compares the experimentally obtained burnout values with model predictions for studied fuels. According to model predictions, devolatilization occurs between residence time of ~0.08 and ~0.19 sec. After the devolatilization, char oxidation starts with a lower conversion rate than the devolatilization. Overall, char oxidation rates seem to be in agreement with the experimental results but the onset times of the oxidation are not well predicted which is attributed to the excessive devolatilization rates.

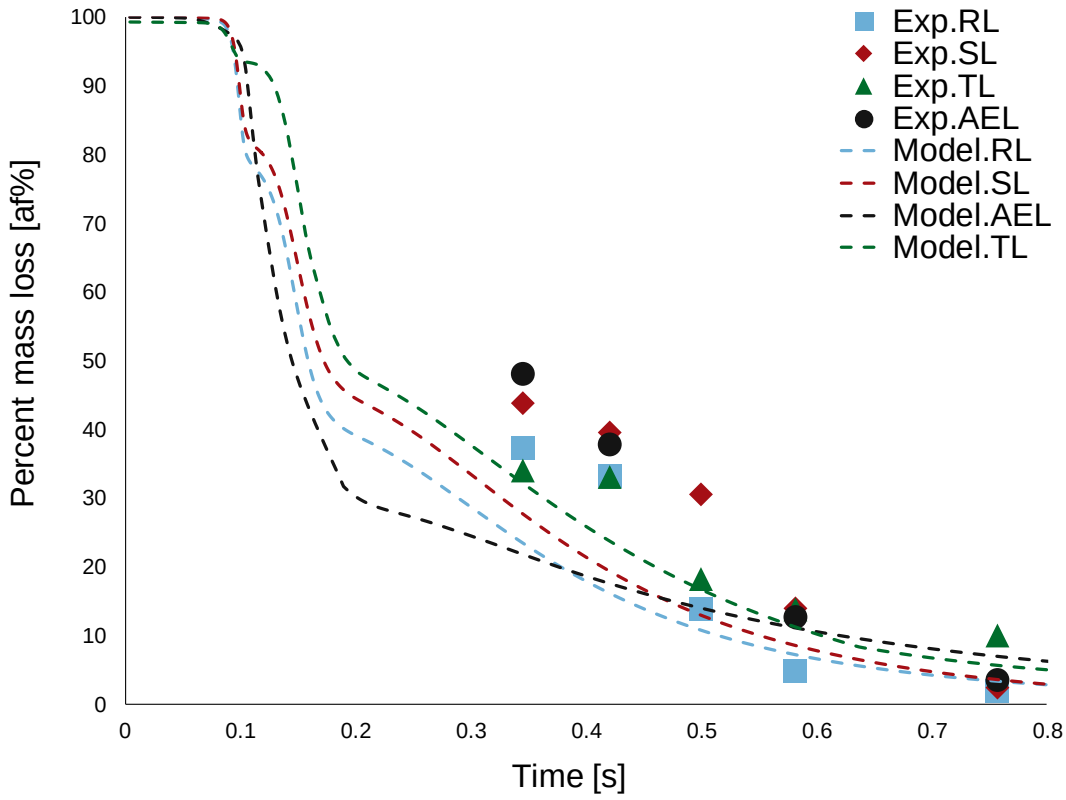

Figure 5.8. Comparison between PoliMi model predictions and experimental data: TG [ash free%] of sample lignites as a function of temperature in DTF experiments: Soma lignite (SL), Rhenish lignite (RL), Tunçbilek lignite (TL), Afşin-Elbistan lignite (AEL)

Figure 5.9, which uses dataset expressed in Figure 5.8, shows the experimental results with model predictions only for the fuels whose elemental compositions are suitable for coal characterization of PoliMi model (see Figure 4.4). As mentioned above, devolatilization rates are overpredicted. With around 0.1 sec shift, model predictions can match quite well with the experimental results for both fuels. According to HTVL magnitudes in Table 5.1, devolatilization of both fuels ends between the residence times of 0.34 and 0.42 sec. Since the conversion rates increase after the experimental data points at 0.42 sec, it is assumed that the char oxidation of both fuels starts at around 0.42 s. Experimental char oxidation rates first increase (0.42-0.58 sec) then decrease (0.58-0.76 sec) but the predicted rates continuously decrease.

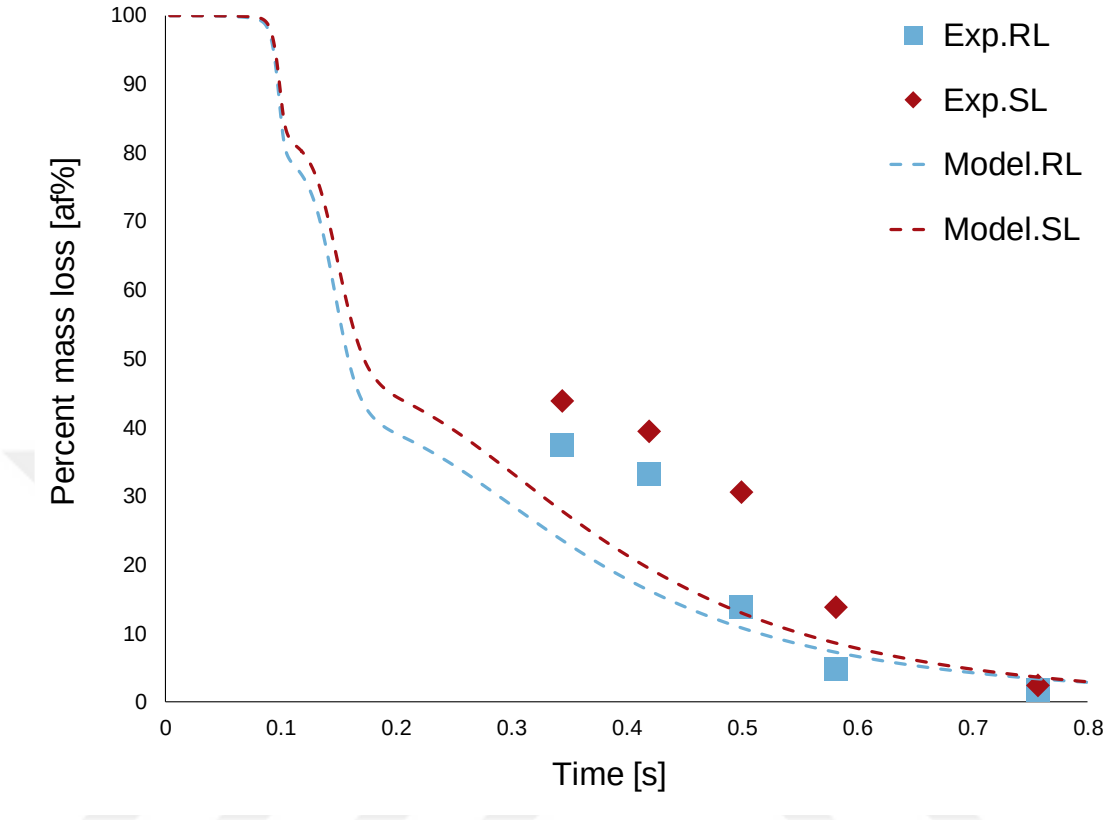

Figure 5.9. Comparison between PoliMi model predictions and experimental data: TG [ash free%] of sample lignites as a function of temperature in DTF experiments: Soma lignite (SL), Rhenish lignite (RL)

Uncertainty analysis of the experimentally obtained burnout values is done only for Rhenish lignite (see Appendix D). Table 3.2 displays the uncertainties in time for residence time and in percentage for burnout at different collection probe levels in DTF experiments.

Before the DTF experiments, the collection probe is fastened manually at the desired height level in order to collect fuel samples. The error coming from this positioning process is taken account in the uncertainty analysis of the residence time. On the other hand, statistical uncertainty and systematic uncertainty are combined in the uncertainty analysis of burnout values. Standard deviation is calculated using the

burnout results for each probe height level. Based on the standard deviation, statistical uncertainty is calculated. In the calculation of burnout, only mass of the particles are used. Thus, mass measurement apparatus is taken as only uncertainty source for systematic uncertainty.

Table 5.2. Uncertainties of the calculated residence times and burnout values at different residence times in DTF combustion experiments for Rhenish lignite

Probe height level [m]	Residence time, t, [s]	Δt [s]	Δ Burnout [%]
0.50	0.757	0.015	3.45
0.60	0.582	0.009	3.55
0.65	0.499	0.007	2.58
0.70	0.420	0.006	1.13
0.75	0.345	0.004	2.06

Figure 5.10 uses the same dataset used in figure 5.8 to express the experimental results with error bars based on the Table 5.2. According to the figure 5.10, uncertainties in the residence times are lower than the uncertainties in the burnout calculation. Especially for higher burnout values, the errors are significantly high which is attribute to low w_a and w_b values in the burnout calculation (see Equation 21).

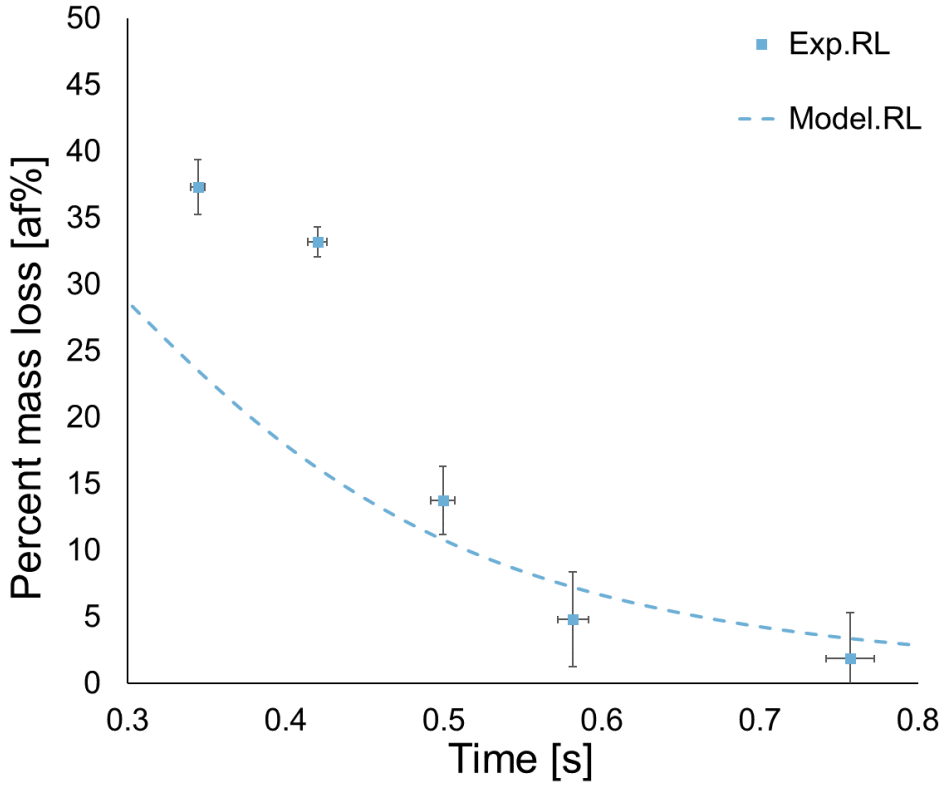

Figure 5.10. Comparison between PoliMi model predictions and experimental data with error bars: TG [ash free%] of Rhenish lignite

CHAPTER 6

CONCLUSION AND FUTURE WORKS

6.1. Conclusion

The present study investigates the air combustion behaviour of lignites from different geographic origins using both experimental and numerical methods. Experimental part of the study is carried out using two different experimental rigs: Thermogravimetric analyzer (TGA) with low heating rates (5, 10, 15, 20ºC/min) and Drop tube furnace (DTF) with high heating rate (~10^4 ºC/s). The temperature and velocity profiles of the solid fuel particle durin the DTF combustion experiments are obtained using ANSYS Fluent. Then, these profiles are used as inputs to PoliMi model for the simulation of single particle combustion. The main outcomes of this study are as follows:

- For low heating rate combustion conditions (TGA), it was observed that the higher volatile content causes early ignition, peak and burnout temperatures (T_{ig}, T_b, T_p). The lignites with the ratio of volatile matter over fixed carbon higher than one ignited earlier and burned with more than one distinguishable phases. When volatile matter content is higher than fixed carbon content, devolatilization step become dominant over char oxidation. Thus, peak temperature (T_b) shifts to the lower temperatures.

- In the low heating rate experiments (TGA), high ash content had a negative effect on the magnitude of mass loss rate while no relevant effect of the ash content was observed in high heating rate experiments (DTF). TGA experiments provide kinetic limited regime in which mass loss rate can be described with reaction rate in Arrhenius form and the char content of the fuel. As the char content increases or ash content decreases, mass loss rate increases. On the other hand, DTF experiments provide pore diffusion limited regime in which mass transfer rate is important for the calculation of mass loss rate. Mass transfer rate highly depends on the morphological properties of the fuel which can cancel the negative effects of the ash content on the combustion rate.

- German lignite presented higher combustion rates than Turkish lignites under both high and low heating rate combustion conditions (DTF and TGA). It is attributed to the German lignite's compositional superiority over Turkish lignites. It has highest volatile matter and lowest ash contents. High volatile content cause early ignition in TGA experiments, and may lead to higher increase in effective surface area during devolatilization in DTF experiments.

- In terms of combustion rates of Turkish lignites, TGA results were not parallel to DTF experiments. This shows that the mass transfer rates of the fuels are not directly proportional to the intrinsic kinetic rates. Evolution of the fuel particle morphology under high temperature needs to be investigated for the further discussion on mass transfer rates.

- In the light of high-temperature volatile yields obtained from the pyrolysis experiments in DTF, onset times of the char oxidation in the combustion experiments were found. Based on the onset times and burnout times, conversion profile could be separable into individual combustion steps as devolatilization and char oxidation.

- In comparison to experimental results, high-temperature volatile yield predictions of PoliMi model were quite accurate with 5.1% and 6.4% error for SL and RL, respectively. The PoliMi model devolatilization reactions are already developed using high number of experimental data by another research group [111]. Since both fuels are suitable for PoliMi model, it is expected to have accurate predictions on high-temperature volatile yield.

- Polimi model overpredicted devolatilization rates of DTF experiments whereas its agreement with the char oxidation experimental results was satisfactory. According to sensitivity analysis on Polimi model, 10% decrease in the heating rate of the particle temperature profile lead an agreement between model predictions and experimental results. Therefore, particle temperature profile needs to be determined experimentally.

- For the fuels whose elemental compositions are not suitable for the coal characterization of PoliMi model, hybrid characterization method was proposed. The comparison with the experimental data showed that predictions of the proposed method were not accurate on guessing volatile matter content. It is attributed to the excessive volatile contents of the biomass reference species used in the hybrid characterization.

6.2. Future Works

This study includes the combination of experimental and numerical works. Thus, the focus of the its future studies is the improve the model with experimental validation. In the light of the conclusions of this study and the available literature in the combustion research area, the possible future studies as a follow up to the present study are listed:

- In this study, it is aimed to obtain the char samples at any moments of conversion process but collection probe used in this study cannot collect samples first 23 cm portion of the hot zone. Using longer collection probe enables the researcher plot the conversion profile starting at the tip of the injector. Conversion profile of the fuel sample starting from zero conversion point and elemental composition of collected samples can be used to tune the kinetic mechanism of PoliMi model.

- Evolution of the fuel morphology during the combustion needs to be investigated. Under high heating rate and high temperature conditions, fragmentation and swelling occurs. However, in the modelling part of the study, it is assumed that the particle size keeps constant during the conversion due to lack of experimental data on the morphology.

- Oxy- fuel combustion of pulverized coal, one of the popular methods in carbon capture and storage technology (CCS), cause a reduction in the volume of flue gas and an increase in the concentration of carbon dioxide (CO_2) in the flue gas. Reliability of the experimental and modelling methods used in the present study are validated with the literature. With some arrangement in the gas feeding system, drop tube furnace can be used to investigate the oxy-fuel combustion rate of various solid fuels. PoliMi model simulate coal combustion using gasification and oxidation reactions. Oxy-fuel combustion experimental data will be useful to calibrate the ambient CO_2 sensitivity of the kinetic mechanism of PoliMi model.

REFERENCES

[1] Energy Information Administration. International Energy Outlook. Outlook 2019;0484:70–99. doi:https://www.eia.gov/outlooks/ieo/pdf/ieo2019.pdf.

[2] Kömür Arama Araştırmaları n.d. http://www.mta.gov.tr.

[3] Turkish Republic Ministry of Energy and Natural Resources. Strategic Energy Plan 2015-2019 2015:128. doi:10.1002/ejoc.201200111.

[4] Barzegar R, Yozgatligil A, Atimtay AT. Combustion characteristics of Turkish lignites at oxygen-enriched and oxy-fuel combustion conditions. J Energy Inst 2018. doi:10.1016/j.joei.2018.08.007.

[5] Magalhães D, Kazanç F, Riaza J, Erensoy S, Kabaklı Ö, Chalmers H. Combustion of Turkish lignites and olive residue: Experiments and kinetic modelling. Fuel 2017;203:868–76. doi:10.1016/j.fuel.2017.05.050.

[6] Yuzbasi NS, Selçuk N. Air and oxy-fuel combustion characteristics of biomass/lignite blends in TGA-FTIR. Fuel Process Technol 2011;92:1101–8. doi:10.1016/j.fuproc.2011.01.005.

[7] Küçükbayrak S, Haykiri-Açma H, Ersoy-Meriçboyu A, Yaman S. Effect of lignite properties on reactivity of lignite. Energy Convers Manag 2001;42:613–26. doi:10.1016/S0196-8904(00)00073-X.

[8] Abbasi-Atibeh E, Yozgatligil A. A study on the effects of catalysts on pyrolysis and combustion characteristics of Turkish lignite in oxy-fuel conditions. Fuel 2014;115:841–9. doi:10.1016/j.fuel.2013.01.073.

[9] Tomeczek J. Coal Combustion. United States: 1992.

[10] Fletcher, Thomas H. and Kerstein AR, Pugmire, Ronald J. and Grant DM. A Chemical Percolation Model for Devolatilization: Summary. J Chem Inf Model 2013;53:1689–99. doi:10.1017/CBO9781107415324.004.

[11] Pugmire RJ, Solum MS, Grant DM, Critchfield S, Fletcher TH. Structural evolution of matched tar-char pairs in rapid pyrolysis experiments. Fuel 1991;70:414–23. doi:10.1016/0016-2361(91)90132-T.

[12] Alvarez YE, Moreno BM, Klein MT, Watson JK, Castro-Marcano F, Mathews JP. Novel simplification approach for large-scale structural models of coal: Three-dimensional molecules to two-dimensional lattices. Part 3: Reactive lattice simulations. Energy and Fuels 2013;27:2915–22. doi:10.1021/ef4001105.

[13] Neavel RC. Coal Structure and Coal Science: Overview and

Recommendations. ACS Div Fuel Chem Prepr 1979;24 v 1:73–82.

[14] Macerals n.d. https://www.uky.edu/KGS/coal/coal-macerals.php.

[15] Rubio B, Mayoral MC, Izquierdo MT, Andre JM. Different approaches to proximate analysis by thermogravimetry analysis. Thermochim Acta 2001;370:91–7.

[16] Van Krevelen DW, Schuyler J. Coal Science: Aspects of Coal Constitution. 1957.

[17] American Society for Testing and Materials (ASTM). Standard Classification of Coals by Rank. Gaseous Fuels; Coal Coke; Bio-Energy Ind Chem from Biomass; Catal 1998;05.06.

[18] Levendis YA, Joshi K, Khatami R, Sarofim AF. Combustion behavior in air of single particles from three different coal ranks and from sugarcane bagasse. Combust Flame 2011;158:452–65. doi:10.1016/j.combustflame.2010.09.007.

[19] Magalhães D, Panahi A, Kazanç F, Levendis YA. Comparison of single particle combustion behaviours of raw and torrefied biomass with Turkish lignites. Fuel 2019;241:1085–94. doi:10.1016/j.fuel.2018.12.124.

[20] Saito M, Sadakata M, Sakai T. Measurements of Surface Combustion Rate of Single Coal Particles in Laminar Flow Furnace. Combust Sci Technol 1987;51:109–28. doi:10.1080/00102208708960319.

[21] Toporov DD. Theoretical Aspects of Burning Pulverised Fuel in Atmosphere. Combust Pulverised Coal a Mix Oxyg Recycl Flue Gas 2014:25–50. doi:10.1016/b978-0-08-099998-2.00003-5.

[22] Debiagi P, Gentile G, Cuoci A, Frassoldati A, Ranzi E, Faravelli T. A predictive model of biochar formation and characterization. J Anal Appl Pyrolysis 2018;134:326–35. doi:10.1016/j.jaap.2018.06.022.

[23] Safdari MS, Amini E, Weise DR, Fletcher TH. Heating rate and temperature effects on pyrolysis products from live wildland fuels. Fuel 2019;242:295–304. doi:10.1016/j.fuel.2019.01.040.

[24] Wang B, Xu F, Zong P, Zhang J, Tian Y, Qiao Y. Effects of heating rate on fast pyrolysis behavior and product distribution of Jerusalem artichoke stalk by using TG-FTIR and Py-GC/MS. Renew Energy 2019;132:486–96. doi:10.1016/j.renene.2018.08.021.

[25] Howard JB, Essenhigh RH. Pyrolysis of Coal Particles in Pulverized Fuel Flames. Ind Eng Chem Process Des Dev 1967;6:74–84. doi:10.1021/i260021a013.

[26] Smith KL, Smoot LD, Fletcher TH, Pugmire RJ. The structure and reaction processes of coal. 1994.

[27] Essenhigh RH. Fundamentals of coal combustion. 2nd suppl. New York: Wiley; 1981.

[28] Serio MA, Hamblen DG, Markham JR, Solomon PR. Kinetics of Volatile Product Evolution in Coal Pyrolysis: Experiment and Theory. Energy and Fuels 1987;1:138–52. doi:10.1021/ef00002a002.

[29] Wang G, Zander R, Costa M. Oxy-fuel combustion characteristics of pulverized-coal in a drop tube furnace. Fuel 2014;115:452–60. doi:10.1016/j.fuel.2013.07.063.

[30] Zhang S, Jiang X, Lv G, Wu L, Li W, Wang Y, et al. Co-combustion of Shenmu coal and pickling sludge in a pilot scale drop-tube furnace: Pollutants emissions in flue gas and fly ash. Fuel Process Technol 2019;184:57–64. doi:10.1016/j.fuproc.2018.11.009.

[31] Artos V, Scaroni AW. T.g.a. and drop-tube reactor studies of the combustion of coal blends. Fuel 1993;72:927–33. doi:10.1016/0016-2361(93)90289-E.

[32] Khatami R, Stivers C, Levendis YA. Ignition characteristics of single coal particles from three different ranks in O 2/N 2 and O 2/CO 2 atmospheres. Combust Flame 2012;159:3554–68. doi:10.1016/j.combustflame.2012.06.019.

[33] Chi T, Zhang H, Yan Y, Zhou H, Zheng H. Investigations into the ignition behaviors of pulverized coals and coal blends in a drop tube furnace using flame monitoring techniques. Fuel 2010;89:743–51. doi:10.1016/j.fuel.2009.06.010.

[34] Maffei T, Khatami R, Pierucci S, Faravelli T, Ranzi E, Levendis YA. Experimental and modeling study of single coal particle combustion in O2/N2 and Oxy-fuel (O2/CO2) atmospheres. Combust Flame 2013;160:2559–72. doi:10.1016/j.combustflame.2013.06.002.

[35] Authier O, Thunin E, Plion P, Schönnenbeck C, Leyssens G, Brilhac JF, et al. Kinetic study of pulverized coal devolatilization for boiler CFD modeling. Fuel 2014;122:254–60. doi:10.1016/j.fuel.2014.01.026.

[36] Lewtak R, Hercog J. Coal char kinetics of oxidation and gasification reactions. Chem Process Eng - Inz Chem i Proces 2017;38:135–45. doi:10.1515/cpe-2017-0011.

[37] Botelho T, Costa M, Wilk M, Magdziarz A. Evaluation of the combustion characteristics of raw and torrefied grape pomace in a thermogravimetric analyzer and in a drop tube furnace. Fuel 2018;212:95–100. doi:10.1016/j.fuel.2017.09.118.

[38] Pereira S, Martins PCR, Costa M. Kinetics of Poplar Short Rotation Coppice Obtained from Thermogravimetric and Drop Tube Furnace Experiments. Energy and Fuels 2016;30:6525–36. doi:10.1021/acs.energyfuels.6b01313.

[39] Heuer S, Senneca O, Wütscher A, Düdder H, Schiemann M, Muhler M, et al. Effects of oxy-fuel conditions on the products of pyrolysis in a drop tube reactor. Fuel Process Technol 2016;150:41–9. doi:10.1016/j.fuproc.2016.04.034.

[40] Riaza J, Khatami R, Levendis YA, Álvarez L, Gil M V., Pevida C, et al. Combustion of single biomass particles in air and in oxy-fuel conditions. Biomass and Bioenergy 2014;64:162–74. doi:10.1016/j.biombioe.2014.03.018.

[41] Simone M, Biagini E, Galletti C, Tognotti L. Evaluation of global biomass devolatilization kinetics in a drop tube reactor with CFD aided experiments. Fuel 2009;88:1818–27. doi:10.1016/j.fuel.2009.04.032.

[42] Guizani C, Valin S, Billaud J, Peyrot M, Salvador S. Biomass fast pyrolysis in a drop tube reactor for bio oil production: Experiments and modeling. Fuel 2017;207:71–84. doi:10.1016/j.fuel.2017.06.068.

[43] Pottmaier D, Costa M, Farrow T, Oliveira AAM, Alarcon O, Snape C. Comparison of rice husk and wheat straw: From slow and fast pyrolysis to char combustion. Energy and Fuels 2013;27:7115–25. doi:10.1021/ef401748e.

[44] Kazanc F, Khatami R, Manoel Crnkovic P, Levendis YA. Emissions of NOx and SO2 from coals of various ranks, bagasse, and coal-bagasse blends burning in O2/N2 and O2/CO2 environments. Energy and Fuels 2011;25:2850–61. doi:10.1021/ef200413u.

[45] Zhang S, Jiang X, Lv G, Liu B, Jin Y, Yan J. SO2, NOx, HF, HCl and PCDD/Fs emissions during Co-combustion of bituminous coal and pickling sludge in a drop tube furnace. Fuel 2016;186:91–9. doi:10.1016/j.fuel.2016.08.061.

[46] Zhang S, Lin X, Chen Z, Li X, Jiang X, Yan J. Influence on gaseous pollutants emissions and fly ash characteristics from co-combustion of municipal solid waste and coal by a drop tube furnace. Waste Manag 2018;81:33–40. doi:10.1016/j.wasman.2018.09.048.

[47] Riaza J, Khatami R, Levendis YA, Álvarez L, Gil M V., Pevida C, et al. Single particle ignition and combustion of anthracite, semi-anthracite and bituminous coals in air and simulated oxy-fuel conditions. Combust Flame 2014;161:1096–108. doi:10.1016/j.combustflame.2013.10.004.

[48] Wang G, Silva RB, Azevedo JLT, Martins-Dias S, Costa M. Evaluation of the combustion behaviour and ash characteristics of biomass waste derived fuels, pine and coal in a drop tube furnace. Fuel 2014;117:809–24. doi:10.1016/j.fuel.2013.09.080.

[49] Colom-Díaz JM, Alzueta MU, Fernandes U, Costa M. Emissions of polycyclic aromatic hydrocarbons during biomass combustion in a drop tube furnace. Fuel

2017;207:790–800. doi:10.1016/j.fuel.2017.06.084.

[50] Gilot P, Brillard A, Brilhac JF, Schönnenbeck C. A Simplified Model Accounting for the Combustion of Pulverized Coal Char Particles in a Drop Tube Furnace. Energy and Fuels 2017;31:11391–403. doi:10.1021/acs.energyfuels.7b01756.

[51] Li Q, Zhao C, Chen X, Wu W, Lin B. Properties of char particles obtained under O2/N2 and O2/CO2 combustion environments. Chem Eng Process Process Intensif 2010;49:449–59. doi:10.1016/j.cep.2010.03.007.

[52] Meng F, Yu J, Tahmasebi A, Han Y. Pyrolysis and combustion behavior of coal gangue in O2/CO 2 and O2/N2 mixtures using thermogravimetric analysis and a drop tube furnace. Energy and Fuels 2013;27:2923–32. doi:10.1021/ef400411w.

[53] Dhaneswar SR, Pisupati S V. Oxy-fuel combustion: The effect of coal rank and the role of char-CO 2 reaction. Fuel Process Technol 2012;102:156–65. doi:10.1016/j.fuproc.2012.04.029.

[54] Khatami R, Levendis YA. An overview of coal rank influence on ignition and combustion phenomena at the particle level. Combust Flame 2016;164:22–34. doi:10.1016/j.combustflame.2015.10.031.

[55] Zhang Y, Niu Y, Zou H, Lei Y, Zheng J, Zhuang H, et al. Characteristics of biomass fast pyrolysis in a wire-mesh reactor. Fuel 2017;200:225–35. doi:10.1016/j.fuel.2017.03.070.

[56] Zabaniotou A, Ioannidou O, Antonakou E, Lappas A. Experimental study of pyrolysis for potential energy, hydrogen and carbon material production from lignocellulosic biomass. Int J Hydrogen Energy 2008;33:2433–44. doi:10.1016/j.ijhydene.2008.02.080.

[57] Hoekstra E, Van Swaaij WPM, Kersten SRA, Hogendoorn KJA. Fast pyrolysis in a novel wire-mesh reactor: Decomposition of pine wood and model compounds. Chem Eng J 2012;187:172–84. doi:10.1016/j.cej.2012.01.118.

[58] Di Nola G, de Jong W, Spliethoff H. The fate of main gaseous and nitrogen species during fast heating rate devolatilization of coal and secondary fuels using a heated wire mesh reactor. Fuel Process Technol 2009;90:388–95. doi:10.1016/j.fuproc.2008.10.009.

[59] Riaza J, Ajmi M, Gibbins J, Chalmers H. Ignition and Combustion of Single Particles of Coal and Biomass under O2/CO2 Atmospheres. Energy Procedia 2017;114:6067–73. doi:10.1016/j.egypro.2017.03.1743.

[60] Wang J, Cao Y, Yan Y, Gao J. Heat transfer and kinetics of lignite devolatilization in wire-mesh apparatus. Fuel Process Technol 1994;38:57–67. doi:10.1016/0378-3820(94)90043-4.

[61] Suuberg EM, Peters WA, Howard JB. Product Composition and Kinetics of Lignite Pyrolysis. Ind Eng Chem Process Des Dev 1978;17:37–46. doi:10.1021/i260065a008.

[62] Gibbins-Matham J, Kandiyoti R. Coal Pyrolysis Yields from Fast and Slow Heating in a Wire-Mesh Apparatus with a Gas Sweep. Energy and Fuels 1988;2:505–11. doi:10.1021/ef00010a017.

[63] Riaza J, Mason P, Jones JM, Gibbins J, Chalmers H. High temperature volatile yield and nitrogen partitioning during pyrolysis of coal and biomass fuels. Fuel 2019;248:215–20. doi:10.1016/j.fuel.2019.03.075.

[64] PerkinElmer Inc. A Beginner's Guide: Thermogravimetric Analysis (TGA) TGA 8000 TGA 4000 STA 6000 / STA 8000 2015.

[65] Arenillas A, Rubiera F, Arias B, Pis JJ, Faúndez JM, Gordon AL, et al. A TG/DTA study on the effect of coal blending on ignition behaviour. J Therm Anal Calorim 2004;76:603–14. doi:10.1023/B:JTAN.0000028039.72613.73.

[66] Magalhães D, Kazanç F, Ferreira A, Rabaçal M, Costa M. Ignition behavior of Turkish biomass and lignite fuels at low and high heating rates 2017;207:154–64. doi:10.1016/j.fuel.2017.06.069.

[67] Zhang S, Chen ZD, Chen XJ, Gong XZ. Effects of ash/K2CO3/Fe2O3 on ignition temperature and combustion rate of demineralized anthracite. Ranliao Huaxue Xuebao/Journal Fuel Chem Technol 2014;42:166–74. doi:10.1016/S1872-5813(14)60013-X.

[68] Jones JM, Saddawi A, Dooley B, Mitchell EJS, Werner J, Waldron DJ, et al. Low temperature ignition of biomass. Fuel Process Technol 2015;134:372–7. doi:10.1016/j.fuproc.2015.02.019.

[69] Jayaraman K, Kok MV, Gokalp I. Pyrolysis, combustion and gasification studies of different sized coal particles using TGA-MS. Appl Therm Eng 2017;125:1446–55. doi:10.1016/j.applthermaleng.2017.07.128.

[70] Gou X, Zhao X, Singh S, Qiao D. Tri-pyrolysis: A thermo-kinetic characterisation of polyethylene, cornstalk, and anthracite coal using TGA-FTIR analysis. Fuel 2019;252:393–402. doi:10.1016/j.fuel.2019.03.143.

[71] Soria-Verdugo A, Garcia-Gutierrez LM, Blanco-Cano L, Garcia-Hernando N, Ruiz-Rivas U. Evaluating the accuracy of the Distributed Activation Energy Model for biomass devolatilization curves obtained at high heating rates. Energy Convers Manag 2014;86:1045–9. doi:10.1016/j.enconman.2014.06.074.

[72] Yuzbasi NS, Seluk N. Air and oxy-fuel combustion behaviour of petcoke/lignite blends. Fuel 2012;92:137–44. doi:10.1016/j.fuel.2011.08.026.

[73] Al-Qayim K, Nimmo W, Hughes K, Pourkashanian M. Kinetic parameters of the intrinsic reactivity of woody biomass and coal chars via thermogravimetric analysis. Fuel 2017;210:811–25. doi:10.1016/j.fuel.2017.09.010.

[74] Ma Z, Chen D, Gu J, Bao B, Zhang Q. Determination of pyrolysis characteristics and kinetics of palm kernel shell using TGA-FTIR and model-free integral methods. Energy Convers Manag 2015;89:251–9. doi:10.1016/j.enconman.2014.09.074.

[75] Pielsticker S, Heuer S, Senneca O, Cerciello F, Salatino P, Cortese L, et al. Comparison of pyrolysis test rigs for oxy-fuel conditions. Fuel Process Technol 2017;156:461–72. doi:10.1016/j.fuproc.2016.10.010.

[76] Jones JM, Kubacki M, Kubica K, Ross AB, Williams A. Devolatilisation characteristics of coal and biomass blends. J Anal Appl Pyrolysis 2005;74:502–11. doi:10.1016/j.jaap.2004.11.018.

[77] Jalalabadi T, Li C, Yi H, Lee D. A TGA study of CO2gasification reaction of various types of coal and biomass. J Mech Sci Technol 2016;30:3275–81. doi:10.1007/s12206-016-0636-1.

[78] Xu B, Cao Q, Kuang D, Gasem KAM, Adidharma H, Ding D, et al. Kinetics and mechanism of CO2 gasification of coal catalyzed by Na2CO3, FeCO3 and Na2CO3–FeCO3. J Energy Inst 2019. doi:10.1016/j.joei.2019.08.004.

[79] Wang F, Zeng X, Wang Y, Su H, Yu J, Xu G. Non-isothermal coal char gasification with CO 2 in a micro fluidized bed reaction analyzer and a thermogravimetric analyzer. Fuel 2016;164:403–9. doi:10.1016/j.fuel.2015.09.084.

[80] Senneca O, Vorobiev N, Wütscher A, Cerciello F, Heuer S, Wedler C, et al. Assessment of combustion rates of coal chars for oxy-combustion applications. Fuel 2019;238:173–85. doi:10.1016/j.fuel.2018.10.093.

[81] Gil M V., Riaza J, Álvarez L, Pevida C, Pis JJ, Rubiera F. Oxy-fuel combustion kinetics and morphology of coal chars obtained in N2 and CO2 atmospheres in an entrained flow reactor. Appl Energy 2012;91:67–74. doi:10.1016/j.apenergy.2011.09.017.

[82] Muthuraman M, Namioka T, Yoshikawa K. Characteristics of co-combustion and kinetic study on hydrothermally treated municipal solid waste with different rank coals: A thermogravimetric analysis. Appl Energy 2010;87:141–8. doi:10.1016/j.apenergy.2009.08.004.

[83] Barzegar R, Yozgatligil A, Olgun H, Atimtay AT. TGA and kinetic study of different torrefaction conditions of wood biomass under air and oxy-fuel combustion atmospheres. J Energy Inst 2019. doi:10.1016/j.joei.2019.08.001.

[84] Jones JM, Bridgeman TG, Darvell LI, Gudka B, Saddawi A, Williams A.

Combustion properties of torrefied willow compared with bituminous coals. Fuel Process Technol 2012;101:1–9. doi:10.1016/j.fuproc.2012.03.010.

[85] Gil M V., Riaza J, Álvarez L, Pevida C, Pis JJ, Rubiera F. Kinetic models for the oxy-fuel combustion of coal and coal/biomass blend chars obtained in N2 and CO2 atmospheres. Energy 2012;48:510–8. doi:10.1016/j.energy.2012.10.033.

[86] Pan WP, Gan Y, Serageldin MA. A study of thermal analytical values for coal blends burned in an air atmosphere. Thermochim Acta 1991;180:203–17. doi:10.1016/0040-6031(91)80391-U.

[87] Morgan PA, Robertson SD, Unsworth JF. Combustion studies by thermogravimetric analysis. 1. Char oxidation. Fuel 1986;65:1546–51. doi:10.1016/0016-2361(87)90243-2.

[88] Yousefzad Farrokhi F, Kazanç F. Combustion Behavior and Kinetics of Turkish Lignite Blended with Biomass/Magnesite Dust. J Energy Eng 2018;144:1–13. doi:10.1061/(ASCE)EY.1943-7897.0000579.

[89] Al-Abbas AH, Naser J, Dodds D. CFD modelling of air-fired and oxy-fuel combustion of lignite in a 100 KW furnace. Fuel 2011;90:1778–95. doi:10.1016/j.fuel.2011.01.014.

[90] Chen L, Ghoniem AF. Simulation of oxy-coal combustion in a 100 kW th test facility using RANS and LES: A validation study. Energy and Fuels 2012;26:4783–98. doi:10.1021/ef3006993.

[91] Toporov D, Bocian P, Heil P, Kellermann A, Stadler H, Tschunko S, et al. Detailed investigation of a pulverized fuel swirl flame in CO2/O2 atmosphere. Combust Flame 2008;155:605–18. doi:10.1016/j.combustflame.2008.05.008.

[92] Kangwanpongpan T, Corrêa da Silva R, Krautz HJ. Prediction of oxy-coal combustion through an optimized weighted sum of gray gases model. Energy 2012;41:244–51. doi:10.1016/j.energy.2011.06.010.

[93] Jovanovic R, Milewska A, Swiatkowski B, Goanta A, Spliethoff H. Sensitivity analysis of different devolatilisation models on predicting ignition point position during pulverized coal combustion in O 2/N 2 and O 2/CO 2 atmospheres. Fuel 2012;101:23–37. doi:10.1016/j.fuel.2011.02.024.

[94] Álvarez L, Yin C, Riaza J, Pevida C, Pis JJ, Rubiera F. Oxy-coal combustion in an entrained flow reactor: Application of specific char and volatile combustion and radiation models for oxy-firing conditions. Energy 2013;62:255–68. doi:10.1016/j.energy.2013.08.063.

[95] Sankar G, Kumar DS, Balasubramanian KR. Computational modeling of pulverized coal fired boilers – A review on the current position. Fuel 2019;234:643–65. doi:10.1016/j.fuel.2018.08.154.

[96] Heydari M, Rahman M, Gupta R. Kinetic study and thermal decomposition behavior of lignite coal. Int J Chem Eng 2015;2015:1–9. doi:10.1155/2015/481739.

[97] Gürüz GA, Üçtepe Ü, Durusoy T. Mathematical modeling of thermal decomposition of coal. J Anal Appl Pyrolysis 2004;71:537–51. doi:10.1016/j.jaap.2003.08.007.

[98] Badzioch S, Hawksley PGW. Kinetics of Thermal Decomposition of Pulverized Coal Particles. Ind Eng Chem Process Des Dev 1970;9:521–30. doi:10.1021/i260036a005.

[99] Anthony DB, Howard JB, Hottel HC, Meissner HP. Rapid devolatilization of pulverized coal. Symp Combust 1975;15:1303–17. doi:10.1016/S0082-0784(75)80392-4.

[100] Solomon PR, Colket MB. Coal devolatilization. Symp Combust 1979;17:131–43. doi:10.1016/S0082-0784(79)80016-8.

[101] Kobayashi H, Howard JB, Sarofim AF. Coal devolatilization at high temperatures. Symp Combust 1997;16:411–25.

[102] Pitt GJ. The kinetics of the evolution of volatile products from coal. Fuel 1962;41:267–274.

[103] Anthony DB, Howard JB. Coal devolatilization and hydrogastification. AIChE J 1976;22:625–56. doi:10.1002/aic.690220403.

[104] Lakshmanan CC, White N. A New Distributed Activation Energy Model Using Weibull Distribution for the Representation of Complex Kinetics. Energy and Fuels 1994;8:1158–67. doi:10.1021/ef00048a001.

[105] De Caprariis B, De Filippis P, Herce C, Verdone N. Double-gaussian distributed activation energy model for coal devolatilization. Energy and Fuels 2012;26:6153–9. doi:10.1021/ef301092r.

[106] Hasse C, Universita T. Author ' s personal copy Models for Coal Kinetics 2015:0–18. doi:10.1016/B978-0-12-409547-2.11520-3.

[107] Niksa S, Kerstein AR. FLASHCHAIN Theory for Rapid Coal Devolatilization Kinetics. 1. Formulation. Energy and Fuels 1991;5:647–65. doi:10.1021/ef00029a006.

[108] Solomon PR, Hamblen DG, Carangelo RM, Serio MA, Deshpande G V. General Model of Coal Devolatilization. Energy & Fuels 1988;2:405–22. doi:10.1021/ef00010a006.

[109] Sommariva S, Maffei T, Migliavacca G, Faravelli T, Ranzi E. A predictive multi-step kinetic model of coal devolatilization. Fuel 2010;89:318–28. doi:10.1016/j.fuel.2009.07.023.

[110] Genetti D. An advanced model of coal devolatilization based on chemical structure. 1999.

[111] Maffei T, Milano PDI. Kinetic Model of Coal Combustion. 2013.

[112] Maffei T, Frassoldati A, Cuoci A, Ranzi E, Faravelli T. Predictive one step kinetic model of coal pyrolysis for CFD applications. Proc Combust Inst 2013;34:2401–10. doi:10.1016/j.proci.2012.08.006.

[113] Debiagi PEA, Heuer S, Ontyd C, Schiemann M, Faravelli T, Hasse C, et al. Differences in formation and oxidation of Colombian coal chars in air and oxy-fuel atmospheres. Chem Eng Trans 2019;74:151–6. doi:10.3303/CET1974026.

[114] Bear J. Dynamics of Fluids in Porous Media. American Elsevier Publishing Co, New York; 1988.

[115] Russell N V., Gibbins JR, Man CK, Williamson J. Coal char thermal deactivation under pulverized fuel combustion conditions. Energy and Fuels 2000;14:883–8. doi:10.1021/ef990241w.

[116] Hurt RH, Gibbins JR. Residual carbon from pulverized coal fired boilers: 1. Size distribution and combustion reactivity. Fuel 1995;74:471–80. doi:10.1016/0016-2361(95)98348-I.

[117] Zolin A, Jensen AD, Jensen PA, Dam-Johansen K. Experimental study of char thermal deactivation. Fuel 2002;81:1065–75. doi:10.1016/S0016-2361(02)00009-1.

[118] Senneca O, Salatino P, Masi S. Microstructural changes and loss of gasification reactivity of chars upon heat treatment. Fuel 1998;77:1483–93. doi:10.1016/S0016-2361(98)00056-8.

[119] Hurt R, Sun JK, Lunden M. A kinetic model of carbon burnout in pulverized coal combustion. Combust Flame 1998;113:181–97. doi:10.1016/S0010-2180(97)00240-X.

[120] Zhou Z, Chen L, Guo L, Qian B, Wang Z, Cen K. Computational modeling of oxy-coal combustion with intrinsic heterogeneous char reaction models. Fuel Process Technol 2017;161:169–81. doi:10.1016/j.fuproc.2017.03.009.

[121] McConnell J, Sutherland JC. The effect of model fidelity on prediction of char burnout for single-particle coal combustion. Proc Combust Inst 2017;36:2165–72. doi:10.1016/j.proci.2016.06.136.

[122] Shurtz RC, Fletcher TH. Coal char-CO2 gasification measurements and modeling in a pressurized flat-flame burner. Energy and Fuels 2013;27:3022–38. doi:10.1021/ef400253c.

[123] Srivastava A. Second law (exergy) analysis of various types of coal. Energy Convers Manag 1988;28:117–21. doi:10.1016/0196-8904(88)90036-2.

[124] Bilgen S, Kaygusuz K, Sari A. Second law analysis of various types of coal and woody biomass in Turkey. Energy Sources 2004;26:1083–94. doi:10.1080/00908310490494621.

[125] Juniper L, Schumacher G. Residual char combustion. In: Osborne D, editor. Coal Handb. Towar. Clean. Prod. Coal Util., Woodhead Publishing Limited; 2013, p. 312–51.

[126] Li L, Rowbotham JS, Christopher Greenwell H, Dyer PW. An Introduction to Pyrolysis and Catalytic Pyrolysis: Versatile Techniques for Biomass Conversion. 2013. doi:10.1016/B978-0-444-53878-9.00009-6.

[127] PerkinElmer Inc. TGA 4000 Thermogravimetric Analyzer 2012.

[128] Morgan PA, Robertson SD, Unsworth JF. Combustion studies by thermogravimetric analysis: 1. Coal oxidation. Fuel 1986;65:1546–51. doi:10.1016/0016-2361(86)90331-5.

[129] Avila C, Wu T, Lester E. Estimating the spontaneous combustion potential of coals using thermogravimetric analysis. Energy and Fuels 2014;28:1765–73. doi:10.1021/ef402119f.

[130] Li XG, Lv Y, Ma BG, Wang WQ, Jian SW. Decomposition kinetic characteristics of calcium carbonate containing organic acids by TGA. Arab J Chem 2017;10:S2534–8. doi:10.1016/j.arabjc.2013.09.026.

[131] Fluent. ANSYS FLUENT User ' s Guide 2011;15317:2498.

[132] Baxter LL, Fletcher TH, Ottesen DK. Spectral Emittance Measurements of Coal Particles. Energy and Fuels 1988;2:423–30. doi:10.1021/ef00010a007.

[133] Tufano GL, Stein OT, Kronenburg A, Gentile G, Stagni A, Frassoldati A, et al. Fully-resolved simulations of coal particle combustion using a detailed multi-step approach for heterogeneous kinetics. Fuel 2019;240:75–83. doi:10.1016/j.fuel.2018.11.139.

[134] Fogler HS. External Diffusion Effects on Heterogeneous Reactions. Elem. Chem. React. Eng. 4th ed., Prentice Hall; 2013, p. 757–813.

[135] Huang K, Goodenough JB. Voltage losses in a solid oxide fuel cell (SOFC). In: Huang K, Goodenough JB, editors. Solid Oxide Fuel Cell Technol., 2009, p. 98–140.

[136] Crittenden JC, Trussell RR, Hand DW, Howe KJ, Tchobanoglous G. Adsorption. MWH's Water Treat. Princ. Des. 3rd ed., Wiley; 2012, p. 1117–263.

[137] Hartmann M, Machoke AG, Schwieger W. Catalytic test reactions for the evaluation of hierarchical zeolites. Chem Soc Rev 2016;45:3313–30. doi:10.1039/c5cs00935a.

[138] Konno H, Ohnaka R, Nishimura JI, Tago T, Nakasaka Y, Masuda T. Kinetics of the catalytic cracking of naphtha over ZSM-5 zeolite: Effect of reduced crystal size on the reaction of naphthenes. Catal Sci Technol 2014;4:4265–73. doi:10.1039/c4cy00733f.

[139] Smoot LD, Smith PJ. Coal Combustion and Gasification. New York and London: Plenum Press; 1985.

[140] Debiagi PEA, Pecchi C, Gentile G, Frassoldati A, Cuoci A, Faravelli T, et al. Extractives Extend the Applicability of Multistep Kinetic Scheme of Biomass Pyrolysis. Energy and Fuels 2015;29:6544–55. doi:10.1021/acs.energyfuels.5b01753.

[141] Debiagi PEA. A Kinetic Model of Thermochemical Conversion of Biomass. 2018.

[142] Özer B, Amaral Debiagi PE, Hasse C, Faravelli T, Kazanç F. An experimental and numerical study on the combustion of lignites from different geographic origins. 14th Int. Conf. Energy a Clean Environ., Madeira, Portugal: 2019.

[143] Cong K, Han F, Zhang Y, Li Q. The investigation of co-combustion characteristics of tobacco stalk and low rank coal using a macro-TGA. Fuel 2019;237:126–32. doi:10.1016/j.fuel.2018.09.149.

[144] Wang C, Lei M, Liu H, Lu H. Combustion characteristics and nitric oxide release of the pulverized coals under oxy-enrich conditions. Ind Eng Chem Res 2012;51:14355–60. doi:10.1021/ie301097c.

[145] Xu J, Tang H, Su S, Liu J, Xu K, Qian K, et al. A study of the relationships between coal structures and combustion characteristics: The insights from micro-Raman spectroscopy based on 32 kinds of Chinese coals. Appl Energy 2018;212:46–56. doi:10.1016/j.apenergy.2017.11.094.

[146] Kosowska-Golachowska M, Gajewski W, Musiał T. Determination of the effective thermal conductivity of solid fuels by the laser flash method. Arch Thermodyn 2014;35:3–16. doi:10.2478/aoter-2014-0018.

[147] Incropera FP, Dewitt DP, Lavine AS, Bergman TL. Fundamentals of heat and mass transfer. 7th ed. 2011.

APPENDICES

A. Calculation of Non-dimensional Numbers

Biot number for heat transfer (Bi_h): Ratio of the heat transfer resistances inside of a body and at the surface of a body

$$Bi_h = \frac{hd_p}{k_p}$$

Where,

h : Overall convective heat transfer coefficient (W m^{-2} K^{-1})

d_p : Diameter of the fuel particle (110 μm)

k_p : Conductivity of the fuel particle (0.11-0.18 W m^{-1} K^{-1} for the fuels used in this study [146])

$$h = h_{conv} + h_{rad}$$

Where,

h_{conv} : Convective heat transfer coefficient (W m^{-2} K^{-1})

h_{rad} : Radiative heat transfer coefficient (W m^{-2} K^{-1})

$$h_{conv} = \frac{Nu_D d_p}{k_f}$$

Where,

Nu_D : Nusselt number of freely falling sphere (2 from equation 7.57 in [147] or equation 11.34 in [134])

d_p : Diameter of the fuel particle (110μm)

k_f : Conductivity of the fluid (0.08108 W m^{-1} K^{-1} for air at 1273 K)

$$h_{rad} = \varepsilon\sigma(T_s + T_{wall})\left(T_s{}^2 + T_{wall}{}^2\right)$$

Where,

ε : Emissivity of the fuel particle (0.95 for 110 μm lignite particle [132])

σ : Stefan Boltzmann constant (5.67×10^{-8} W m^{-2} K^{-4})

T_s : Absolute temperature of the surface of the fuel particle (293 K)

T_{wall} : Absolute temperature of DTF wall temperature (1273 K)

Reynolds number (Re): Ratio of inertia forces to viscous forces

$$Re = \frac{u_{hot} L}{\nu}$$

Where,

u_{hot} : Velocity of the fluid at hot zone (m/s)

D : Inner diameter of the tubular structure (0.075m)

ν : Kinematic viscosity of fluid at hot zone (7.9×10^{-5} m^2/s at $T_{film} = (T_\infty + T_{wall})/2$)

$$u_{hot} = \frac{Q_{in}\rho_{in}}{A_{cross}\rho_{hot}}$$

Where,

Q_{in} : Inlet volumetric flow rate of the fluid (20L/min)

ρ_{in} : Density of the inlet flow (1.28 kg/m^3 at 20ºC)

A_{cross} : Cross sectional area of the how zone of DTF (0.0044 m^2)

ρ_{hot} : Density of the inlet flow (1.28 kg/m^3 at 1000ºC)

Grashof number (Gr): Ratio of buoyant forces to viscous forces

$$Gr = \frac{g\beta(T_{wall} - T_{\infty})L^3}{\nu^2}$$

Where,

g : Acceleration due to Earth's gravity (9.81 m/s^2)

β : Coefficient of thermal expansion (1/K)

T_{wall} : Wall temperature (1273K)

T_{∞} : İnlet flow temperature (293K)

L : Lenth of the hot zone of DTF (1m)

ν : Kinematic viscosity of fluid (0.9×10^{-5} m^2/s at $T_{film} = (T_{\infty} + T_{wall})/2$)

Prandtl number (Pr): Ratio of momentum diffusivity and thermal diffusivity.

$$Pr = \frac{\mu c_p}{k_f} = \frac{\nu}{\alpha}$$

Where,

μ = Dynamic viscosity of fluid (N s m^{-2})

c_p = Specific heat of fluid (J kg^{-1} K^{-1})

k_f = Thermal conductivity of fluid (W m^{-1} K^{-1})

ν = Kinematic viscosity of fluid (7.9×10^{-5} m^2/s at $T_{film} = (T_{\infty} + T_{wall})/2$)

α = Thermal diffusivity of fluid (1.28×10^{-4} m^2/s at $T_{film} = (T_{\infty} + T_{wall})/2$)

Rayleigh number (Ra): Product of Gr and Pr

$$Ra = Gr \times Pr = \frac{g\beta(T_s - T_{\infty})L^3}{\nu\alpha}$$

Effectiveness factor (η): Ratio of actual reaction rate to the intrinsic reaction rate

$$\eta = \frac{\frac{3}{\varphi}\left(\frac{1}{\tanh(\varphi)} - \frac{1}{\varphi}\right)}{1 + \frac{\varphi}{Bi_m}\left(\frac{1}{\tanh(\varphi)} - \frac{1}{\varphi}\right)}$$

Where,

φ = Thiele modulus

Bi_m = Biot number for mass transfer

$$\varphi = \frac{d_p}{2}\sqrt{\frac{k_o e^{-\frac{E_a}{R_{gas}T_p}}}{D_e}}$$

$$Bi_m = \frac{k_g d_p}{D_e}$$

Where,

d_p = Diameter of the fuel particle (110μm)

k_o = Pre exponential factor of intrinsic gas-solid reaction (= 4.5×10^5 s^{-1})

E_a = Activation energy of intrinsic gas-solid reaction (= 34223 J/mol)

R_{gas}= The gas constant (8.314 J mol^{-1} K^{-1})

T_p= Temperature of the fuel particle (1300- 1400 K according to CFD analysis)

k_g = External mass transfer coefficient (m/s)

D_e = Effective diffusivity (m^2/s)

$$k_g = \frac{Sh\, D_{mol}}{d_p}$$

$$D_e = \frac{D_{mol} D_k}{D_{mol} + D_k} \theta^2$$

Where,

d_p = Diameter of the fuel particle (110μm)

D_{mol} = Molecular diffusion coefficient (m^2/s)

D_k = Knudsen diffusion coefficient (m^2/s)

θ = Porosity (0.5 (assumed))

Sh = Sherwood number of freely falling sphere (2 from equation 11.40 in [134])

$$D_k = \frac{2}{3} r_{pore} \sqrt{\frac{8}{\pi} \frac{R_{gas} T_g}{M_g}}$$

$$D_{mol} = D_{mol,0} \left(\frac{T_g}{T_{ref}} \right)^{1.75}$$

Where,

r_{pore} = Mean pore diameter ($5x\ 10^{-9}$ m [80])

R_{gas} = The gas constant (8.314 J mol^{-1} K^{-1})

T_g = Temperature of the ambient gas (1273 K according to CFD analysis)

M_g = Molecular mass of the oxygen (0.032 kg/mol)

$D_{mol,0}$ = Molecular diffusion coefficient of oxygen in air at standard temperature (273 K) and pressure (1 atm) ($1.78x\ 10^{-5}$ m_2/s)

T_{ref} = Standard temperature (273 K)

B. Calculation of Gas Content at the Tip of Collection Probe

$$x_{O_2,p} = \frac{Q_f x_{O_2,f} + Q_q x_{O_2,q}}{Q_p}$$

$$Q_f = Q_p - Q_q$$

Where,

$x_{O2,\,p}$: Mole fraction of oxygen in the flow in collection probe

$x_{O2,\,f}$: Mole fraction of oxygen in the flow coming from the furnace (21% (for air))

$x_{O2,\,q}$: Mole fraction of oxygen in the quenching gas (0% (for pure nitrogen))

Q_p : Volumetric suction rate in the collection probe (21 L/min)

Q_f : Volumetric flow rate coming from the furnace (L/min)

Q_p : Volumetric flow rate of the quenching gas (14 L/min)

C. Governing Equations Used in CFD Analysis

Energy equation:

$$\frac{\partial}{\partial t}(\rho E) + \nabla \cdot (\vec{v}(\rho E + p)) = \nabla \cdot \left(k_{eff} \nabla T - \sum_{j}^{n} h_j \vec{J}_j + \left(\bar{\bar{\tau}}_{eff} \vec{v} \right) \right) + S_h$$

Where,

ρ : Density (kg m^{-3})

v : Fluid Velocity (m s^{-1})

p : Fluid pressure (Pa)

T : Temperature (K)

k_{eff} : Effective conductivity (W m^{-1} K^{-1})

J_j : Diffusion flux of species j

τ_{eff} : Effective stress tensor

h_j : Sensible enthalpy of species j (j kg^{-1})

S_h : Volumetric Heat Source (j m^{-3} s^{-1})

n : Number of species

E : Total Energy (j kg^{-1})

$$E = h - \frac{p}{\rho} + \frac{v^2}{2}$$

Source of energy, S_h due to reaction:

$$S_{h,rxn} = -\sum_j \frac{h_j^0}{M_j} R_j$$

Where,

h^0_j : Enthalpy of formation of species j (j mol^{-1})

M_j : Molecular Weight (kg mol^{-1})

R_j : Volumetric rate of creation of species j (m^3 s^{-1})

Radiative transfer equation:

$$\frac{dI(\vec{r},\vec{s})}{ds} + (a+\sigma_s)I(\vec{r},\vec{s}) = an^2\frac{\sigma T^4}{\pi} + \frac{\sigma_s}{4\pi}\int_0^{4\pi} I(\vec{r},\vec{s}')\phi\,(\vec{s},\vec{s}')d\Omega'$$

Where,

I(r,s) : Radiative intensity

s : Direction

s’ : Scattering direction vector

r : Position

T : Local temperature (K)

n : Refractive index

a : Absorption coefficient

σ_s : Scattering coefficient

ϕ: Phase function

Ω' : Solid angle

Continuity:

$$\nabla \cdot (\vec{V}) = 0$$

Where,

V : Fluid Velocity Vector(m s^{-1})

Equation of state:

$$P = \rho RT$$

Where,

ρ : Density (kg m^{-3})

P : Pressure (Pa)

T : Temperature (K)

R : Specific gas constant (J K^{-1} kg^{-1})

Momentum equations:

x- Axis $\nabla.\left(\rho u\vec{V}\right) = -\frac{\partial P}{\partial x} + \frac{\partial \tau_{xx}}{\partial \mathrm{x}} + \frac{\partial \tau_{yx}}{\partial y} + \frac{\partial \tau_{zx}}{\partial z} + \rho f_x$

y- Axis $\nabla.\left(\rho v\vec{V}\right) = -\frac{\partial P}{\partial y} + \frac{\partial \tau_{xy}}{\partial \mathrm{x}} + \frac{\partial \tau_{yy}}{\partial y} + \frac{\partial \tau_{zy}}{\partial z} + \rho f_y$

z- Axis $\nabla.\left(\rho w\vec{V}\right) = -\frac{\partial P}{\partial z} + \frac{\partial \tau_{xz}}{\partial \mathrm{x}} + \frac{\partial \tau_{yz}}{\partial y} + \frac{\partial \tau_{zz}}{\partial z} + \rho f_z$

Where,

ρ : Density (kg m^{-3})

u : Fluid Velocity in x-axis (m s^{-1})

v : Fluid Velocity in y-axis (m s^{-1})

w : Fluid Velocity in z-axis (m s^{-1})

V : Fluid Velocity vector(m s^{-1})

P : Pressure (Pa)

f : body force

τ : Viscous stress (Pa)

$$\tau_{xx} = \lambda\left(\frac{\partial u}{\partial x} + \frac{\partial v}{\partial y} + \frac{\partial w}{\partial z}\right) + 2\mu\frac{\partial u}{\partial x}$$

$$\tau_{yy} = \lambda\left(\frac{\partial u}{\partial x} + \frac{\partial v}{\partial y} + \frac{\partial w}{\partial z}\right) + 2\mu\frac{\partial v}{\partial y}$$

$$\tau_{zz} = \lambda\left(\frac{\partial u}{\partial x} + \frac{\partial v}{\partial y} + \frac{\partial w}{\partial z}\right) + 2\mu\frac{\partial w}{\partial z}$$

$$\tau_{xy} = \tau_{yx} = \mu\left(\frac{\partial u}{\partial y} + \frac{\partial v}{\partial x}\right)$$

$$\tau_{xz} = \tau_{zx} = \mu\left(\frac{\partial u}{\partial z} + \frac{\partial w}{\partial x}\right)$$

$$\tau_{zy} = \tau_{yz} = \mu\left(\frac{\partial w}{\partial y} + \frac{\partial v}{\partial z}\right)$$

Where,

μ : Dynamic viscosity (kg m^{-1} s^{-1})

λ : Second viscosity coefficient

Transport equations for realizable k-ε model:

$$\frac{\partial(\rho k)}{\partial t} + \frac{\partial(\rho k u_j)}{\partial x_j} = \frac{\partial}{\partial x_j}\left[\left(\mu + \frac{\mu_t}{\sigma_k}\right)\frac{\partial k}{\partial x_j}\right] + G_k + G_b - \rho\varepsilon - Y_M + S_k$$

$$\frac{\partial(\rho\varepsilon)}{\partial t} + \frac{\partial(\rho\varepsilon u_j)}{\partial x_j} = \frac{\partial}{\partial x_j}\left[(\mu + \frac{\mu_t}{\sigma_\varepsilon}\frac{\partial \varepsilon}{\partial x_j}\right] + \rho C_1 S_\varepsilon - \rho C_2 \frac{\varepsilon^2}{k + \sqrt{v\varepsilon}} C_{1\varepsilon}\frac{\varepsilon}{k} C_{3\varepsilon} G_b + S_\varepsilon$$

$$C_1 = \sqrt{2S_{ij}S_{ij}}$$

$$\mu_t = C_\mu \rho \frac{k^2}{\varepsilon}$$

Where,

ρ : Density (kg m-3)

ε : Dissipation

u : Fluid Velocity (m s-1)

G_k : Generation of turbulence kinetic energy due to the mean velocity gradients

G_b : Turbulence kinetic energy generated with buoyancy effect

Y_M : Fluctuating dilatation in compressible turbulence

σ_k : Prandtl number for k

σ_ε : Prandtl number for ε

S_k and S_ε : user-defined source terms

Equation of motion for discrete phase:

$$\frac{du_p}{dt} = F_D(u - u_p) + \frac{g(\rho_p - \rho)}{\rho_p} + F$$

$$F_D = \frac{18\mu}{\rho_p d_p^2}\frac{C_D Re}{24}$$

$$Re = \frac{\rho d_p |u_p - u|}{\mu}$$

Where,

F_D (u-u_p): Drag force per unit particle mass (m s^{-2})

F_x: Additional acceleration (m s^{-2})

μ : Dynamic viscosity (kg m^{-1} s^{-1})

ρ_p : Density of the particle (kg m^{-3})

d_p : Diameter of the particle (kg m^{-3})

Re : Relative Reynolds number

u : Fluid velocity (m s-1)

u_p : Particle velocity (m s-1)

C_D : Drag coefficient

g : Gravitational acceleration (m s^{-2})

Momentum transfer from the continuous phase to discrete phase:

$$F = \sum \left(\frac{18\mu C_D Re}{\rho_p d_p^2 24} (u_p - u) + F_{other} \right) \dot{m}_p \Delta t$$

Where,

μ : Dynamic viscosity (kg m^{-1} s^{-1})

ρ_p : Density of the particle (kg m^{-3})

d_p : Diameter of the particle (kg m^{-3})

Re : Relative Reynolds number

u : Fluid velocity (m s-1)

u_p : Particle velocity (m s-1)

C_D : Drag coefficient

m_p : mass flow rate of the particles

Δt : time step

F_{other} : Other interaction forces

Heat transfer from the continuous phase to discrete phase

$$Q = \frac{\dot{m}_{p,0}}{m_{p,0}} \left[(m_{p,in} - m_{p,out}) [H_{pyrol} - H_{latref}] - m_{p,out} \int_{T_{ref}}^{T_{P,out}} c_{p_p} \, dT + m_{p,in} \int_{T_{ref}}^{T_{P,in}} c_{p_p} \, dT \right]$$

Where,

$\dot{m}_{p,0}$: Initial mass flow rate of the particle injection (kg s^{-1})

$m_{p,0}$: Initial mass of the particle (kg)

$m_{p,in}$: Mass of the particle on cell entry (kg)

$m_{p,out}$: Mass of the particle on cell exit (kg)

c_{pp} : Heat capacity of the particle (J kg^{-1} K^{-1})

H_{pyrol} : Heat of pyrolysis as volatiles are evolved (J kg^{-1})

$T_{P,in}$: Temperature of the particle on cell entry (K)

$T_{P,out}$: Temperature of the particle on cell exit (K)

T_{ref} : Reference temperature for enthalpy (K)

H_{latref} : Latent heat at reference conditions (J kg^{-1})

Discrete ordinates (DO) radiation model theory:

$$\nabla \cdot (I(\vec{r},\vec{s})\vec{s}) + (a+\sigma_s)I(\vec{r},\vec{s}) = an^2\frac{\sigma T^4}{\pi} + \frac{\sigma_s}{4\pi}\int_0^{4\pi} I(\vec{r},\vec{s}')\phi\,(\vec{s},\vec{s}')d\Omega'$$

Where,

I(r,s) : Radiative intensity

s : Direction

s’ : Scattering direction vector

r : Position

T : Local temperature (K)

n : Refractive index

a : Absorption coefficient

σ_s : Scattering coefficient

ϕ: Phase function

Ω’ : Solid angle

Intrinsic surface combustion model

$$R = \eta \frac{d_p}{6} \rho_p A_g k_i$$

$$\eta = \frac{3}{\phi^2}(\phi coth\phi - 1)$$

$$\phi = \frac{d_p}{2}\left[\frac{S_b \rho_p A_g k_i p_{ox}}{D_e \rho_{ox}}\right]^{1/2}$$

$$k_i = A_i e^{-(E_i/RT_p)}$$

Where,

η : Effectiveness factor

d_p : Diameter of the particle (m)

ρ_p : Density of the particle (kg m^{-3})

ϕ : Thiele modulus

ρ_{ox} : Density of oxidant in the bulk gas (kg m^{-3})

p_{ox} : Partial pressure of oxidant in the bulk gas (kg m^{-3})

D_e : Effective diffusion coefficient

A_g : Specific internal surface area of the char particle

k_i : intrinsic reactivity

A_i : Pre-exponential factor (s^{-1})

E_i : Activation energy (J/mol)

T_p : Particle Temperature (K)

Heat and mass transfer during char combustion

$$m_p c_p \frac{dT_p}{dt} = hA_p\left(T_\infty - T_p\right) - f_h \frac{dm_p}{dt} H_{reac} + A_p \varepsilon_p \sigma\left(\theta_R^4 - T_p^4\right)$$

Where,

m_p : Mass of the particle (m)

c_p : Heat capacity of the particle

T_p : Particle temperature (K)

A_p : the surface area of the particle (m^2)

T_∞ : Flow temperature (K)

h : Convective heat transfer coefficient for the particle surface

ε_p : Emissivity of the fuel particle (0.95 for 110 μm lignite particle [132])

σ : Stefan Boltzmann constant (5.67x 10-8 W m-2 K-4)

H_{reac} : Heat released by the surface reaction

D. Uncertainty Calculation

$$\text{Burnout} = \alpha = \frac{1 - w_i * \frac{w_b}{w_a}}{1 - w_i}$$

$$w_i = \frac{w_{a,i}}{w_{b,i}}$$

Table 7.1. Uncertainty analysis of the ashing process for Rhenish lignite (Since the real data was not recorded, experimental values are estimated based on the experimental procedure)

$w_{a,i}$	$\Delta w_{a,I}$, %	$w_{b,i}$	$\Delta w_{b,i}$, %	w_i	Δw_i, %
1.000	0.005	0.0287	0.005	0.0287	0.1792

Table 7.2. Uncertainty analysis of the burnout values of the each DTF experiments for Rhenish lignite

Probe level [cm]	w_i	Δw_i, %	w_b	Δw_b, %	w_a	Δw_a, %	α	Δα, %
50	0.0287	0.1792	0.0054	0.9259	0.0070	0.7143	0.9883	1.9986
50	0.0287	0.1792	0.0082	0.6098	0.0097	0.5155	0.9928	1.4837
60	0.0287	0.1792	0.0075	0.6667	0.0118	0.4237	0.9774	1.4488
60	0.0287	0.1792	0.0042	1.1905	0.0101	0.4950	0.9445	2.0440
65	0.0287	0.1792	0.0052	0.9615	0.0244	0.2049	0.8542	1.5249
65	0.0287	0.1792	0.0082	0.6098	0.0317	0.1577	0.8868	1.1259
70	0.0287	0.1792	0.0107	0.4673	0.0990	0.0505	0.6740	0.8762
70	0.0287	0.1792	0.0124	0.4032	0.1146	0.0436	0.6744	0.8053
75	0.0287	0.1792	0.0183	0.2732	0.1762	0.0284	0.6592	0.6600
75	0.0287	0.1792	0.0165	0.3030	0.1810	0.0276	0.6062	0.6891

Table 7.3. Standard deviations and the uncertainties of mean burnout values for Rhenish lignite

Probe level [cm]	α_1	α_2	Standard Deviation	α_{mean}	$\Delta\ \alpha_{mean}$, %	$\Delta\ \alpha_{mean}$
50	0.9883	0.9928	0.00225	0.9905	3.4823	0.0344
60	0.9774	0.9445	0.01645	0.9609	3.4928	0.0335
65	0.8542	0.8868	0.0163	0.8705	2.6508	0.0230
70	0.6740	0.6744	0.0002	0.6742	1.6815	0.0113
75	0.6592	0.6062	0.0265	0.6327	1.3491	0.0085

Table 7.4. Combined uncertainties of mean burnout values for Rhenish lignite

Probe level	Statistical uncertainty (from standard deviation)	Systematic uncertainty (from instrumental error)	Combined uncertainty
50	0.0016	0.0345	0.0345
60	0.0116	0.0336	0.0355
65	0.0115	0.0231	0.0258
70	0.0001	0.0113	0.0113
75	0.0187	0.0085	0.0206

Table 7.5. Uncertainty analysis of the collection process of the each DTF experiments for Rhenish lignite

Probe level, L	ΔL	ΔL, %	Residence time, t	Δt
50	±1 cm	2.00	0.757	0.015
60	±1 cm	1.67	0.582	0.009
65	±1 cm	1.54	0.499	0.007
70	±1 cm	1.43	0.420	0.006
75	±1 cm	1.33	0.345	0.004

E. Polimi Model Kinetic Mechanism

Table 7.6. Mechanism of the devolatilization

DEVOLATILIZATION	**A (1/s)**	**E (j/mol)**
COAL1=>COAL1_M+CH2_M+CHAR+.5H2	.5000E+10	35000.0
COAL1=>COAL1_M+CH2+CHAR+.5H2	.1000E+16	65000.0
COAL1_M=>4CHARH+1.25CHAR+.75CH4+.5H2	.2000E+09	36000.0
COAL1_M=>TAR1_M	.1000E+09	36000.0
COAL1_M=>4CHARH+CHAR+CH4	.1000E+15	75000.0
COAL1_M=>0.25TETRALIN+0.625C12H8	.1000E+15	75000.0
TAR1_M=>0.25TETRALIN+0.625C12H8	.2500E+13	50000.0
TAR1_M+CHARH=>5CHARH+CHAR+CH4	.2500E+11	32500.0
TAR1_M+CHAR=>4CHARH+2CHAR+CH4	.2500E+11	32500.0
COAL2=>2.CHAR+3.94CHARH+.25COAL1+.02BTX_M+.31CH4_M+.11CH2_M+.11COH2_M+.15CO2_S_M+.41H2O_M+.18CO_L_M+.265H2	.6000E+11	36000.0
COAL2=>1.81CHAR+3.73CHARH+.21COAL1+.08BTX_M+.27CH4+.50CO+.1H2O+.3COH2_M+.48H2+0.1CO_L_M	.4000E+19	63000.0
COAL2=>TAR2_M	.5000E+11	36000.0
COAL2=>0.3055555556C10H7CH3+0.3944444444BIN1B+0.25C11H12O4	.4000E+18	63000.0
TAR2_M=>0.3055555556C10H7CH3+0.3944444444BIN1B+0.25C11H12O4	.2400E+10	39000.0
TAR2_M+CHARH=>7.CHARH+1.5CHAR+H2O_M+.5CH4	.4500E+09	30000.0

TAR2_M+CO2_TS_M=>CO2_TS_M+.15CO2_S_M+1.94CHAR+4.CHARH+.25COAL1+.02BTX_M+.3CH4_M+.05CH2_M+.1COH2_M+.4H2O_M+.2CO_L_M+.335H2	.1500E+12	30000.0
COAL3=>2.73CHAR+1.8CHARH+.22COAL1+.04BTX_M+.2CH3O+.1CH4_M+.11CH2_M+.2H2+.6COH2_M+2.2H2O_M+.1CO2+.38CO2_M+.02CO2_TS_M+CO_L_M	.2000E+11	33000.0
COAL3=>COAL3_M	.5000E+19	61000.0
COAL3_M=>1.0CHARH+2.23CHAR+1.9CO+.25CH3O+.17CH4+.74CH2+.5CO2+.65COH2_M+.08BTX_M+.21COAL1+1.2H2O+.48H2	.1200E+09	30000.0
COAL3=>TAR3_M+CO2_M+H2O	.1600E+10	33000.0
COAL3=>0.1192411924C10H7CH3+0.1539295393BIN1B+0.3170731707C9H10O2+0.3414634146C11H12O4+CO2+H2O	.2000E+19	61000.0
TAR3_M=>0.1192411924C10H7CH3+0.1539295393BIN1B+0.3170731707C9H10O2+0.3414634146C11H12O4	.5000E+10	32500.0
TAR3_M+CHARH=>4CHARH+2.5CHAR+.2CH4_M+2COH2_M+.8H2+.3CH2_M	.1400E+12	30000.0
BTX_M=>0.5C10H7CH3+0.75TETRALIN	.4000E+13	48000.0
CH4_M=>CH4	.1000E+04	17000.0
CH2_M=>CH2	.1000E+04	17000.0
CO2_M=>CO2	.1000E+04	18000.0
CO2_S_M=>CO2	.1000E+03	18000.0

Table 7.7. Mechanism of the thermal annealing

ANNEALING	**A (1/s)**	**E (j/mol)**
CHARH=>2CHAR+0.5H2	.1000E+12	80000.0
CHAR=>CHARG	.3000E+04	50167.0

Table 7.8. Mechanism of the nitrogen release

NITROGEN	**A (1/s)**	**E (j/mol)**
N_COAL1=>COAL1_M+ .19 CH2_M+.74 H2 +0.07NH3_M+ 0.05HCN_M+ 0.88NCHAR	.2000E+09	40000
N_COAL1 => NTAR_M + .75 TAR1_M + .5 CHAR	.4000E+08	40000
N_COAL1=> .84 COAL1_M+CH2+CHAR+.59 H2 + 0.05NH3 + 0.3 HCN + 0.65 NCHAR	.1600E+16	75000
N_COAL2 => 2.93CHAR+ 2.64CHARH+ .25COAL1+ .02BTX_M+ .31CH4_M+.11CH2_M+.11COH2_M+.15CO2_S_M+.41H2O_M+.18CO_L_M+.265H2+0.15NH3_M+0.03HCN_M+0.82NCHAR	.1000E+15	75000
N_COAL2 => NTAR_M + .5TAR2_M +.5 CO + 2.5 CHAR	.5000E+11	36000.0
N_COAL2 => 1.81CHAR+ 3.03CHARH+ .21COAL1+ .08BTX_M+ .27CH4+ .50CO+ .1H2O+.3COH2_M+.18H2+0.1CO_L_M + 0.15NH3+ 0.3HCN+ 0.55NCHAR	.3000E+18	63000.0
N_COAL2 => 0.08C10H7CH3+0.12BIN1B+0.25C11H12O4 +NTAR +3.970CHAR	.4000E+18	63000.0
N_COAL3=>3.78CHAR+0.5CHARH+.22COAL1+.04BTX_M+.2CH3O+.1CH4_M+.11CH2_M+.2H2+.6COH2_M+2.2H2O_M+.1CO2+.38CO2_M+.02CO2_TS_M+CO_L_M +0.15NH3_M+0.15HCN_M+0.7NCHAR	.4000E+11	33000.0
N_COAL3=>0.55TAR3_M+1.95CO2_M+0.75H2_M+NTAR_M	.1600E+10	33000.0
N_COAL3=>0.8 COAL3_M + 0.5CO2 +0.275 CH4+0.025CHAR + 0.15NH3+ 0.1HCN+ 0.75NCHAR	.5000E+19	61000.0
N_COAL3=>0.04BIN1B+0.2C9H10O2+0.35C11H12O4+1.5CO2+0.2H2O +0.05CHAR+NTAR	.2000E+19	61000.0
CHAR + NTAR_M => 0.95 CH4 + 2.3 CHAR + 0.05HCN_M+ 0.1NH3_M+ 0.85NCHAR	.1100E+10	32500.0

NTAR_M => NTAR	.3800E+09	33000.0
NH3_M => NH3	.7000E+03	23000.0
HCN_M => HCN	.4000E+03	23000.0
NCHAR => HCN + CHAR	.4000E+10	80000.0

Table 7.9. Mechanism of the sulfur release

SULFUR	**A (1/s)**	**E (j/mol)**
SAL => 0.4H2S_M+0.2C2H3SH_M+0.4SCHAR+ 0.6BTX_M+4.3CHAR+ 1.5CH4	.5500E+11	33000.0
SAL => 0.5H2S +0.3C2H3SH +0.2SCHAR+0.8BTX_M+3.0CHAR+1.3H2	.4000E+19	61500.0
SARO => 0.2H2S_M+ 0.1C2H3SH_M+ 0.7SCHAR+ 1.0BTX_M+ 0.5CHAR+ 0.3CH4	.8000E+10	36000.0
SARO => 0.3H2S +0.3C2H3SH +0.4SCHAR+1.0BTX_M+ 0.4CHAR+ 0.1H2	.8500E+18	65000.0
STHIO => 0.9SCHAR+0.1C2H3SH_M +.5 BTX_M +.15 CH4 + 5.15 CHAR	.5000E+10	38000.0
STHIO => 0.5SCHAR+0.5C2H3SH+.3 BTX_M + .45 CH4 +6.65 CHAR	.2000E+18	70000.0
CHAR + STAR_M => SCHAR+ 6.25 CHAR +.5 BTX_M +.25 CH4_M	.5000E+08	24000.0
SAL => STAR_M + 2 CH4_M	.2300E-02	20659.0
SAL => STAR + 2 CH4	.1080E+19	60216.0
SARO => STAR_M + 2 CH4_M	.2300E-02	20659.0
SARO => STAR + 2 CH4	.1080E+19	60216.0
STHIO => STAR_M	.2300E-02	20659.0
STHIO => STAR	.1080E+19	60216.0
STAR_M => STAR	.4030E+10	35258.0
SPYR => .5H2S+0.5SCHAR+SPYR2	.1600E+08	36065.0
SPYR2 => H2S	.1300E+06	75731.0
SSUL => .666666667 SO3 + 0.33333333 SCHAR	.1800E+03	21000.0
H2S_M => H2S	.5000E+04	20000.0
C2H3SH_M => C2H3SH	.2100E+04	22000.0

Table 7.10. Mechanism of the heterogeneous reactions

HETEROGENEOUS	**A (1/s)**	**E (j/mol)**
COH2_M+O2=>H2O+CO2	.1200E+11	23667.0
CHARH+0.75O2=>0.5H2O+CO+CHAR	.0260E+11	26667.0
CHAR+O2=>CO2	.1600E+11	28250.0
CHAR+0.5O2=>CO	.0715E+12	34223.0
CHARG+O2=>CO2	.0500E+11	32028.0
CHARG+0.5O2=>CO	.0290E+11	37000.0
CHARH+0.5H2O=>H2+0.5CO+1.5CHAR	.4600E+12	46345.0
CHAR+H2O=>H2+CO	.1500E+13	53034.0
CHARG+H2O=>H2+CO	.2900E+12	53989.0
CHARH+0.5CO2=>0.5H2O+0.5CO+2CHAR	.3000E+13	55184.0
CHAR+CO2=>2CO	.4000E+13	59962.0
CHARG+CO2=>2CO	.1000E+13	61395.0

F. Coal Classification

Table 7.11. Volati Seyler's coal classification [16]

<table>
<tr><td></td><td colspan="7">Species</td></tr>
<tr><td></td><td rowspan="2">Anthracite</td><td></td><td colspan="4">Bituminous</td><td>Lignit</td></tr>
<tr><td></td><td>Carbonaceous</td><td>Meta-</td><td>Ortho-</td><td>Para-</td><td>Meta-</td><td>Ortho</td></tr>
<tr><td>Genera</td><td>Carbon over 93.3%</td><td>Carbon % 93.3-91.2</td><td>Carbon % 91.2-89.0</td><td>Carbon % 89.0-87.0</td><td>Carbon % 87.0-84.0</td><td>Carbon %84-80</td><td>%80-75</td></tr>
<tr><td>Per-bituminous Hydrogen > 5.8%</td><td>-</td><td>-</td><td>Per-bituminous (per-meta-bituminous)</td><td>Per-bituminous (per-ortho-bituminous)</td><td>Per-bituminous (per-pare-bituminous)</td><td colspan="2">Per- lignitous</td></tr>
<tr><td rowspan="2">bituminous Hydrogen 5.0-5.8%</td><td rowspan="2">-</td><td rowspan="2">Pseudo-bituminous species</td><td rowspan="2">Meta-bituminous</td><td rowspan="2">Ortho-bituminous</td><td rowspan="2">Para-bituminous</td><td colspan="2">Lignitous</td></tr>
<tr><td>Meta</td><td>Ortho</td></tr>
<tr><td rowspan="2">Semi-bituminous Hydrogen 4.5-5.0%</td><td rowspan="2">-</td><td rowspan="2">Semi-bituminous species (ortho-semi-bituminous)</td><td rowspan="2">Sub-bituminous (sub- meta-bituminous)</td><td rowspan="2">Sub-bituminous (sub- ortho-bituminous)</td><td rowspan="2">Sub-bituminous (sub- Para-bituminous)</td><td colspan="2">Sub- lignitous</td></tr>
<tr><td>Meta</td><td>Ortho</td></tr>
<tr><td>Carbonaceous Hydrogen 4.0-4.5%</td><td>Semi-anthracitic species</td><td>Carbonaceous species (ortho-carbonaceous)</td><td>Pseudo-carbonaceous (sub- meta-bituminous)</td><td>Pseudo-carbonaceous (sub-ortho-bituminous)</td><td>Pseudo-carbonaceous (sub- para-bituminous)</td><td></td><td></td></tr>
</table>

G. Characteristic Temperatures and Stages

Table 7.12. Combustion characteristic temperatures of each fuel for different heating rates in TGA experiments: Decomposition temperature (Td), ignition temperature (Tig), peak temperature (Tp), burnout temperature (TB)

			5 K/min	10 K/min	15 K/min	20 K/min
Decomposition Temperature	T_d	RL	293	289	268	265
		SL	368	345	332	323
		TL	377	354	354	351
		AEL	296	271	267	265
Ignition Temperature	T_{ig}	RL	331	344	349	329
		SL	400	412	423	429
		TL	415	425	436	441
		AEL	302	313	314	317
Peak Temperatures	T_{p1}	RL	383	387	383	368
		SL	465	485	505	509
		TL	476	485	500	511
		AEL	379	402	419	422
	T_{p2}	RL	514	527	534	540
		AEL	631	649	656	658
	T_{p3}	AEL	701	719	729	739
Burnout Temperature	T_B	RL	515	540	551	556
		SL	514	551	581	600
		TL	538	573	603	620
		AEL	704	730	748	758

Table 7.13. Combustion characteristic stages of each fuel for different heating rates in TGA experiments: Decomposition Stage (Tig- Td), Combustion Stage (Tb -Tig)

			5 K/min	10 K/min	15 K/min	20 K/min
Decomposition Stage (T_{ig}- T_d)	ΔT [K]	RL	38.0	55.0	81.0	64.0
		SL	32.0	67.0	91.0	106.0
		TL	38.0	71.0	82.0	90.0
		AEL	6.0	42.0	47.0	52.0
	Δt [min]	RL	7.6	5.5	5.4	3.2
		SL	6.4	6.7	6.1	5.3
		TL	7.6	7.1	5.5	4.5
		AEL	1.2	4.2	3.1	2.6
Combustion Stage (T_b -T_{ig})	ΔT [K]	RL	184.0	196.0	202.0	227.0
		SL	114.0	139.0	158.0	171.0
		TL	123.0	148.0	167.0	179.0
		AEL	402.0	417.0	434.0	441.0
	Δt [min]	RL	36.8	19.6	13.5	11.4
		SL	22.8	13.9	10.5	8.6
		TL	24.6	14.8	11.1	9.0
		AEL	80.4	41.7	28.9	22.1